Targeting CDC25B-CDK2/CyclinA Activity Using Chemical Biology Approaches

by

George Lund

A dissertation submitted in partial fulfillment
of the requirements for the degree of
Doctor of Philosophy
(Molecular and Cellular Pathology)
in The University of Michigan
2015

Doctoral Committee:

        Assistant Professor Tomasz Cierpicki, Chair
        Associate Professor David O. Ferguson
        Assistant Professor Zaneta Nikolovska-Coleska
        Research Assistant Professor Matthew A. Young

To my amazing wife Carryn

Acknowledgements

I would like to thank my mentor Tomasz Cierpicki for his patience, advice, and guidance throughout my graduate career. I also would like to thank Jolanta Grembecka for her help and support during my thesis research. The entire Cierpicki-Grembecka lab has been a wonderful source of support and knowledge, and I am forever grateful to all current and former lab members for their help. I'd especially like to thank the graduate students in the lab, Felicia Gray, Jon Pollock, and Dave Rogawski for years of camaraderie through the my graduate career. I would additionally like to thank my thesis committee for their helpful input and support through my graduate studies. Thanks also to Martha Larson and Steve Vander Roest for their help with my high-throughput screening work.

Thank you to all of my friends and family who made this journey possible. My friends have always been a great source of support for me through my graduate studies and I thank them sincerely for everything they have done for me. Thanks to my parents Dave and Diane Lund, and my brother Tom, for your love and support. You three taught me to be skeptical and question authority, while always keeping me optimistic. Without you I wouldn't be here. Thanks also to my second family, Dan, Tami, Alyssa and Jarad Christianson. You have supported me and helped me grow over the last 11 years, and I'm very lucky to have you all in my life.

Most importantly, thanks to my wife Carryn, without whom I would be entirely lost. You have been the best partner anyone could ask for. You moved to Ann Arbor with me not knowing where this crazy adventure might take us, and I owe you forever for your support and love. Thank you, thank you, thank you.

Table of Contents

Chapter 2: Characterization of CDC25B-CDK2/CycA-Mre11 interactions using biochemical and biophysical methods

Chapter 3: Identification of inhibitors of the CDC25B-CDK2/Cyclin A interaction through fragment screening by NMR

Chapter 4: High-throughput screening to identify inhibitors of the CDC25B-CDK2/Cyclin A protein-protein interaction

Chapter 5: Conclusions and future directions

Chapter 6: Appendix - development of the FMAP program for use in the rational design of fluorinated compounds

List of Figures

List of Tables

List of Abbreviations

cyclin dependent kinase (CDK), cell division cycle 25 (CDC25), adenosine triphosphate (ATP), CDK activating kinase (CAK), deoxyribonucleic acid (DNA), nuclear export signal (NES), nuclear localization signal (NLS), checkpoint kinase (Chk), DMBA (7,12-dimethyl-1,2-benzanthracine), small interfering RNA (siRNA), microRNA (miRNA), dithiothreitol (DTT), MRN complex (Mre11, Rad50, and NBS1), nuclear magnetic resonance (NMR), heteronuclear single-quantum coherence (HSQC), generalized order parameter (S^2), parts per million (ppm), Carr–Purcell–Meiboom–Gill (CPMG), residual dipolar coupling (RDC), C-terminal 76 residues of Mre11 ($Mre11^{C76}$), tabacco etch virus (TEV), Isopropyl β-D-1-thiogalactopyranoside (IPTG), tris(hydroxymethyl)aminomethane (Tris), phenylmethylsulfonyl fluoride (PMSF), tris(2-carboxyethyl)phosphine (TCEP), Ubiquitin-like-specific protease 1 (ULP1), deuterium oxide (D_2O), Nuclear Overhauser effect (NOE), Isothermal titration calorimetry (ITC), Bifunctional ligase/repressor (BirA), phosphate buffered saline (PBS), 2-fluoro-4-hydroxybenzonitrile (compound **1**), Dimethyl sulfoxide (DMSO), Amplified Luminescent Proximity Homogeneous Assay (AlphaLISA), bovine serum albumin (BSA), sodium dodecyl sulfate (SDS), polyacrylamide gel electrophoresis (PAGE), Tris-buffered saline with 0.1% Tween-20 (TBS-T), horseradish peroxidase (HRP), Thin Layer Chromatography (TLC), ultra-violet (UV), infrared (IR), dichloromethane (DCM), N,N-diisopropylethylamine (DIPEA), chloromethyl methyl ether (MOMCl), dimethylformamide (DMF), hydrochloric acid (HCl), ethyl acetate (EtOAc), ethanol (EtOH), protein-protein interaction (PPI), high-throughput screening (HTS),

homogeneous time-resolved fluorescence (HTRF), fluorescent resonance energy transfer (FRET), signal-to-noise (S/N), coefficient of variation (CV), 3 standard deviations compared to plate negative controls (3SD), University of Michigan Center for Chemical Genomics (UM-CCG), saturation transfer difference (STD), Dulbecco's Modified Eagle Medium (DMEM), 3-(4,5-dimethylthiazol-2-yl)-2,5-diphenyltetrazolium bromide (MTT), Ethylenediaminetetraacetic acid (EDTA), sodium orthovanadate (Na_3VO_4), nonyl phenoxypolyethoxylethanol (NP-40), ribonuclease A (RNaseA)

Abstract

The cell cycle is a fundamental process of cell biology, and its progression is highly regulated. A critical mode of regulation for proper advancement of the cell cycle is the activation of the CDKs by the CDC25 family of dual specificity phosphatases. The CDC25 proteins are often overexpressed or misregulated in cancer, resulting in dysregulated cell growth, genomic instability and evasion of apoptosis. The oncogenic role of the CDC25 proteins has inspired over two decades of drug discovery efforts to inhibit their enzymatic activity. Despite these efforts, no therapeutic agents targeting family of CDC25 phosphatases emerged. In order to identify new classes of CDC25B inhibitors, new approaches to target CDC25 are needed.

We have employed a novel approach to inhibit the CDC25 family member CDC25B by targeting its interaction with its native substrate, the CDK2/Cyclin A complex. We used two different methods, fragment-based drug discovery and "gray-box" high-throughput screening, to identify inhibitors of the CDC25B-CDK2/Cyclin A protein-protein interaction. Using NMR-based fragment based screening, we identified a small molecule ligand of the CDC25B catalytic domain. We solved the co-crystal structure with this ligand bound to CDC25B, and used this structure to develop more potent analogs. We have shown that fragment-derived compounds can disrupt the CDC25B-CDK2/Cyclin A interaction and inhibit CDC25B catalytic activity. To our knowledge, our inhibitor-bound crystal structure of CDC25B is the first crystal structure with CDC25B bound to a small molecule ligand.

We have also developed several protein-protein interaction assays to quantify the

interaction between CDC25B and CDK2/Cyclin A. We employed these assays in three high-throughput screens to identify several classes of CDC25B-CDK2/Cyclin A protein-protein interaction inhibitors. The inhibitors we identified do not target CDC25B, but disrupt the protein-protein interaction by targeting CDK2/Cyclin A. Importantly, we have developed a high quality screening assay for the identification of CDC25B-CDK2/Cyclin A interaction inhibitors. This assay will be useful for future drug discovery efforts targeting the CDC25B-CDK2/Cyclin A interaction.

In summary, we have developed two new approaches to inhibit CDC25B. These results pave the way towards the development of new chemical probes and potential therapeutic agents targeting CDC25B.

Chapter 1

Introduction

1.1 Abstract

The biology of the cell cycle and its regulation by the cyclin dependent kinases (CDKs) and the cell division cycle 25 (CDC25) phosphatases has been studied for many years. The activation of the CDKs by the CDC25 proteins is critical for proper advancement through the cell cycle and regulates vital cell cycle checkpoints. Dysregulation of the CDKs in cancer by overexpression or aberrant activation of the CDC25 proteins overcomes cell cycle checkpoints, resulting in unregulated cell growth, genomic instability and evasion of apoptosis. For these reasons, regulators of the cell cycle, including the CDC25 phosphatases, have been active targets of inhibitor development for many years. Yet no therapeutic agents targeting any of the CDC25 proteins have made it through clinical trials despite significant drug discovery efforts. Presented here is a summary of the role of the CDKs and CDC25s in normal and cancer biology, as well as previous efforts to inhibit the CDC25 phosphatases.

1.2 Structure and function of CDC25 phosphatases and their CDK/Cyclin substrates

1.2.1 CDK/Cyclin complexes in cell cycle regulation

The cyclin-dependent kinases (CDKs) are important regulators for progression through the cell cycle. CDK family members regulate a wide variety of cellular processes including cell growth, DNA replication and damage repair, and mitosis[1–3]. In humans, there are 13 genes encoding the classical CDK family proteins CDKs 1-13, and an additional 9 genes encoding for proteins identified to be CDK-like proteins based on sequence homology and conserved primary structure[4,5]. All CDKs contain a Ser/Thr protein kinase domain that is responsible for its enzymatic activity. The CDKs are highly similar across the family, with sequence identities ranging from 40 – 60 %. CDK family members all have a fold common to all protein kinases containing an active site with an ATP binding cleft between N-terminal and C-terminal lobes. The CDK family of kinases is highly conserved; of the 13 classical CDKs found in humans, there are 11 homologs in *D. melanogaster*, 10 in *C. elegans* and a single CDK in *S. cerevisiae*[6]. Complementation experiments highlight the degree of conservation by showing that the human homolog of CDK1 can complement a mutated form of the *S. cerevisiae* CDK[7].

Due to the regulatory role of the CDK family in many cellular processes, their activity is highly regulated (Figure 1.1). A primary mode of regulation is through the binding of proteins called cyclins resulting in formation of catalytically active CDK/Cyclin heterodimer complexes[8]. Cyclin binding to a CDK plays two roles in activating the CDK. First, cylins induce a conformational shift in two regions of CDK that occlude the active site in the free form of the CDK, allowing for substrate access to the active site[9]. Second, cyclins contain a binding site that is responsible in part for substrate recruitment and the specificity of CDK activity through their RxL-binding pocket[10,11]. CDKs are also regulated through phosphorylation. Activation of CDKs
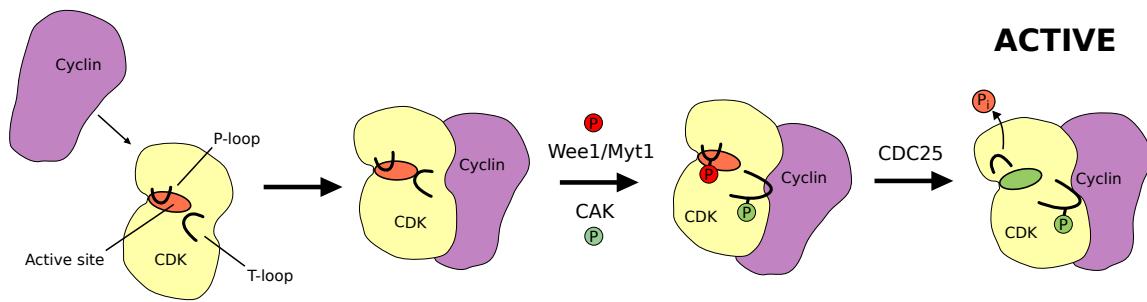
Figure 1.1. *Steps in CDK activation*. Schematic of how CDKs are regulated by cyclin binding and phosphorylation state. Red "P" circles represent inhibitory phosphorylations and green "P" circles represent activating phosphorylations. Enzymes responsible for catalyzing the phosphorylation reactions are given.

is achieved through phosphorylation of Thr160 by the CDK activating kinase (CAK) on the conserved T-loop on CDKs which greatly increases the catalytic turnover rate[12,13]. Inhibitory phosphorylation by Wee1[14] or Myt1[15] kinases on T14 and/or Y15 in the conserved P-loop of CDK2 locks the active site in a closed conformation[16]. Removal of inhibitory phosphorylations on T14 and/or Y15 by the cell division cycle 25 (CDC25) phosphatases on the conserved glycine-rich P-loop of CDK further opens access to the active site and is required for full kinase activity[17]. Importantly, dephosphorylation of the CDKs by the CDC25 phosphatases is thought to be the rate-limiting step in CDK activation[18,19]. In addition to cyclin binding and phosphorylation state, it has recently been shown that, at least for the CDK2/Cyclin A complex, intracellular Mg^{2+} also plays a role in tuning CDK activity[20,21].

The various roles for the different CDKs in the phases of the cell cycle have been studied for many years. Canonically, CDK4 and CDK6 are activated by D-cyclins (D1, D2, D3) in G1 phase to promote progression of the G1 and early S phases primarily through phosphorylation

of the retinoblastoma family proteins p107, p130, and pRb[22,23]. Phosphorylation and subsequent activation of the retinoblastoma family members leads to the expression of E-type cyclins (E1, E2), which in turn bind and activate the CDK2 protein early in S-phase to initiate DNA synthesis[6,23,24]. Once S-phase is initiated, E-type cyclins are actively degraded and replaced by A-type cyclins for CDK2 binding[4,25]. The CDK2/Cyclin A complex regulates the S-G2 phase transition through the phosphorylation of a variety of proteins including transcription factors and cell-cycle checkpoint proteins[26,27]. In the early stages of mitosis A-type cyclins interact with CDK1 to stop DNA replication and to control the spindle assembly process[3,28]. A-type cyclins are then degraded and CDK1 binds to B-type cyclins, which regulate many mitotic processes such as chromosomal condensation[29,30].

Recent genetic studies using CDK knockouts in mice has cast some doubt on the classical role of the CDKs. In mouse models, CDK1 knockout is the only CDK family member that is absolutely required for cell division[31]. Knockouts of other CDKs, alone or in combination, are either embryonic lethal or lead to sterile adult mice but do not show unilateral cell cycle arrest[4]. This suggests a compensatory role for CDK1 throughout all phases of the cell cycle. Roles for the other CDK family members may be more tissue specific, as mice without CDK2, CDK4, and CDK6 are embryonic lethal due to decreased hematopoietic precursors[31].

1.2.2 Structure and biology of the CDC25 phosphatases

As mentioned above, the CDC25 family of phosphatases are critical regulators of the CDK proteins by catalyzing the removal of inhibitory phosphates. The CDC25 phosphatases are dual specificity phosphatases belonging to the protein tyrosine phosphatase superfamily of enzymes[32], which are characterized by their phosphatase activity through a signature HCX_5R

catalytic motif. There are three genes encoding for the CDC25 phosphatases in humans corresponding to the three CDC25 family members, CDC25A, CDC25B, and CDC25C[32]. All three CDC25 family members contain an N-terminal regulatory domain and a C-terminal catalytic domain. The regulatory domains of the family members vary widely between the three proteins, and alternative splicing in the N-terminal domains leads to multiple isoforms for each protein[33,34]. The N-terminal domain of the CDC25 proteins contains a both a nuclear export signal (NES) and a nuclear localization signal (NLS), as well as many phosphorylation sites involved in their regulation. The C-terminal catalytic domains are highly similar between all three proteins, with approximately 60 % sequence identity between any of the family members. The three phosphatases have highly similar protein folds, the only exception being an additional C-terminal helix found in the CDC25B crystal structure that is not observed the crystal structures of either CDC25A or CDC25C[35–37]. Other than their active site HCX_5R motif, the CDC25 family is distinct from all other known protein tyrosine phosphatases in both sequence homology and protein fold[32]. Potentially due to their unique structures, the CDC25 proteins are the only known phosphatases to catalyze removal of the inhibitory CDK phosphorylations[32]. Additionally, only a few non-CDK substrates have been identified[38,39], indicating that their primary role in the cell is to activate CDK proteins.

The CDC25 phosphatases have been thought to play specific roles throughout the cell cycle (Figure 1.2). CDC25A is considered to be the primary regulator in the G1/S phase transition by dephosphorylating and activating the CDK4/6/Cyclin D, CDK2/Cyclin E and CDK2/Cyclin A complexes[40–42]. The S/G2 phase transition checkpoint is dominantly regulated by CDC25B[43]. CDC25B regulates this checkpoint by dephosphorylation and activation of both the CDK2/Cyclin A and CDK1/Cyclin B complexes[44]. Interestingly, of all three CDC25 family members,

5
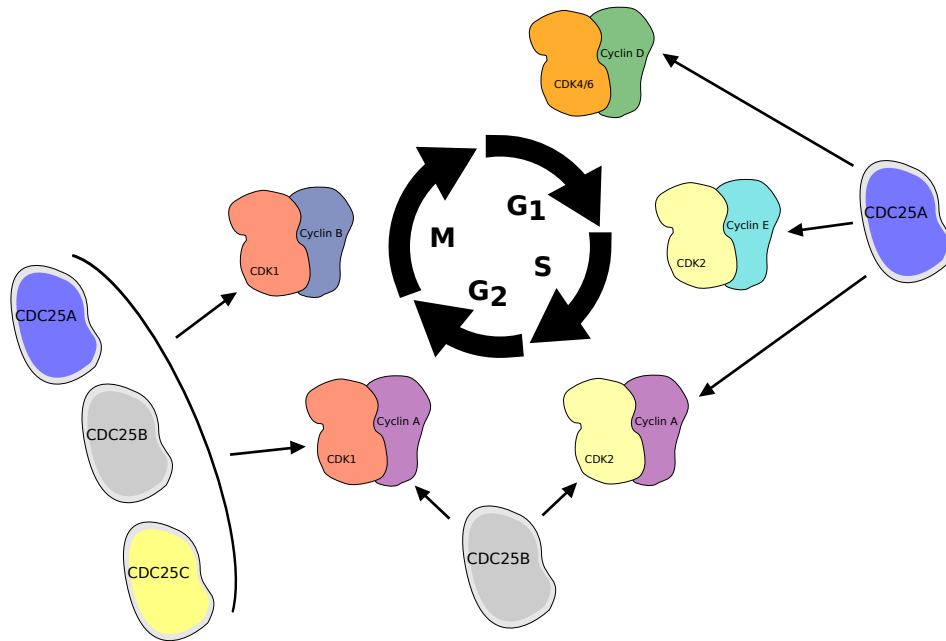
Figure 1.2 *Roles for the CDKs and CDC25s in cell cycle progression.* Schematic of how the different CDK/Cyclin complexes regulate the phases of the cell cycle. A circle representation of the cell cycle is surrounded by the CDKs and their cyclin binding partners that are active in the cell cycle phase to which they are adjacent. The CDC25s responsible for the regulation of the various CDKs are shown with arrows pointing toward their substrates.

CDC25B is required for resumption of the cell cycle after DNA damage[45]. All three CDC25s are thought to promote mitosis by dephosphorylating CDK1/Cyclin A and CDK1/Cyclin B[46,47]. Contrary to the idea of delineated roles for the individual CDC25 family members, some functional redundancy has been observed[46,48,49]. For example, mice lacking CDC25B and CDC25C are sterile but develop normally, demonstrating that CDC25A can perform all the functions required for proper cell division[50].

Given their critical role in the cell cycle, CDC25 phosphatases are subject to tight regulation from a variety of signaling pathways. CDC25 proteins are regulated through multiple mechanisms, including phosphorylation state[51,52], differential expression[53,54], subcellular

localization[55,56], and degradation[57,58]. CDC25A is primarily expressed in G1 phase and is ubiquitinylated and degraded after the completion of mitosis[41,57]. CDC25B is expressed primarily during S phase, and after the G2/M phase transition it is rapidly degraded[59,60]. The role of CDC25C appears to be primarily related to meiotic cell division[61,62], but reports have also indicated that it may have a function in both S and G2/M phases[49,63]. In addition to regulation by transcription and degradation, phosphorylation of CDC25 proteins also regulates their function throughout the cell cycle. Importantly, phosphorylation by CDK/Cyclin complexes creates feedback loops to promote cell cycle advancement. For example, phosphorylation of CDC25A by CDK2/Cyclin E in the G1/S phase transition increases its activity[64], which in further activates CDK2 leading to signal amplification and promotion of DNA synthesis. Conversely, phosphorylation of CDC25B by CDK1/Cyclin B induces the degradation of CDC25B during the progression of mitosis[65]. In addition to the role of phosphorylation of the CDC25s through normal cell division, regulation by phosphorylation is a critical mechanism for the induction of cell cycle arrest upon DNA damage. The CDC25s are substrates for Chk1 phosphorylation[66], a critical kinase in the DNA damage response pathway. Phosphorylation by Chk1 leads to the proteasome-mediated degradation or cytoplasmic sequestration of the CDC25 proteins[67,68]. Loss of the CDC25 phosphatases by either mechanism results in cell cycle arrest, which allows the cell to repair the damaged DNA before reentry into the cell cycle[45] or to induce apoptotic pathways[69]. This response is critical for the maintenance of genomic stability.

1.2.3 Recognition and activation of the CDK2/Cyclin A complex by CDC25B

Activation of the CDK2/Cyclin A complex by CDC25B is a critical step in late S phase to complete proper DNA synthesis and start the mitotic process. The molecular mechanisms

7

responsible for mediating the interaction between CDC25B and CDK2/Cyclin A have been probed by structural analysis[70], computational modeling[71], mutagenesis[72,73] and enzyme kinetics[74]. As mentioned above, the active site of CDC25 phosphatases is shallow compared to other protein tyrosine phosphatases, and phospho-peptides are poor substrates regardless of peptide sequence[75]. Compared to phospho-peptide substrates, the catalytic rate of CDC25B for its native substrate pT14pY15-CDK2/Cyclin A is approximately six-orders of magnitude faster[75]. These experiments suggest that the mode of substrate recognition occurs through alternative sites and not through the active site. Additionally, full length CDC25B protein and CDC25B protein containing just the C-terminal catalytic domain have similar activities towards pT14pY15-CDK2/Cyclin A, indicating that all essential interaction motifs for substrate recognition are present within the catalytic domain of CDC25B[70].

Though the structure of the CDC25B-CDK2/Cyclin A complex is not known, computational models of the interaction and subsequent mutagenesis have demonstrated that the protein-protein interaction is mediated primarily through two regions on CDC25B[71,72,76] (Figure 1.3). The first region is a so-called protein-protein interaction "hotspot", which is distant from
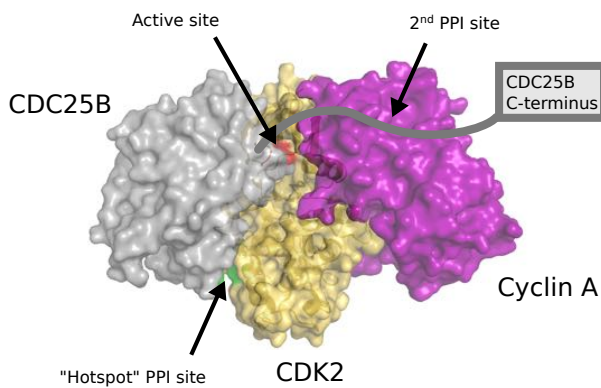
Figure 1.3 *Model of the CDC25B-CDK2/Cyclin A interaction based on computational and mutational studies.* Model of the PPI based on studies by Sohn et al.[72] CDC25B, CDK2, and Cyclin A are shown in gray, yellow, and purple respectively. The C-terminal region of CDC25B is indicated as a dark gray line. The region near the CDC25B active site is labeled and colored red. The PPI sites are also labeled, and the PPI "hotspot" region is colored green.

the active site. Mutations in this site, specifically residues R488, R492, and Y497, are highly detrimental to enzymatic activity of CDC25B towards pT14pY15-CDK2/Cyclin A, but do not affect activity toward artificial substrates[71,72,76]. For example, mutation of R492 to leucine decreases the phosphatase activity of CDC25B over 100-fold in vitro, and closely resembles the activity of a catalytically inactive mutant in vivo[72]. Similarly, mutation of two aspartic acids D206 and D210 on CDK2 also decreases the rate of dephosphorylation by CDC25B[72]. Double mutant cycles have shown that that swapping of charged residues in these sites is less detrimental than milder hotspot mutations[72], indicating that potentially these two sites may directly interact to help mediate substrate recognition. Besides this protein-protein hotspot interaction, a second region of CDC25B also helps in substrate recognition. Deletion of the 17 C-terminal residues of CDC25B decreases the pT14pY15-CDK2/Cyclin A dephosphorylation rate 10-fold[73]. Specific mutation of R556 and R562 to leucines shows a similar dephosphorylation rate as observed for the truncated protein, indicating that these residues are responsible for the majority of the catalytic benefit gained from the C-terminus[73]. The binding site of the CDC25B C-terminus on the CDK2/Cyclin A complex is unknown.

1.3 Role of CDC25 phosphatases in cancer

Due to their regulation of cell cycle checkpoints and their role in the DNA damage response, it is not surprising that the CDC25 phosphatases have been shown to play a role in cancer. Overexpression of CDC25 phosphatases is observed in a wide variety of human cancers, including ovarian[77], breast[78], liver[79], prostate[80], colorectal[81], gastric[82], thyroid[83,84], glioma[85], head and neck cancers[86], and non-Hodgkin lymphoma[87]. No reports of gene amplification or rearrangements have been reported, so the mechanism of overexpression is not entirely clear. It

has been shown for several cancers that CDC25 overexpression is due to increased CDC25 transcription from upstream oncogenic transcription factors such as Myc[53] or E2F[54]. In other cancers, CDC25 overexpression occurs through stabilization at the protein level through a suppression of degradation pathways[88]. No matter the mechanism, overexpression of CDC25A and/or CDC25B often correlates with higher tumor grades, metastatic disease, and subsequently, poor patient outcomes in many cancers[77,79,84,85,89–92].

The CDC25 phosphatases, primarily CDC25A and CDC25B, have been shown to play a role in both tumorigenesis and tumor progression. Overexpression of CDC25A or CDC25B in mouse mammary glands induces hyperplasia, but overexpression alone was not sufficient for oncogenesis[93,94]. However, in the context of either RAS or Neu overexpression, tumor-free survival in mice was almost half that of RAS or Neu overexpression alone[94]. Additionally, overexpression of CDC25B decreased mouse mammary tumor latency upon exposure to the carcinogen DMBA (7,12-dimethyl-1,2-benzanthracine)[95]. This indicates that CDC25A and CDC25B may be rate-limiting factors in RAS or Neu-driven oncogenesis in breast cancer mouse models[96]. In addition to tumor initiation, the CDC25 proteins play a role in tumor progression and maintenance. First, CDC25 proteins are downstream targets of cell growth signaling pathways, and link these pathways to cell cycle regulation[97–99]. In cancer, the constitutive expression of CDC25s promotes unregulated promotion of the cell cycle and cellular proliferation. A second critical oncogenic effect of CDC25 overexpression is the loss of DNA damage checkpoints. As outlined above, upon DNA damage CDC25 proteins are inactivated through degradation or sequestration to the cytoplasm in order to arrest the cell cycle and allow for the DNA damage to be repaired or for the induction of apoptosis. CDC25 overexpression circumnavigates the DNA damage checkpoints, promoting genomic instability[100,101]. For example, studies found that cells

in which CDC25B is overexpressed enter mitosis whether or not their DNA replication was complete[47]. In a second study, it was shown that cells with higher levels of CDC25A due to an inactive Chk2 mutation continued DNA synthesis despite exposure to ionizing radiation[102]. This insensitivity to regulatory pathways is possibly due to the increased CDC25 protein levels overwhelming the degradative or sequestration regulation mechanisms. Through several mechanisms, the involvement of the CDC25 phosphatases in cancer has indicated their therapeutic value.

1.4 Previous drug discovery efforts targeting CDC25 phosphatases

1.4.1 CDC25 phosphatases as potential anti-cancer drug targets

The CDC25 phosphatases have been considered attractive therapeutic targets for many reasons. Genetic experiments using siRNA or knockdown models suggest that the inhibition of members of the CDC25 family can slow or arrest tumor cell growth both in vitro and in vivo[103–106]. In mouse mammary tumor models, heterozygous knockout of CDC25A significantly delays tumor initiation upon expression of RAS or Neu[103]. Transcriptional repression of CDC25B in acute myeloid leukemia or expression of miRNAs targeting CDC25B in pancreatic ductal adenocarcinoma cells blocks the ability of these cells to form colonies in soft agar[104,105]. In hepatocellular carcinoma cell lines, suppression of CDC25B expression by siRNA induces cell cycle arrest in late S and G2 cell cycle phases, reduces growth rate, and reduces invasion and migration potential[106]. These cells, when subcutaneously injected into mice have a marked reduction in the rate of tumor growth[106]. Although studies have demonstrated that CDC25A is sufficient to drive the cell cycle in developing mice[50], these experimental results indicate that cancer cell growth can be dependent on either CDC25A or CDC25B overexpression.

Importantly for the development of CDC25 inhibitors, targeting the cell cycle has already been shown to be a viable therapeutic approach in cancer. Indeed, several cell cycle inhibitors have already shown promise in clinical trials[107,108]. The majority of current therapeutic agents specifically targeting the cell cycle are CDK inhibitors[109–111]. Though some efficacy has been shown for CDK inhibitors as single agents[109,112], combinations with chemotoxic agents such as letrozole[113] and mitoxantrone[114] have shown promise in phase 2 clinical trials. Approved in February 2015, the CDK4/6 inhibitor Palbociclib is the first CDK inhibitor to be approved by the FDA[115]. Despite this success, many clinical trials using CDK inhibitors have shown limited effect and significant toxicity[116–118]. These studies indicate that while inhibition of the cell cycle is a viable approach for cancer therapies, inhibitors with new mechanisms of action are needed.

1.4.2 Previous identification and characterization of CDC25 inhibitors

Due to their therapeutic value, the CDC25 phosphatases have been the target of drug discovery efforts for over twenty years[119,120]. Primarily, two approaches have been used to identify inhibitors of CDC25s. The first approach is the identification of natural product inhibitors, such as the dysidiolides and naturally occurring quinone containing compounds like vitamin K3[121–124] (Figure 1.4). The natural product inhibitors and their derivatives inhibited CDC25 phosphatases with potencies in the low to mid micro-molar range[122,123,125]; however, studies later showed that many of these compounds were either non-specific for the CDC25s compared to other protein tyrosine phosphatases[126,127] or were less potent than first reported upon retesting[128]. Despite the non-specificity of the natural products and their derivatives, several have been tested and found to be active in cancer cell lines[129,130].

Dysidiolide
87 μM

Vitamin K3
14 μM

Dnacin A1
141 μM

LGH00031
0.82 μM

IRC-083864 (Debio 0931)
0.026 μM
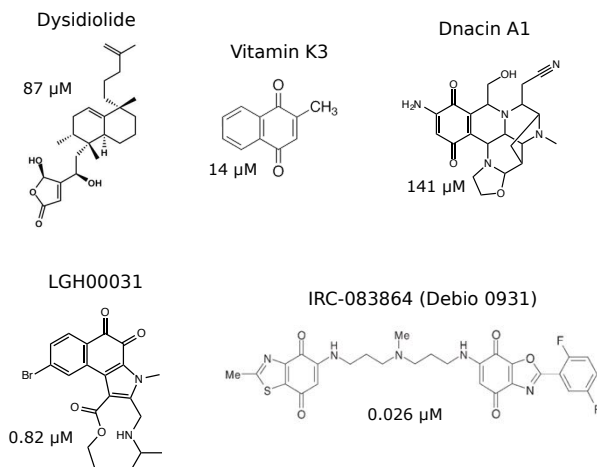
Figure 1.4. *Previously identified inhibitors of the CDC25 phosphatases.* Structures of several published inhibitors of the CDC25 family. The top three compounds are representative of inhibitor classes derived from natural products[122,125,148]. The bottom two compounds are representative synthetic inhibitors from the quinone class of compounds[138,149]. IC_{50} for CDC25B inhibition in vitro are shown.

The second major approach to CDC25 inhibitor identification, comprising the majority of drug discovery efforts, has been high-throughput screening targeting CDC25 enzymatic activity. All high-throughput screening studies to date have employed a dephosphorylation assay using an artificial substrate as a readout for CDC25 activity[131–135]. Using these high-throughput screening approaches, several lead compounds have emerged. The most successful of these compounds have been the quinone-containing class (Figure 1.4). Though these compounds have been extensively studied, their mechanisms of action are still not clear. Studies have indicated that quinone-containing compounds can inhibit the CDC25 phosphatases by covalent modification[131] or oxidation of the active site cysteine[136], thereby inhibiting enzymatic activity. This is evidenced by the fact that many of these compounds have been shown to increase intracellular reactive oxygen species, and lose activity in vitro upon the addition of a reducing agent such as DTT[135–137]. A potent bis-quinone compound IRC-083864[138] under the name Debio 0931 entered phase II clinical trials in 2009, but no data has yet been released. In all, more than 40 patents exist for CDC25 inhibitors spanning over 20 years of drug discovery efforts[119,120], yet no therapies targeting CDC25 phosphatase are currently available in the clinic.

1.5 Rationale for the development of new approaches to target CDC25 phosphatases

The CDC25 phosphatases have been validated to be of therapeutic value in cancer, and represent an alternative approach to inhibit the cell cycle. Additionally, their unique structure and biological function compared to other protein tyrosine phosphatases may allow for the development of selective inhibitors.

As detailed above, previous drug discovery efforts targeting the CDC25s have had not yet lead to any successful clinical candidates. The promiscuity of many natural product and synthetic inhibitors has made them unattractive due to potential off-target effects. Additionally, several of the current CDC25 inhibitors are reactive quinone-containing compounds or generators of reactive oxygen species, including the clinical candidate IRC-083864. As quinones have been affiliated with toxicity[139] and increased levels of reactive oxygen species are considered to play an oncogenic role in tumor biology[140,141], inhibiting CDC25 with such compounds may not be the best strategy.

The identification of reactive and non-specific inhibitors is in part due to the inherent drawbacks of previous methods used to identify CDC25 inhibitors. As mentioned above, the majority of screening approaches employed artificial substrates as readouts for inhibition of enzymatic activity. These substrates have at least two orders of magnitude slower reaction rates than are observed for the native pT14pY15-CDK2/Cyclin A substrate[75]. In addition to being poor substrates, screening with such reagents only targets the CDC25 active site. As outlined above, the CDC25 active site is shallow, confers no substrate recognition, and is the only structural motif in the CDC25s that is conserved with other protein tyrosine phosphatases. Given the nature of the CDC25 active site, it is unlikely that screening approaches targeting this site would yield

selective inhibitors. In addition, no structural or biophysical characterization for any of the previously identified inhibitors has been published, leaving their complete mechanism of action unclear.

For these reasons, we proposed to inhibit CDC25B by blocking its interaction with CDK2/Cyclin A. As opposed to previous studies, we employed biophysical and chemical biology approaches to identify and characterize CDC25B inhibitors. Additionally, instead of using artificial substrates to identify CDC25B inhibitors our studies focused on using a biologically relevant substrate, the CDK2/Cyclin A complex. The proposed approach of targeting the CDC25B-CDK2/Cyclin A protein-protein interaction has two primary advantages over previous attempts to identify CDC25B inhibitors. First, targeting the CDC25B-CDK2/ Cyclin A protein-protein interaction instead of CDC25B catalytic activity addresses the bias towards targeting the shallow active site of CDC25B that is inherent in all previous inhibitor discovery efforts. Inhibitors identified using this approach do not target a specific binding site and can bind to any site on CDC25B or the CDK2/Cyclin A complex responsible for mediating the protein-protein interaction. Second, this approach is much less sensitive to oxidizing agents such as the quinone-containing class of CDC25B inhibitors. As stated above, many previously identified compounds inhibit CDC25B activity by oxidizing the catalytic cysteine of CDC25B through the generation of intracellular reactive oxygen species. By screening for inhibitors of the CDC25B-CDK2/Cyclin A protein-protein interaction instead of CDC25B catalytic activity inhibitors, the bias of previous screens towards the identification of oxidizing agents is removed. This is important because many of the CDC25B inhibitors that are active through oxidation of the catalytic cysteine are from the quinone-containing class of compounds, which have been associated with toxicity in vivo[139].

In addition to the advantages of targeting the CDC25B-CDK2/Cyclin A interaction, inhibitors identified using this approach may have advantages over previously characterized CDC25B inhibitors. One of the limiting factors of previously described CDC25B has been their toxicity, likely caused by their non-specific reactivity or their generation of intracellular reactive oxygen species. Due to the removal of the bias towards the identification of inhibitors that oxidize the highly reactive CDC25B catalytic cysteine, inhibitors identified by targeting the CDC25B-CDK2/Cyclin A protein-protein interaction may be less likely to be oxidizing agents. Identification of compounds with a mechanism of inhibition other than oxidation of the CDC25B catalytic cysteine may be less toxic than previously identified inhibitors.

In addition to limiting the toxicity of CDC25B inhibitors by targeting the CDC25B-CDK2/Cyclin A interaction instead of CDC25B catalytic activity, inhibitors of the protein-protein interaction may exhibit increased specificity for CDC25B. As described above, the active sites of the CDC25 family members are the only structural motifs shared with all other protein phosphatases and are very shallow compared to other protein phosphatases. For this reason it is unlikely that compounds targeting the active sites of the CDC25 family could be highly specific. However, the rest of the structure of the CDC25 family members is unique compared to all other protein phosphatases. Therefore targeting sites other than the active site on CDC25B may represent a better approach towards the development of specific CDC25B inhibitors. A specific inhibitor of CDC25B or an inhibitor specific to the CDC25 family would be a useful tool for understanding the biology of these important phosphatases, as well as potentially being useful for more targeted therapies.

Notes

Many of the topics presented here have been well reviewed and deserve acknowledgment. The roles of the CDKs in normal and cancer biology have been well described by Malumbres et al[6]; the role of the CDC25 family in cancer and their value as therapeutic targets has been reviewed by Buotros et al.[142,143], Kiyokawa et al.[144], Rudolph[145], and Lazo[146]; the structure and function of the CDC25 phosphatases has been reviewed by Rudolph[147]; patent reviews of CDC25 inhibitors have been written by Lavecchia et al.[119,120].

1.6 References

1. John, P. C., Mews, M. & Moore, R. Cyclin/Cdk complexes: their involvement in cell cycle progression and mitotic division. *Protoplasma* **216,** 119–42 (2001).

2. Tanaka, S. & Araki, H. Regulation of the initiation step of DNA replication by cyclin-dependent kinases. *Chromosoma* **119,** 565–74 (2010).

3. Li, C., Vassilev, A. & DePamphilis, M. L. Role for Cdk1 (Cdc2)/cyclin A in preventing the mammalian origin recognition complex's largest subunit (Orc1) from binding to chromatin during mitosis. *Mol. Cell. Biol.* **24,** 5875–86 (2004).

4. Malumbres, M. & Barbacid, M. Cell cycle, CDKs and cancer: a changing paradigm. *Nat. Rev. Cancer* **9,** 153–66 (2009).

5. Malumbres, M. *et al.* Cyclin-dependent kinases: a family portrait. *Nat. Cell Biol.* **11,** 1275–6 (2009).

6. Malumbres, M. & Barbacid, M. Cell cycle, CDKs and cancer: a changing paradigm. *Nat. Rev. Cancer* **9,** 153–66 (2009).

7. Lee, M. G. & Nurse, P. Complementation used to clone a human homologue of the fission yeast cell cycle control gene cdc2. *Nature* **327,** 31–35 (1987).

8. Morgan, D. O. Cyclin-dependent kinases: engines, clocks, and microprocessors. *Annu. Rev. Cell Dev. Biol.* **13,** 261–91 (1997).

9. Jeffrey, P. D. *et al.* Mechanism of CDK activation revealed by the structure of a cyclinA-CDK2 complex. *Nature* **376,** 313–320 (1995).

10. Schulman, B. A., Lindstrom, D. L. & Harlow, E. Substrate recruitment to cyclin-dependent kinase 2 by a multipurpose docking site on cyclin A. *Proc. Natl. Acad. Sci.* **95,** 10453–10458 (1998).

11. Brown, N. R., Noble, M. E., Endicott, J. a & Johnson, L. N. The structural basis for specificity of substrate and recruitment peptides for cyclin-dependent kinases. *Nat. Cell Biol.* **1,** 438–443 (1999).

12. Stevenson, L. M., Deal, M. S., Hagopian, J. C. & Lew, J. Activation Mechanism of CDK2: Role of Cyclin Binding versus Phosphorylation †. *Biochemistry* **41,** 8528–8534 (2002).

13. Hagopian, J. C. *et al.* Kinetic basis for activation of CDK2/cyclin A by phosphorylation. *J. Biol. Chem.* **276,** 275–80 (2001).

14. Den Haese, G. J., Walworth, N., Carr, A. M. & Gould, K. L. The Wee1 protein kinase regulates T14 phosphorylation of fission yeast Cdc2. *Mol. Biol. Cell* **6,** 371–85 (1995).

15. Booher, R. N., Holman, P. S. & Fattaey, A. Human Myt1 Is a Cell Cycle-regulated Kinase That Inhibits Cdc2 but Not Cdk2 Activity. *J. Biol. Chem.* **272,** 22300–22306 (1997).

16. Welburn, J. P. I. *et al.* How tyrosine 15 phosphorylation inhibits the activity of

cyclin-dependent kinase 2-cyclin A. *J. Biol. Chem.* **282,** 3173–81 (2007).

17. Bártová, I., Otyepka, M., Kríz, Z. & Koca, J. Activation and inhibition of cyclin-dependent kinase-2 by phosphorylation; a molecular dynamics study reveals the functional importance of the glycine-rich loop. *Protein Sci.* **13,** 1449–57 (2004).

18. Krämer, A. *et al.* Centrosome-associated Chk1 prevents premature activation of cyclin-B-Cdk1 kinase. *Nat. Cell Biol.* **6,** 884–891 (2004).

19. Sexl, V. *et al.* A rate limiting function of cdc25A for S phase entry inversely correlates with tyrosine dephosphorylation of Cdk2. *Oncogene* **18,** 573–582 (1999).

20. Bao, Z. Q., Jacobsen, D. M. & Young, M. A. Briefly bound to activate: transient binding of a second catalytic magnesium activates the structure and dynamics of CDK2 kinase for catalysis. *Structure* **19,** 675–90 (2011).

21. Jacobsen, D. M., Bao, Z.-Q., O'Brien, P., Brooks, C. L. & Young, M. A. Price to be paid for two-metal catalysis: magnesium ions that accelerate chemistry unavoidably limit product release from a protein kinase. *J. Am. Chem. Soc.* **134,** 15357–70 (2012).

22. Sherr, C. J. & Roberts, J. M. CDK inhibitors: positive and negative regulators of G1-phase progression. *Genes Dev.* **13,** 1501–1512 (1999).

23. Malumbres, M. & Barbacid, M. Mammalian cyclin-dependent kinases. *Trends Biochem. Sci.* **30,** 630–41 (2005).

24. Malumbres, M. & Barbacid, M. To cycle or not to cycle: a critical decision in cancer. *Nat. Rev. Cancer* **1,** 222–31 (2001).

25. Clurman, B. E., Sheaff, R. J., Thress, K., Groudine, M. & Roberts, J. M. Turnover of cyclin E by the ubiquitin-proteasome pathway is regulated by cdk2 binding and cyclin phosphorylation. *Genes Dev.* **10,** 1979–1990 (1996).

26. Meraldi, P., Lukas, J., Fry, A. M., Bartek, J. & Nigg, E. A. Centrosome duplication in mammalian somatic cells requires E2F and Cdk2-cyclin A. *Nat. Cell Biol.* **1,** 88–93 (1999).

27. Ruffner, H., Jiang, W., Craig, A. G., Hunter, T. & Verma, I. M. BRCA1 is phosphorylated at serine 1497 in vivo at a cyclin-dependent kinase 2 phosphorylation site. *Mol. Cell. Biol.* **19,** 4843–54 (1999).

28. Chen, Q., Zhang, X., Jiang, Q., Clarke, P. R. & Zhang, C. Cyclin B1 is localized to unattached kinetochores and contributes to efficient microtubule attachment and proper chromosome alignment during mitosis. *Cell Res.* **18,** 268–80 (2008).

29. Tin Su, T. Cell cycle: How, when and why cells get rid of cyclin A. *Curr. Biol.* **11,** R467–R469 (2001).

30. Abe, S. *et al.* The initial phase of chromosome condensation requires Cdk1-mediated phosphorylation of the CAP-D3 subunit of condensin II. *Genes Dev.* **25,** 863–74 (2011).

31. Santamaría, D. *et al.* Cdk1 is sufficient to drive the mammalian cell cycle. *Nature* **448,** 811–5 (2007).

32. Alonso, A. *et al.* Protein Tyrosine Phosphatases in the Human Genome. *Cell* **117,** 699–711 (2004).

33. Wegener, S., Hampe, W., Herrmann, D. & Schaller, H. C. Alternative splicing in the regulatory region of the human phosphatases CDC25A and CDC25C. *Eur. J. Cell Biol.* **79,** 810–5 (2000).

34. Baldin, V., Cans, C., Superti-Furga, G. & Ducommun, B. Alternative splicing of the human CDC25B tyrosine phosphatase. Possible implications for growth control? *Oncogene* **14,** 2485–2495 (1997).

35. Fauman, E. B. *et al.* Crystal structure of the catalytic domain of the human cell cycle control phosphatase, Cdc25A. *Cell* **93,** 617–25 (1998).

36. Reynolds, R. A. *et al.* Crystal structure of the catalytic subunit of Cdc25B required for G2/M phase transition of the cell cycle. *J. Mol. Biol.* **293,** 559–68 (1999).

37. Kim, Y. . W. A. . H. C. . S. P. . J. C. . B. L. . B. A. . V. M. . M. J. . W. J. . A. C. H. . E. A. . B. C. . G. O. . von D. F. . K. S. . J. A. Crystal Structure of Cell Division Cycle 25C Protein Isoform A from Homo sapiens. *TO BE Publ.* at <http://www.rcsb.org/pdb/explore/explore.do?structureId=3OP3>

38. Wang, Z., Zhang, B., Wang, M. & Carr, B. I. Cdc25A and ERK interaction: EGFR-independent ERK activation by a protein phosphatase Cdc25A inhibitor, compound 5. *J. Cell. Physiol.* **204,** 437–44 (2005).

39. Wang, Z. Identification of Epidermal Growth Factor Receptor as a Target of Cdc25A Protein Phosphatase. *J. Biol. Chem.* **277,** 19470–19475 (2002).

40. Blomberg, I. & Hoffmann, I. Ectopic expression of Cdc25A accelerates the G(1)/S transition and leads to premature activation of cyclin E- and cyclin A-dependent kinases. *Mol. Cell. Biol.* **19,** 6183–94 (1999).

41. Jinno, S. *et al.* Cdc25A is a novel phosphatase functioning early in the cell cycle. *EMBO J.* **13,** 1549–1556 (1994).

42. Iavarone, A. & Massagué, J. Repression of the CDK activator Cdc25A and cell-cycle arrest by cytokine TGF-beta in cells lacking the CDK inhibitor p15. *Nature* **387,** 417–22 (1997).

43. Bugler, B., Schmitt, E., Aressy, B. & Ducommun, B. Unscheduled expression of CDC25B in S-phase leads to replicative stress and DNA damage. *Mol. Cancer* **9,** 29 (2010).

44. Goldstone, S., Pavey, S., Forrest, A., Sinnamon, J. & Gabrielli, B. Cdc25-dependent activation of cyclin A/cdk2 is blocked in G2 phase arrested cells independently of ATM/ATR. *Oncogene* **20,** 921–32 (2001).

45. Bansal, P. & Lazo, J. S. Induction of Cdc25B regulates cell cycle resumption after genotoxic stress. *Cancer Res.* **67,** 3356–3363 (2007).

46. Lindqvist, A., Källström, H., Lundgren, A., Barsoum, E. & Rosenthal, C. K. Cdc25B cooperates with Cdc25A to induce mitosis but has a unique role in activating cyclin B1–Cdk1 at the centrosome. *J. Cell Biol.* **171,** 35–45 (2005).

47. Karlsson, C., Katich, S., Hagting, A., Hoffmann, I. & Pines, J. Cdc25B and Cdc25C Differ Markedly in their Properties as Initiators of Mitosis. *J. cell …* **146,** (1999).

48. Garner-Hamrick, P. A. & Fisher, C. Antisense phosphorothioate oligonucleotides specifically down-regulate cdc25B causing S-phase delay and persistent antiproliferative effects. *Int. J. Cancer* **76,** 720–728 (1998).

49. Turowski, P. *et al.* Functional cdc25C dual-specificity phosphatase is required for S-phase entry in human cells. *Mol. Biol. Cell* **14,** 2984–2998 (2003).

50. Ferguson, A. M., White, L. S., Donovan, P. J. & Piwnica-Worms, H. Normal cell cycle and checkpoint responses in mice and cells lacking Cdc25B and Cdc25C protein phosphatases. *Mol. Cell. Biol.* **25,** 2853–2860 (2005).

51. Cazales, M. *et al.* CDC25B phosphorylation by Aurora-A occurs at the G2/M transition and is inhibited by DNA damage. *Cell Cycle* **4,** 1233–1238 (2005).

52. Theis-Febvre, N. *et al.* Protein kinase CK2 regulates CDC25B phosphatase activity. *Oncogene* **22,** 220–232 (2003).

53. Galaktionov, K., Chen, X. & Beach, D. Cdc25 cell-cycle phosphatase as a target of c-myc. *Nature* **382,** 511–517 (1996).

54. Vigo, E. *et al.* CDC25A phosphatase is a target of E2F and is required for efficient E2F-induced S phase. *Mol. Cell. Biol.* **19,** 6379–6395 (1999).

55. Kumagai, A., Yakowec, P. S. & Dunphy, W. G. 14-3-3 proteins act as negative regulators of the mitotic inducer Cdc25 in Xenopus egg extracts. *Mol. Biol. Cell* **9,** 345–354 (1998).

56. Lopez-Girona, A., Furnari, B., Mondesert, O. & Russell, P. Nuclear localization of Cdc25 is regulated by DNA damage and a 14-3-3 protein. *Nature* **397,** 172–5 (1999).

57. Donzelli, M. *et al.* Dual mode of degradation of Cdc25 A phosphatase. *EMBO J.* **21,** 4875–4884 (2002).

58. Uchida, S. *et al.* SCFβ(TrCP) mediates stress-activated MAPK-induced Cdc25B degradation. *J. Cell Sci.* **124,** 2816–2825 (2011).

59. Gabrielli, B. G. *et al.* Cytoplasmic accumulation of cdc25B phosphatase in mitosis triggers centrosomal microtubule nucleation in HeLa cells. *J. Cell Sci.* **109 (Pt 5,** 1081–1093 (1996).

60. Kieffer, I., Lorenzo, C., Dozier, C., Schmitt, E. & Ducommun, B. Differential mitotic degradation of the CDC25B phosphatase variants. *Oncogene* **26,** 7847–7858 (2007).

61. Dai, Y., Lee, C., Hutchings, A., Sun, Y. & Moor, R. Selective requirement for Cdc25C protein synthesis during meiotic progression in porcine oocytes. *Biol. Reprod.* **62,** 519–32 (2000).

62. Perdiguero, E. & Nebreda, A. R. Regulation of Cdc25C activity during the meiotic G2/M transition. *Cell Cycle* **3,** 733–7 (2004).

63. Strausfeld, U. *et al.* Activation of p34cdc2 protein kinase by microinjection of human cdc25C into mammalian cells. Requirement for prior phosphorylation of cdc25C by

p34cdc2 on sites phosphorylated at mitosis. *J. Biol. Chem.* **269,** 5989–6000 (1994).

64. Hoffmann, I., Draetta, G. & Karsenti, E. Activation of the phosphatase activity of human cdc25A by a cdk2-cyclin E dependent phosphorylation at the G1/S transition. *EMBO J.* **13,** 4302–4310 (1994).

65. Baldin, V., Cans, C., Knibiehler, M. & Ducommun, B. Phosphorylation of human CDC25B phosphatase by CDK1-cyclin A triggers its proteasome-dependent degradation. *J. Biol. Chem.* **272,** 32731–32734 (1997).

66. Sanchez, Y., Wong, C., Thoma, R. & Richman, R. Conservation of the Chk1 checkpoint pathway in mammals: linkage of DNA damage to Cdk regulation through Cdc25. *Science (80-.).* **277,** 1497–1501 (1997).

67. Xiao, Z. *et al.* Chk1 mediates S and G2 arrests through Cdc25A degradation in response to DNA-damaging agents. *J. Biol. Chem.* **278,** 21767–21773 (2003).

68. Schmitt, E. *et al.* CHK1 phosphorylates CDC25B during the cell cycle in the absence of DNA damage. *J. Cell Sci.* **119,** 4269–4275 (2006).

69. Yanagida, J. *et al.* Accelerated elimination of ultraviolet-induced DNA damage through apoptosis in CDC25A-deficient skin. *Carcinogenesis* **33,** 1754–61 (2012).

70. Rudolph, J. Cdc25 phosphatases: structure, specificity, and mechanism. *Biochemistry* **46,** 3595–604 (2007).

71. Sohn, J. & Rudolph, J. The energetic network of hotspot residues between Cdc25B phosphatase and its protein substrate. *J. Mol. Biol.* **22,** 4109 (2008).

72. Sohn, J., Parks, J. & Buhrman, G. Experimental validation of the docking orientation of Cdc25 with its Cdk2-CycA protein substrate. *Biochemistry* **44,** 16563–16573 (2005).

73. Wilborn, M., Free, S., Ban, A. & Rudolph, J. The C-terminal tail of the dual-specificity Cdc25B phosphatase mediates modular substrate recognition. *Biochemistry* **40,** 14200–14206 (2001).

74. Chen, W., Wilborn, M. & Rudolph, J. Dual-specific Cdc25B phosphatase: in search of the catalytic acid. *Biochemistry* **39,** 10781–10789 (2000).

75. Rudolph, J., Epstein, D., Parker, L. & Eckstein, J. Specificity of natural and artificial substrates for human Cdc25A. *Anal. Biochem.* **289,** 43–51 (2001).

76. Sohn, J., Buhrman, G. & Rudolph, J. Kinetic and structural studies of specific protein-protein interactions in substrate catalysis by Cdc25B phosphatase. *Biochemistry* **46,** 807–818 (2007).

77. Broggini, M. *et al.* Cell cycle-related phosphatases CDC25A and B expression correlates with survival in ovarian cancer patients. *Anticancer Res.* **20,** 4835–40

78. Ito, Y. *et al.* Expression of cdc25A and cdc25B phosphatase in breast carcinoma. *Breast Cancer* **11,** 295–300 (2004).

79. Xu, X. *et al.* Overexpression of CDC25A phosphatase is associated with hypergrowth activity and poor prognosis of human hepatocellular carcinomas. *Clin. Cancer Res.* **9,**

1764–72 (2003).

80.   Ngan, E. S. W., Hashimoto, Y., Ma, Z.-Q., Tsai, M.-J. & Tsai, S. Y. Overexpression of Cdc25B, an androgen receptor coactivator, in prostate cancer. *Oncogene* **22,** 734–9 (2003).

81.   Dixon, D., Moyana, T. & King, M. J. Elevated expression of the cdc25A protein phosphatase in colon cancer. *Exp. Cell Res.* **240,** 236–243 (1998).

82.   Xing, X., Chen, J. & Chen, M. Expression of CDC25 phosphatases in human gastric cancer. *Dig. Dis. Sci.* **53,** 949–953 (2008).

83.   Ito, Y. *et al.* Expression of cdc25A and cdc25B proteins in thyroid neoplasms. *Br. J. Cancer* **86,** 1909–13 (2002).

84.   Ito, Y. *et al.* Expression of cdc25B and cdc25A in medullary thyroid carcinoma: cdc25B expression level predicts a poor prognosis. *Cancer Lett.* **229,** 291–7 (2005).

85.   Nakabayashi, H., Hara, M. & Shimizu, K. Prognostic significance of CDC25B expression in gliomas. *J. Clin. Pathol.* **59,** 725–8 (2006).

86.   Gasparotto, D. *et al.* Overexpression of CDC25A and CDC25B in head and neck cancers. *Cancer Res.* **57,** 2366–2368 (1997).

87.   Hernández, S. *et al.* cdc25 cell cycle-activating phosphatases and c-myc expression in human non-Hodgkin's lymphomas. *Cancer Res.* **58,** 1762–1767 (1998).

88.   He, N. *et al.* Regulation of lung cancer cell growth and invasiveness by beta-TRCP. *Mol. Carcinog.* **42,** 18–28 (2005).

89.   Zhang, Z., Zhang, G. & Kong, C. High expression of Cdc25B and low expression of 14-3-3σ is associated with the development and poor prognosis in urothelial carcinoma of bladder. *Tumour Biol.* **35,** 2503–12 (2014).

90.   Sasaki, H. *et al.* Expression of the cdc25B gene as a prognosis marker in non-small cell lung cancer. *Cancer Lett.* **173,** 187–92 (2001).

91.   Takemasa, I. *et al.* Overexpression of CDC25B phosphatase as a novel marker of poor prognosis of human colorectal carcinoma. *Cancer Res.* **60,** 3043–50 (2000).

92.   Xu, X. *et al.* Overexpression of CDC25A phosphatase is associated with hypergrowth activity and poor prognosis of human hepatocellular carcinomas. *Clin. Cancer Res.* **9,** 1764–1772 (2003).

93.   Ma, Z. Q., Chua, S. S., DeMayo, F. J. & Tsai, S. Y. Induction of mammary gland hyperplasia in transgenic mice over-expressing human Cdc25B. *Oncogene* **18,** 4564–4576 (1999).

94.   Ray, D. *et al.* Deregulated CDC25A expression promotes mammary tumorigenesis with genomic instability. *Cancer Res.* **67,** 984–991 (2007).

95.   Yao, Y., Slosberg, E., Wang, L. & Hibshoosh, H. Increased susceptibility to carcinogen-induced mammary tumors in MMTV-Cdc25B transgenic mice. *Oncogene* **18,** 5159–5166 (1999).

96.   Ray, D. & Kiyokawa, H. CDC25A phosphatase: A rate-limiting oncogene that

determines genomic stability. *Cancer Res.* **68,** 1251–1253 (2008).

97.   Galaktionov, K., Jessus, C. & Beach, D. Raf1 interaction with Cdc25 phosphatase ties mitogenic signal transduction to cell cycle activation. *Genes Dev.* **9,** 1046–1058 (1995).

98.   Brunetto, E. *et al.* CDC25A protein stability represents a previously unrecognized target of HER2 signaling in human breast cancer: implication for a potential clinical relevance in trastuzumab treatment. *Neoplasia* **15,** 579–90 (2013).

99.   Guo, S.-L. *et al.* Akt-p53-miR-365-cyclin D1/cdc25A axis contributes to gastric tumorigenesis induced by PTEN deficiency. *Nat. Commun.* **4,** 2544 (2013).

100.   Molinari, M., Mercurio, C., Dominguez, J., Goubin, F. & Draetta, G. F. Human Cdc25 A inactivation in response to S phase inhibition and its role in preventing premature mitosis. *EMBO Rep.* **1,** 71–79 (2000).

101.   Zhao, H., Watkins, J. L. & Piwnica-Worms, H. Disruption of the checkpoint kinase 1/ cell division cycle 25A pathway abrogates ionizing radiation-induced S and G2 checkpoints. *Proc. Natl. Acad. Sci. U. S. A.* **99,** 14795–800 (2002).

102.   Falck, J., Mailand, N., Syljuåsen, R. G., Bartek, J. & Lukas, J. The ATM-Chk2-Cdc25A checkpoint pathway guards against radioresistant DNA synthesis. *Nature* **410,** 842–847 (2001).

103.   Ray, D. *et al.* Hemizygous disruption of Cdc25A inhibits cellular transformation and mammary tumorigenesis in mice. *Cancer Res.* **67,** 6605–6611 (2007).

104.   Nakamura, S. *et al.* Transcriptional repression of Cdc25B by IER5 inhibits the proliferation of leukemic progenitor cells through NF-YB and p300 in acute myeloid leukemia. *PLoS One* **6,** e28011 (2011).

105.   Liffers, S.-T. *et al.* MicroRNA-148a is down-regulated in human pancreatic ductal adenocarcinomas and regulates cell survival by targeting CDC25B. *Lab. Invest.* **91,** 1472–9 (2011).

106.   Yan, X., Chua, M., He, J. & So, S. Small interfering RNA targeting CDC25B inhibits liver tumor growth in vitro and in vivo. *Mol Cancer* **7,** 19 (2008).

107.   Schwartz, G. K. *et al.* Phase i study of barasertib (AZD1152), a selective inhibitor of Aurora B kinase, in patients with advanced solid tumors. *Invest. New Drugs* **31,** 370–380 (2013).

108.   Olmos, D. *et al.* Phase I study of GSK461364, a specific and competitive Polo-like kinase 1 inhibitor, in patients with advanced solid malignancies. *Clin. Cancer Res.* **17,** 3420–3430 (2011).

109.   Dispenzieri, A. *et al.* Flavopiridol in patients with relapsed or refractory multiple myeloma: a phase 2 trial with clinical and pharmacodynamic end-points. *Haematologica* **91,** 390–393 (2006).

110.   Geoffrey I. Shapiro, John Hilton, James M. Cleary, Sara M. Tolaney, Leena Ghandi, Eunice L. Kwak, Jeffrey W. Clark, Andrew Wolanski, Tracy Bell, John Schulz, Sheelagh Frame, Chiara Saladino, Morag Hogben, Scott J. Rodig, Judy H. Chiao, D.

B. Responses to sequential sapacitabine and seliciclib in patients with BRCA-deficient solid tumors. *AACR 2013* **LB-202,** 98112 (2013).

111. Hofmeister, C. C. *et al.* A phase I trial of flavopiridol in relapsed multiple myeloma. *Cancer Chemother. Pharmacol.* **73,** 249–257 (2014).

112. S.K., K. *et al.* Phase 1/2 trial of a novel CDK inhibitor dinaciclib (SCH727965) in patients with relapsed multiple myeloma demonstrates encouraging single agent activity. *Blood* **120,** (2012).

113. Finn, R. *et al.* Results of a randomized phase 2 study of PD 0332991, a cyclin-dependent kinase (CDK) 4/6 inhibitor, in combination with letrozole vs letrozole alone for first-line treatment of ER+/HER2- advanced breast cancer (BC). *Cancer Res.* **72,** S1–6–S1–6 (2012).

114. Karp, J. E. *et al.* Randomized phase II study of two schedules of flavopiridol given as timed sequential therapy with cytosine arabinoside and mitoxantrone for adults with newly diagnosed, poor-risk acute myelogenous leukemia. *Haematologica* **97,** 1736–42 (2012).

115. Research, C. for D. E. and. Approved Drugs - Palbociclib. at <http://www.fda.gov/Drugs/InformationOnDrugs/ApprovedDrugs/ucm432886.htm>

116. DeMichele, A. *et al.* CDK 4/6 Inhibitor Palbociclib (PD0332991) in Rb+ Advanced Breast Cancer: Phase II Activity, Safety, and Predictive Biomarker Assessment. *Clin. Cancer Res.* **21,** 995–1001 (2015).

117. Chen, E. X. *et al.* A Phase I study of cyclin-dependent kinase inhibitor, AT7519, in patients with advanced cancer: NCIC Clinical Trials Group IND 177. *Br. J. Cancer* **111,** 2262–7 (2014).

118. Mita, M. M. *et al.* Randomized phase II trial of the cyclin-dependent kinase inhibitor dinaciclib (MK-7965) versus capecitabine in patients with advanced breast cancer. *Clin. Breast Cancer* **14,** 169–76 (2014).

119. Lavecchia, A., Di Giovanni, C. & Novellino, E. Inhibitors of Cdc25 phosphatases as anticancer agents: a patent review. *Expert Opin. Ther. Pat.* **20,** 405–25 (2010).

120. Lavecchia, A., Di Giovanni, C. & Novellino, E. CDC25 phosphatase inhibitors: an update. *Mini Rev. Med. Chem.* **12,** 62–73 (2012).

121. Gunasekera, S. P., McCarthy, P. J., Kelly-Borges, M., Lobkovsky, E. & Clardy, J. Dysidiolide: A novel protein phosphatase inhibitor from the Caribbean sponge Dyside A etheria de Laubenfels. *J. Am. Chem. Soc.* **118,** 8759–8760 (1996).

122. Horiguchi, T. *et al.* Dnacin A1 and dnacin B1 are antitumor antibiotics that inhibit cdc25B phosphatase activity. *Biochem. Pharmacol.* **48,** 2139–41 (1994).

123. Brisson, M. *et al.* Independent mechanistic inhibition of cdc25 phosphatases by a natural product caulibugulone. *Mol. Pharmacol.* **71,** 184–92 (2007).

124. Wu, F. Y. & Sun, T. P. Vitamin K3 induces cell cycle arrest and cell death by inhibiting Cdc25 phosphatase. *Eur. J. Cancer* **35,** 1388–93 (1999).

125. Takahashi, M. *et al.* Synthesis of the novel analogues of dysidiolide and their structure–activity relationship. *Bioorg. Med. Chem. Lett.* **10,** 2571–2574 (2000).

126. Rice, R. L. *et al.* A targeted library of small-molecule, tyrosine, and dual-specificity phosphatase inhibitors derived from a rational core design and random side chain variation. *Biochemistry* **36,** 15965–74 (1997).

127. Ducruet, A. P. *et al.* Identification of new Cdc25 dual specificity phosphatase inhibitors in a targeted small molecule array. *Bioorg. Med. Chem.* **8,** 1451–1466 (2000).

128. Blanchard, J. L., Epstein, D. M., Boisclair, M. D., Rudolph, J. & Pal, K. Dysidiolide and related gamma-hydroxy butenolide compounds as inhibitors of the protein tyrosine phosphatase, CDC25. *Bioorg. Med. Chem. Lett.* **9,** 2537–2538 (1999).

129. Aoyagi, Y. *et al.* A novel cinnamic acid derivative that inhibits Cdc25 dual-specificity phosphatase activity. *Cancer Sci.* **96,** 614–9 (2005).

130. Nishikawa, Y. *et al.* Growth inhibition of hepatoma cells induced by vitamin K and its analogs. *J. Biol. Chem.* **270,** 28304–28310 (1995).

131. Pu, L., Amoscato, A. A., Bier, M. E. & Lazo, J. S. Dual G1 and G2 phase inhibition by a novel, selective Cdc25 inhibitor 6-chloro-7-[corrected](2-morpholin-4-ylethylamino)-quinoline-5,8-dione. *J. Biol. Chem.* **277,** 46877–85 (2002).

132. Lazo, J. S. *et al.* Identification of a potent and selective pharmacophore for Cdc25 dual specificity phosphatase inhibitors. *Mol. Pharmacol.* **61,** 720–8 (2002).

133. Zhou, Y. *et al.* LGH00031, a novel ortho-quinonoid inhibitor of cell division cycle 25B, inhibits human cancer cells via ROS generation. *Acta Pharmacol. Sin.* **30,** 1359–68 (2009).

134. Kim, K.-R. *et al.* EK-6136 (3-methyl-4-(O-methyl-oximino)-1-phenylpyrazolin-5-one): a novel Cdc25B inhibitor with antiproliferative activity. *Eur. J. Pharmacol.* **528,** 37–42 (2005).

135. Johnston, P. A. *et al.* Cdc25B dual-specificity phosphatase inhibitors identified in a high-throughput screen of the NIH compound library. *Assay Drug Dev. Technol.* **7,** 250–65 (2009).

136. Brisson, M. *et al.* Redox regulation of Cdc25B by cell-active quinolinediones. *Mol. Pharmacol.* **68,** 1810–20 (2005).

137. Lavecchia, A. *et al.* Discovery of new inhibitors of Cdc25B dual specificity phosphatases by structure-based virtual screening. *J. Med. Chem.* **55,** 4142–58 (2012).

138. Brezak, M.-C. *et al.* IRC-083864, a novel bis quinone inhibitor of CDC25 phosphatases active against human cancer cells. *Int. J. Cancer* **124,** 1449–56 (2009).

139. Bolton, J. L., Trush, M. A., Penning, T. M., Dryhurst, G. & Monks, T. J. Role of quinones in toxicology. *Chem. Res. Toxicol.* **13,** 135–60 (2000).

140. Waris, G. & Ahsan, H. Reactive oxygen species: role in the development of cancer

and various chronic conditions. *J. Carcinog.* **5,** 14 (2006).

141.   Liou, G.-Y. & Storz, P. Reactive oxygen species in cancer. *Free Radic. Res.* **44,** 479–96 (2010).

142.   Boutros, R., Dozier, C. & Ducommun, B. The when and wheres of CDC25 phosphatases. *Curr. Opin. Cell Biol.* **18,** 185–91 (2006).

143.   Boutros, R., Lobjois, V. & Ducommun, B. CDC25 phosphatases in cancer cells: key players? Good targets? *Nat. Rev. Cancer* **7,** 495–507 (2007).

144.   Kiyokawa, H. & Ray, D. In vivo roles of CDC25 phosphatases: Biological insight into the anti-cancer therapeutic targets. *Brain Behav. Immun.* **22,** 4109 (2008).

145.   Rudolph, J. Inhibiting transient protein–protein interactions: lessons from the Cdc25 protein tyrosine phosphatases. *Nat. Rev. Cancer* **7,** 202–11 (2007).

146.   Lazo, J. S. & Wipf, P. Is Cdc25 a druggable target? *Anticancer. Agents Med. Chem.* **8,** 837–42 (2008).

147.   Rudolph, J. Cdc25 phosphatases: structure, specificity, and mechanism. *Biochemistry* **46,** (2007).

148.   Brezak, M.-C. *et al.* A novel synthetic inhibitor of CDC25 phosphatases: BN82002. *Cancer Res.* **64,** 3320–5 (2004).

149.   Feng, X. *et al.* Discovery and characterization of a novel inhibitor of CDC25B, LGH00045. *Acta Pharmacol. Sin.* **29,** 1268–74 (2008).

Chapter 2

Characterization of CDC25B-CDK2/CycA-Mre11 interactions using biochemical and biophysical methods

2.1 Abstract

Activation of CDK/Cyclin complexes is a critical step in cell cycle progression, and their aberrant regulation occurs in many cancers. The CDC25B phosphatase is a critical regulator of CDK2/Cyclin A and has been validated as an important therapeutic target in cancer. Recently the DNA double strand break repair protein Mre11 has also been shown to interact directly with CDK2/Cyclin A, leading to its activation. Characterization of these proteins and their molecular interactions is critical for understanding CDK2/Cyclin A biology as well as for the development of chemical probes to inhibit aberrant regulation of this complex. Here we show that CDC25B is rigid in solution and its structure closely matches that found in the crystal structure. In addition, we have characterized the CDC25B-CDK2/Cyclin A interaction using a variety of biophysical techniques and found that CDC25B makes multiple contacts with CDK2/Cyclin A. Finally, we determined the binding mode between CDK2/Cyclin A and the activator Mre11, finding that the interaction is mediated by two motifs on the Mre11 C-terminus and interacts with CDK2/Cyclin A at least in part through contacts to the RxL peptide binding pocket on Cyclin A. These results lead to new understandings of how CDK2/Cyclin A is regulated and has implications for the development of chemical probes and potential therapeutics targeting its activation.

2.2 Introduction

As discussed in Chapter 1, the CDC25 dual-specificity phosphatases are key regulators of the cell cycle. Their oncogenic role in cancer has led to their active targeting for small molecule inhibitor development[1–4]. Because of their potential as therapeutic targets in cancer, studies of CDC25 family catalytic mechanism and structure are of vital importance.

Previous molecular dynamics simulations combined with bioinformatics analysis have suggested that approximately 20 C-terminal residues of CDC25B are partially unfolded or disordered in solution[5,6]. It has been hypothesized that dynamics of the C-terminus allows for the formation of transient pockets near the active site[5,6]. If confirmed, these results would have important implications for the development of any CDC25B inhibitors through structure-based drug design[6]. Therefore, the need for experimental characterization of the dynamics of CDC25B has been emphasized in the literature[6].

The most well studied biological role for CDC25B is the dephosphorylation of the CDK2/ Cyclin A[7–10]. A variety of experiments addressing this interaction using biochemical and enzymatic methods resulted in an understanding of how CDC25B catalyzes the dephosphorylation reaction[8], and has provided insight on the interaction mechanism through mutagenesis and computational modeling[7,9,10]. However, direct biophysical characterization of the interaction in solution has not been done. Understanding this interaction is critical for the development of small molecule inhibitors targeting the protein-protein interaction. For this reason, we assessed the CDC25B-CDK2/Cyclin A interaction in a variety of biophysical experiments.

In addition to its interaction with CDC25B, the CDK2/Cyclin A complex has several other binding partners that regulate its activity. One such recently identified binding partners is

the DNA damage response protein Mre11[11]. Mre11 plays a critical role in DNA double strand break repair, canonically through its role in the MRN complex (Mre11, Rad50, and NBS1)[12]. The MRN complex is involved with both the homologous recombination[13] and the non-homologous end joining[14] mechanisms of double strand break repair through its interaction with the ends of DNA double strand breaks[15], its end resection at breaks[16], as well as its recruitment and activation of ATM to initiate DNA damage signaling[17]. An MRN-independent role for Mre11 has emerged in cell cycle regulation through activation of CDK2/Cyclin A. Recent studies by Buis et al. have demonstrated that a direct interaction between Mre11 and the CDK2/Cyclin A complex links cell cycle regulation and DNA double strand break repair machinery to restrict the use of homologous recombination S and G2 phases[11]. They determined the interaction between Mre11 and CDK2/Cyclin A regulates the phosphorylation state and protein levels of CtIP, a critical protein involved in the homologous recombination pathway of DNA double strand break repair[18]. The phosphorylation state of CtIP was found to be dependent on the kinase activity of CDK2. Increased phosphorylation of CtIP resulted in higher CtIP protein levels through a reduction in proteasome-mediated degradation. Buis and colleagues also determined through yeast two hybrid experiments that Mre11 interacts directly with the CDK2/Cyclin A complex, with a minimal interaction motif in the very C-terminal region of Mre11. Beyond this, little is known about the mechanism of the Mre11-CDK2/Cyclin A interaction. To better understand the mechanism of this interaction, we studied the Mre11-CDK2/Cyclin A interaction in vitro.

2.3 Dynamics of the CDC25B catalytic domain in solution

In order to probe the backbone dynamics of the catalytic domain of CDC25B by NMR, we assigned the CDC25B backbone using triple resonance experiments. Our initial studies indicated that CDC25B was well folded, due to the good peak dispersion on the $^1H^{15}N$-HSQC spectrum. However, we observed that the wild-type protein was unstable in solution over longer periods of time, leading to reduced quality of the NMR spectra. We found that a point mutation of the active site cysteine to serine (C473S) drastically improved the long-term protein stability, most likely due to reducing protein oxidation at this residue. In order to ensure that this mutation did not affect the structure or backbone dynamics of CDC25B, we measured the $^1H^{15}N$-HSQC spectra (Appendix Figure 2.A1) and the backbone ^{15}N T1, T2 relaxation times (Appendix Figure 2.A2) for both the mutant and the wild-type proteins. These experiments indicate that the wild type and C473S mutant proteins have nearly identical structures and backbone flexibility in solution. Moreover, it has been previously shown that the structure of C473S mutant is identical to the wild type protein[10]. Due to the increased long-term stability of the CDC25B C473S mutant, we selected this variant for characterization using solution NMR.

The ^1H-^{15}N HSQC spectrum for the CDC25B C473S protein contains 155 resonances peaks, which constitutes 83 % of the expected resonances for all of the backbone amides present in the sequence. Of these, we were able to assign 92 % of the observed backbone amide resonances using triple resonance NMR experiments (Figure 2.1). The unobserved amide resonances correspond primarily to several N-terminal residues as well as residues located in two loop regions, corresponding to residues 461-467, and 495-504. These regions most likely are unobserved due to motions of these residues and rapid exchange of the amide protons with water, leading to peak broadening. This is in agreement with data from the published crystal structure

31
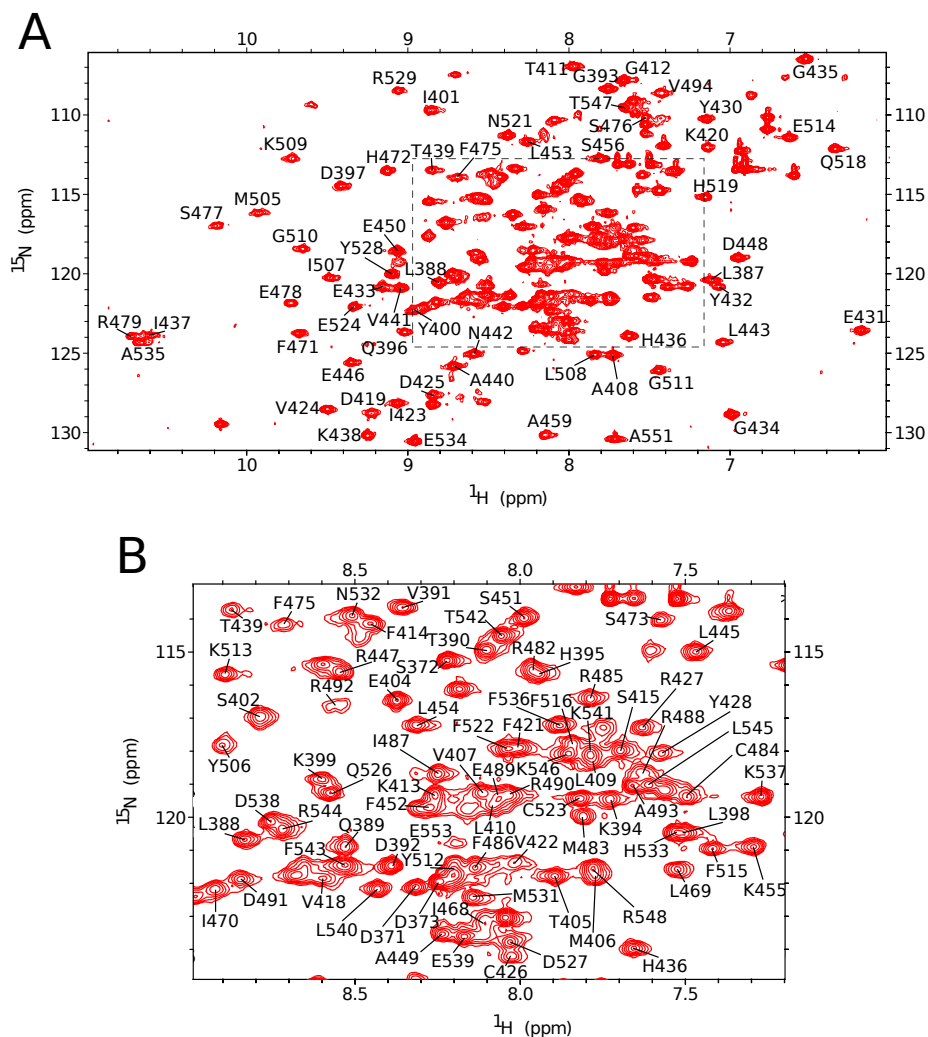
Figure 2.1. *Assignment of CDC25B catalytic domain.* A) The $^1H^{15}N$-HSQC spectrum of the CDC25B catalytic domain is shown with assignments labeled. Cutout of the overlapped region denoted by the dotted box shown below. B) Cutout of the overlapped region of the spectrum with assignments.

of CDC25B, which has no electron density for the N-terminal residues unobserved by NMR and high B-factors for those residues in the 495-504 loop region, indicating a lack of structure for this region[10].

To explore the protein backbone dynamics of the CDC25B C473S on the pico-second to nano-second timescale, we measured the R_1 and R_2 relaxation rates as well as the steady state ^1H-^{15}N heteronuclear NOE for the backbone amides using previously described methodology[19].

These experiments measure the loss of peak intensity at several different time intervals, and the extent of this loss in peak intensity is indicative of backbone motion on the ps-ns timescale. We then used Lipari-Szabo model-free analysis[20] to assess these fast time-scale backbone motions of CDC25B C473S. This analysis determined the global correlation time, a measure of the rate of protein tumbling in solution, to be 11.4 μs. This correlation time is consistent with that expected for a globular, monomeric protein of similar molecular weight to CDC25B. Additionally, the model-free analysis approach produces a measure termed the order parameter (S^2) that quantitatively represents the overall order of a given amide in solution. The values of the of the order parameter range from 0, corresponding to completely unrestricted motion of the amide, to 1, which corresponds to an amide with no motion. This analysis yielded an average order parameter of 0.94 across all the measured amides, which is indicative of a well ordered
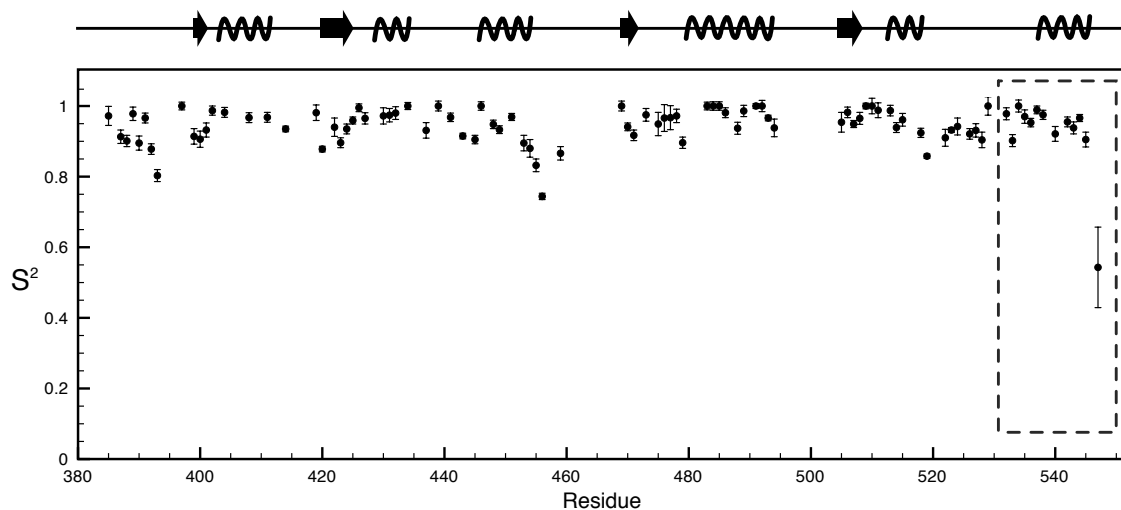
Figure 2.2. *The CDC25B catalytic domain is rigid in solution on the ps-ns timescale.* The generalized order parameter (S^2) is shown for the entire sequence as determined by model free analysis, with a box around C-terminal helix denoting the helix previously reported to be dynamic. A schematic of CDC25B secondary structure is shown above.

backbone with limited internal dynamic motion on the ps-ns timescale (Figure 2.2). Such a relatively high average order parameter may result from a lack of peaks for several amides in loop regions, again likely due to their fast exchange with water.

Only a few resonances show order parameters of less than 0.85, and these are exclusively found either at one of the CDC25 termini, or within the internal loop region 461-467. None of the observed amides experience an S^2 of less than 0.7, indicating that no region of the assigned protein, including the C-terminal helix, experiences any significant dynamics on this timescale. The model-free analysis also indicates that several residues experience additional exchange processes in the micro-second to milli-second timescale which contribute to the observed relaxation data (Figure 2.3). With the exception of E450 and R488, the remaining residues modeled with R_{ex} contributions appear immediately adjacent to or within loop regions, and all of the residues are further than 10 Å from the active site. To ensure the dynamics of CDC25B was
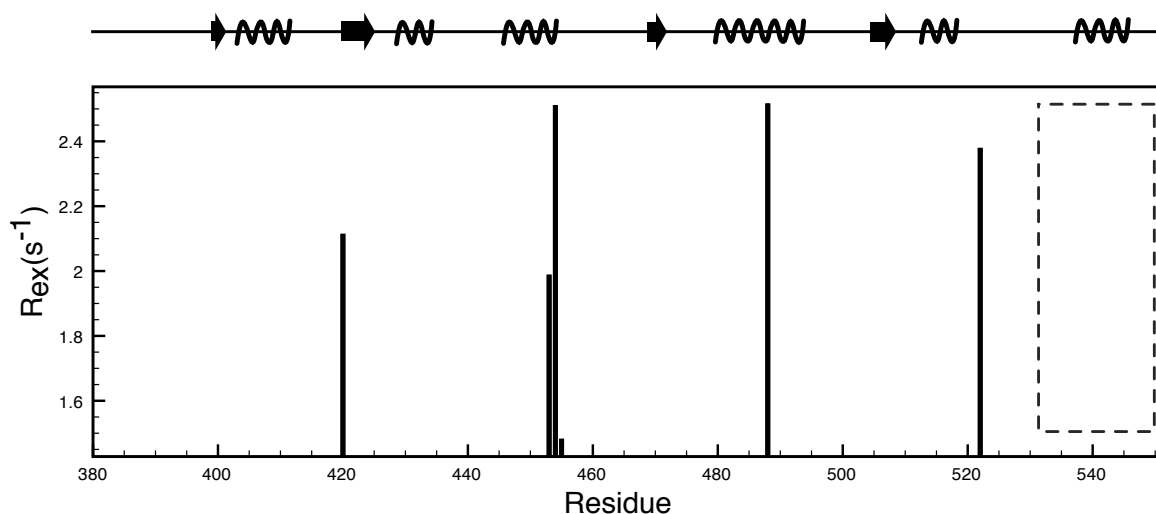
Figure 2.3. *The CDC25B catalytic domain is rigid in solution on the ms timescale as calculated by model-free analysis.* Additional exchange processes (R_{ex}) on the millisecond timescale as predicted by model free analysis. A box around the C-terminal helix is shown.

not altered by the C473S mutation, we measured both R_1 and R_2 relaxation rates for the wild type protein (Appendix Figure 2.A2). Data obtained from these experiments are highly consistent with the data recorded for the mutant, showing an average deviation of 0.048 s^{-1} and 1.57 s^{-1} for R_1 and R_2 respectively.

To examine closer the possibility of conformational exchange within the CDC25B C473S mutant catalytic domain on slower, μs-ms time scales, we carried out ^{15}N relaxation dispersion measurements using Carr–Purcell–Meiboom–Gill (CPMG) experiments[21]. These experiments revealed that only a few residues experienced significant exchange on the μs-ms time scale (Figure 2.4). Similar to the relaxation data acquired for shorter time scales, the majority of these backbone amides experiencing dynamics were found within or adjacent to loop regions (Figure 2.4). Several residues form small clusters, for example L388-Q389-T390 or D419-K420-
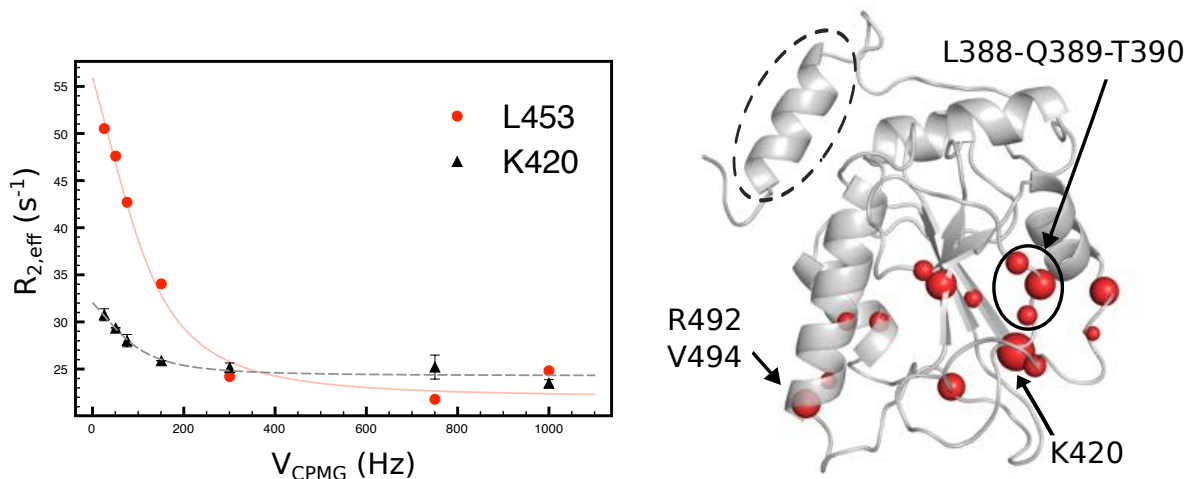
Figure 2.4. *The CDC25B catalytic domain is rigid in solution on the ms timescale experimentally.* Left: representative relaxation dispersion plots for K420 and L453 with $R_{2,eff}$ shown as a function of CPMG pulse frequency in Hz. Right: crystal structure of CDC25B (PDB: 2A2K[24]) highlighting residues experiencing exchange in the relaxation dispersion experiments. Size of sphere indicates relative magnitude of R_{ex} calculated by relaxation dispersion curve modeling. The C-terminal helix is denoted by the dashed ellipse.

V422 that have relatively similar exchange rates, representing correlated local motion of these groups in the milli-second timescale. Importantly, no motion on μs-ms time scale was observed for any residues within 10 Å of the active site or within the C-terminal helix.

Previous molecular dynamics simulations indicated that the CDC25B C-terminal residues (amino acids 531-550) are partially unfolded or disordered[5,6]. To the contrary, our experimental studies of the backbone dynamics clearly demonstrate that these residues are well ordered on ps-ns timescales, with an average S^2 of greater than 0.9 for residues in this region. Additionally, a lack of any correlated exchange in this region on longer time scales in the μs-ms range indicates that this helix does not undergo any partial unfolding.

2.4 Validation of the CDC25B crystal structure in solution

In order to determine whether the crystal structure of CDC25B correctly reflects the protein conformation in solution or whether the crystal structure is distorted by crystal packing, we
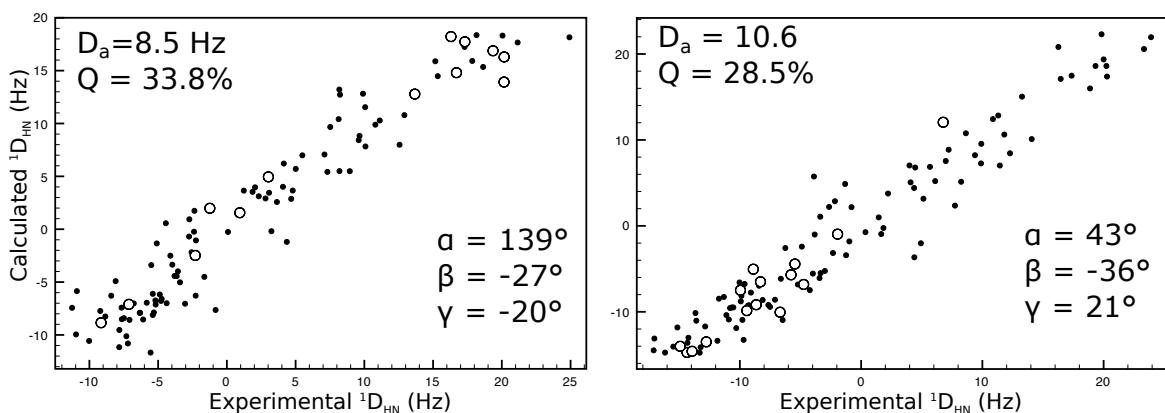
Figure 2.5. *Residual dipolar couplings indicate that CDC25B crystal structure is representative of its structure in solution.* Correlation of predicted and experimental residual dipolar couplings. Alignment tensor, Q-factor, and Euler angles are given. Closed circles represent the CDC25B catalytic domain sequence from 385 to 530, open circles represent the C-terminal helix from 531 to 551. Left: correlations for positively charged gel sample (50+M). Right: correlations for negatively charged gel sample (50-S).

measured residual dipolar couplings (RDCs). RDC measurements provide information on the orientation of bond vectors relative to a molecular frame of alignment, and thus have been shown to provide reliable data for comparative analysis between a crystal structure and the structure in solution[22,23]. Specifically, comparing calculated and experimental RDC values is a powerful tool in validating the crystal structure[22]. In order to measure RDC values, the protein must be weakly aligned with respect to the overall magnetic field to avoid rotational averaging of the RDCs. To this end we aligned the protein using both positively and negatively charged polyacrylamide gels as described previously[24]. We determined approximately 110 $^1D_{HN}$ RDCs measurements for each alignment (Figure 2.5). Comparison between the experimental RDC values and values calculated for the published CDC25B C473S catalytic domain crystal structure (PDB: 2A2K[25]) yields a very good agreement, with correlation coefficients of 0.96 and 0.97 for the protein in positively and negatively charged alignment media respectively (Figure 2.5). Importantly, RDCs for both the C-terminal helix and the active site agree very well with the RDC values predicted for the crystal structure. For example, the correlation coefficients for the RDCs for residues in the C-terminal
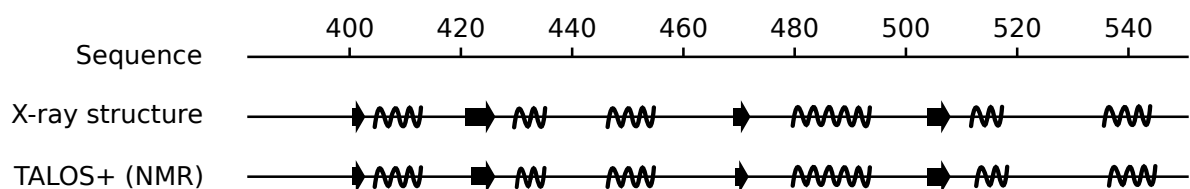
Figure 2.6. *Results of TALOS+ secondary structure prediction from the chemical shifts of the CDC25B C473S catalytic domain.* The program TALOS+ was employed to predict secondary structure elements from the experimentally determined chemical shifts of CDC25B. Results are shown with the sequence, predicted structural element, and a confidence value as output by the TALOS+ program.

helix are 0.95 and 0.91 in positively and negatively charged gels, respectively. These results from two independent alignments clearly indicate that the structure of CDC25B C473S in solution is very close to the structure determined by X-ray crystallography. To additionally examine the CDC25B C473S conformation in solution, we performed an analysis of the chemical shifts for all assigned resonances using the TALOS+ program[26], which predicts secondary structure elements from experimentally determined chemical shift data. The resulting secondary elements predicted from this analysis are in close agreement with those found in the crystal structure (Figure 2.6).

2.5 Biophysical characterization of the CDC25B-CDK2/CycA interaction in vitro

Once the we had explored the conformational dynamics and structure of CDC25B in solution, we turned to experiments characterizing the CDC25B-CDK2/Cyclin A interaction. We first measured the heat of binding by isothermal titration calorimetry ITC, from which the K_d and stoichiometry can be derived. Curve fitting of the heat of binding in our ITC experiments produced a K_d of 1.9 μM (Figure 2.7). As expected from previous studies[10], the stoichiometry of the complex was determined to be 1-to-1. In addition to ITC, we measured the K_d for the CDC25B-CDK2/Cyclin A interaction using biolayer interferometry. Global fitting analysis determined the binding kinetics of the CDC25B-CDK2/Cyclin A interaction to be $1.28 \times 10^4 \pm 1.84 \times 10^2$ $M^{-1}s^{-1}$ and $1.58 \times 10^{-2} \pm 1.08 \times 10^{-4}$ s^{-1} for k_{on} and k_{off} respectively. This yielded K_d of 1.2 ± 0.02 μM which agrees well with our ITC experiments.

To map the CDC25B-CDK2/Cyclin A binding interface in vitro, we employed NMR to analyze the CDC25B C473S backbone amide chemical shift perturbations in the presence of CDK2/Cyclin A. Initial experiments used the CDC25B catalytic domain containing it's
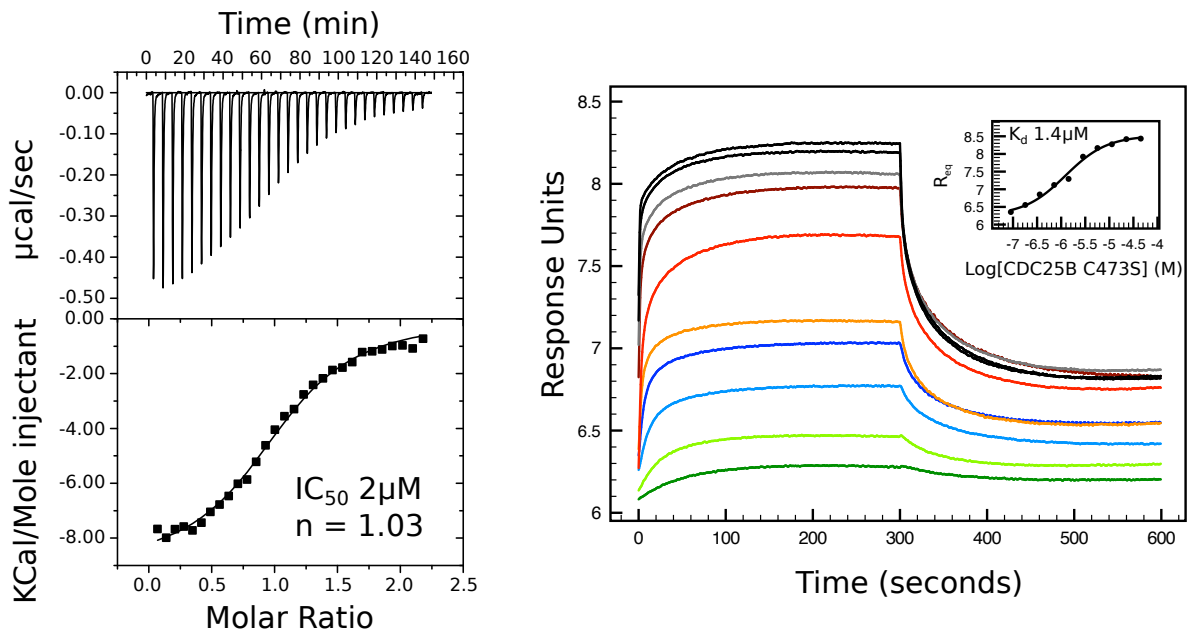
Figure 2.7. *Biophysical determination of the CDC25B-CDK2/Cyclin A binding affinity.* Left: ITC binding analysis of the CDC25B-CDK2/Cyclin A interaction. Right: biolayer interferometry association and dissociation curves. Colored curves correspond to CDC25B at various concentrations: black, 50 µM; dark gray, 25 µM; light gray, 12.5 µM; maroon, 6.25 µM; red, 3.125 µM; orange, 1.56 µM; blue, 0.78 µM; aqua, 0.39 µM; light green, 0.2 µM; dark green, 0.1 µM. Plot of R_{eq} versus CDC25B concentration is inlaid.

unstructured C-terminal tail, which has been shown to be one of the two key sites for high-affinity

binding to CDK2/Cyclin A[9]. However, due to complex formation with CDK2/Cyclin A, the

spectrum for CDC25B was completely broadened and therefore was unusable for analysis. To

circumvent this, we expressed a truncated CDC25B (372-551) that included only the CDC25B

catalytic domain without the unstructured C-terminal tail. The reduction in affinity due to this

truncation resulted in an observable $^1H^{15}N$-HSQC spectra for CDC25B, allowing for the analysis

of chemical shift perturbations due to CDK2/Cyclin A binding (Figure 2.8) This analysis

revealed that the binding interface on CDC25B extends across the entire face of the domain

between the enzymatic active site to the previously described protein-protein interaction
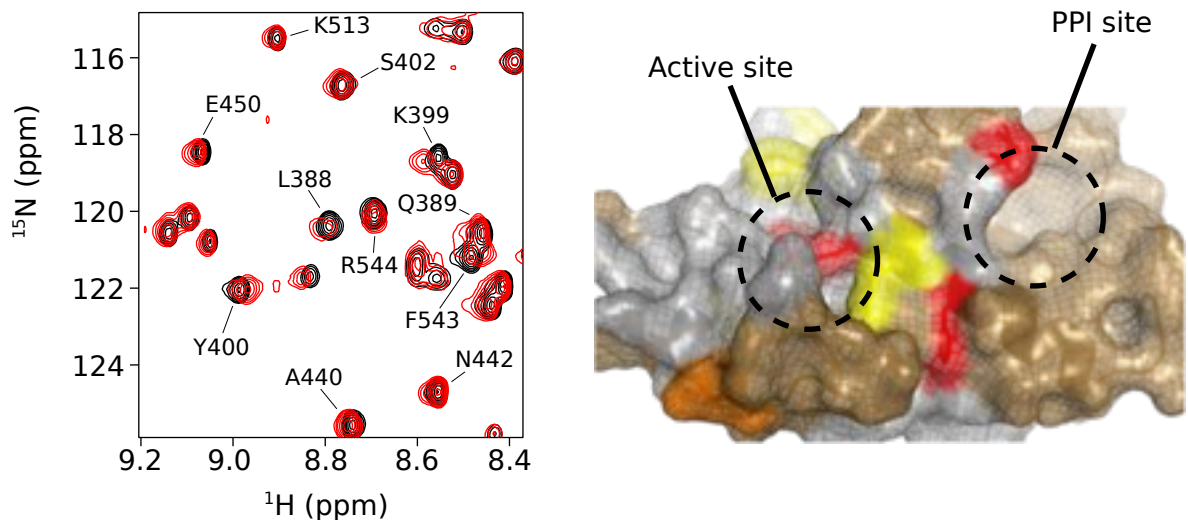
Figure 2.8. *CDK2/Cyclin A contacts the catalytic domain of CDC25B.* Left: chemical shift perturbations on a CDC25B (372-551) ^{1}H^{15}N-HSQC in the presence (red) and absence (black) of CDK2/Cyclin A. Right: global chemical shift perturbations mapped onto the CDC25B crystal structure (PDB: 2A2K[24]). Residues with amide chemical shift perturbations greater than 3 standard deviations are shown in red, greater than 2 standard deviations are shown in orange, greater than 1 standard deviation are in yellow. Unobserved or unassigned residues are shown in bronze, residues with observed amides without significant chemical shift perturbations are shown in gray.

"hotspot" residues[7]. (Figure 2.8). Despite the number of residues showing chemical shift perturbations due to CDK2/Cyclin A binding, many of the shifts are small and still more resonances remain unperturbed, and therefore it is highly unlikely that the CDC25B catalytic domain undergoes any major structural rearrangement upon binding to CDK2/Cyclin A.

In order to determine the region of the unstructured CDC25B C-terminal tail (552-566) involved in the interaction with CDK2/Cyclin A, we took advantage of carbon-detected NMR experiments. Observation of unfolded and unstructured proteins by amide-detected NMR is hindered by both a lack of resonance peak dispersion on the ^{1}H^{15}N-HSQC spectra as well as unfavorable exchange rates of the amide proton with water, which results in loss of resonances due to strong peak broadening. Previous studies have shown that carbon-detected NMR is a
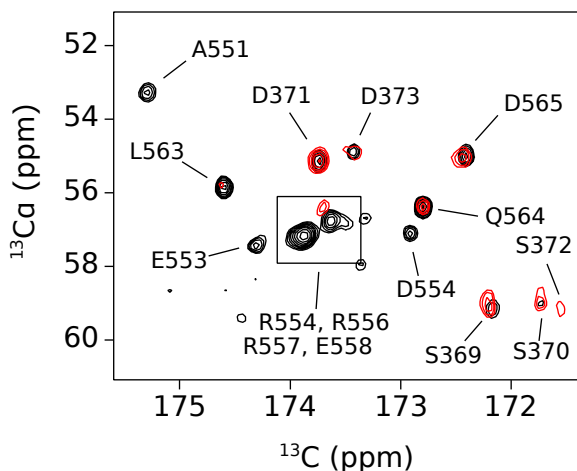
Figure 2.9. *Residues in the C-terminal tail of CDC25B interact with CDK2/Cyclin A*. CACO carbon-detected spectra for CDC25B containing the C-terminal unstructured region (552 – 566) in the presence (red) and absence (black) of CDK2/Cyclin A.

valuable tool to overcome these problems[27], owing to the fact that backbone carbons are not affected by amide exchange and a show greater chemical shift dispersion for random coil residues. For these reasons, we assigned backbone chemical shifts for the C-terminal tail of CDC25B in the presence and absence of CDK2/Cyclin A. For samples where CDK2/Cyclin A is present, a loss of several peaks was observed corresponding to the C-terminal residues 551 to 563 (Figure 2.9). This finding is in agreement with previous mutagenesis studies that found residues R556 and R562 in particular have a detrimental effect on the rate of catalysis for CDC25B toward phosphorylated CDK2/Cyclin A substrate[9]. These results demonstrate that CDC25B interacts with CDK2/Cyclin A through both the well-folded catalytic domain as well as the unstructured C-terminal tail (Figure 2.10).
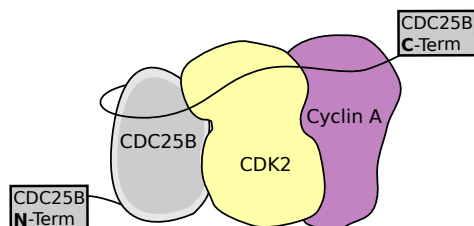
Figure 2.10. *The CDC25B-CDK2/Cyclin A interaction is mediated through multiple contacts*. A model of the CDC25B-CDK2/Cyclin A interaction showing the contacts between both the CDC25B catalytic domain and the C-terminal tail.

41

2.6 Characterization of the CDK2/CycA-Mre11 interaction in vitro

In addition to its interaction with CDC25B, the CDK2/Cyclin A has been shown to directly interact with the core DNA damage repair protein Mre11[11]. Previous reports have indicated that the C-terminal 76 residues of Mre11 (hereafter called Mre11^{C76}) are sufficient to maintain its interaction with the CDK2/Cyclin A complex[11]. To characterize this interaction we used the Mre11^{C76} protein fragment for NMR and ITC experiments. As predicted using bioinformatics analysis of this sequence, the Mre11^{C76} is unstructured in solution as demonstrated by the lack of resonance peak dispersion on the ^{1}H^{15}N-HSQC spectrum. To enable the mapping of the regions
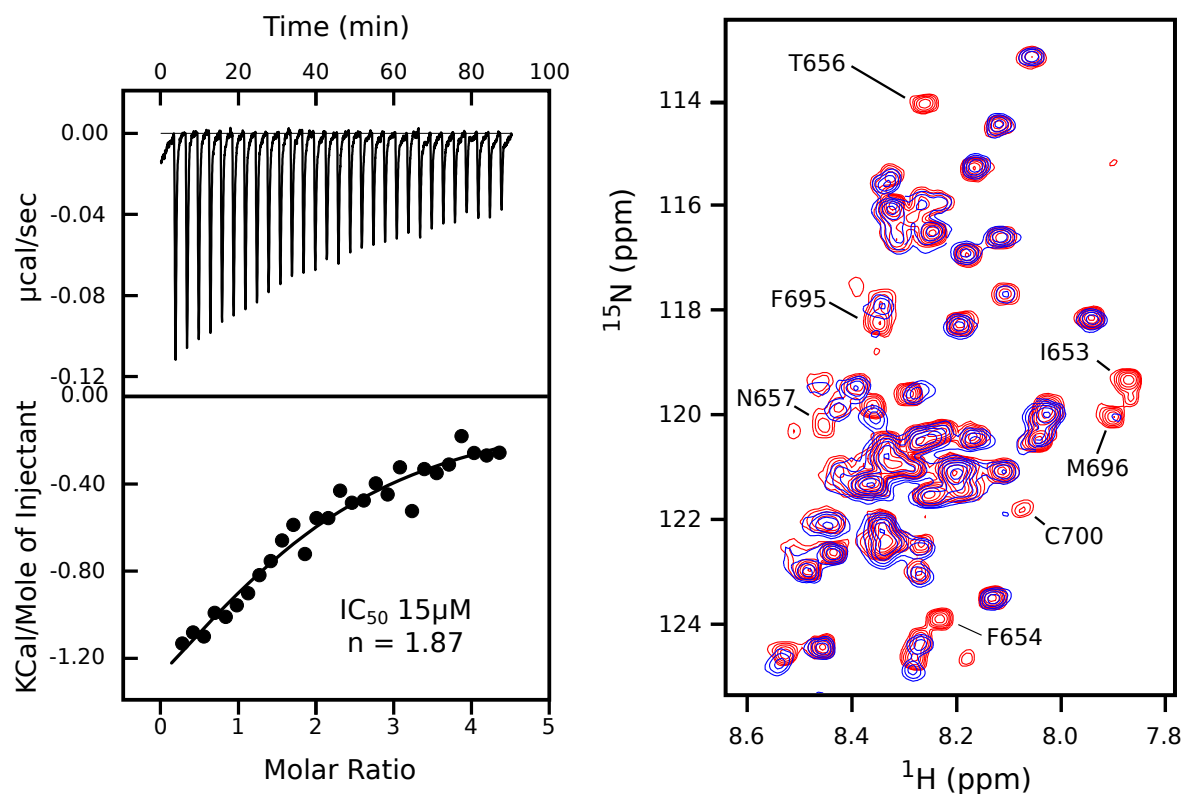
Figure 2.11. *Mre11^{C76} interacts directly with the CDK2/Cyclin A complex in vitro.* Left: ITC binding analysis of the CDK2/Cyclin A-Mre11^{C76} interaction. Right: A portion of the Mre11^{C76} ^{1}H^{15}N-HSQC spectrum in the presence (blue) or absence (red) of CDK2/Cyclin A. Several residues showing loss of peak intensity are labeled.

of Mre11^{C76} that interact with CDK2/Cyclin A, we assigned the backbone amide resonances for this protein fragment. Of the observed ^{1}H-^{15}N resonance peaks, 98% were unambiguously assigned to the corresponding amino acid, representing 83 % of the overall protein fragment (Appendix Figure 2.A3). The unobserved 17 % of amides likely undergo exchange with water on an unfavorable timescale for observation by NMR. For this reason, we measured backbone resonances for Mre11^{C76}. Because amide exchange does not affect backbone carbon resonances, the vast majority of these can be observed. Of all residues in the Mre11^{C76} protein fragment, we observed 94% of the ^{13}CO-^{13}Cα resonance peaks, and 94% of the those were unambiguously assigned to the corresponding amino acid (Appendix Figure 2.A4). The remaining 6 % of residues were unable to be assigned due to peak overlap in certain parts of the spectrum.

To characterize the Mre11 – CDK2/Cyclin A interaction, we employed ITC and NMR.
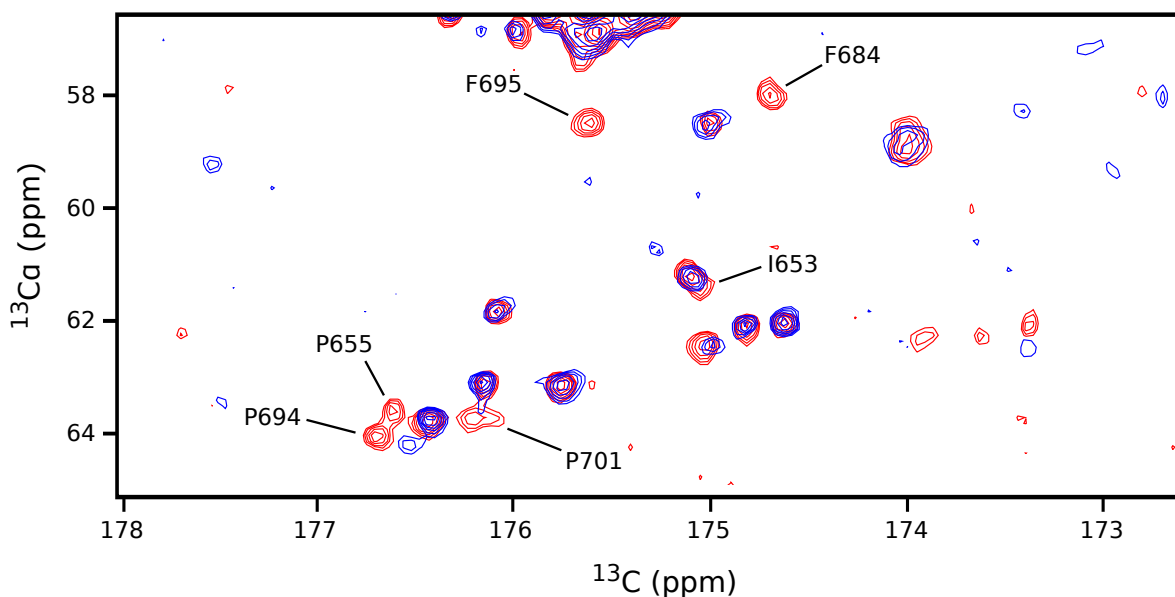
Figure 2.12. *Carbon-detected NMR experiments show the Mre11^{C76}-CDK2/Cyclin A interaction.* A portion of the Mre11^{C76} CACO spectrum in the presence (blue) or absence (red) of CDK2/Cyclin A. Several residues showing loss of peak intensity are labeled.

First we tested the affinity of the binding between Mre11^{C76} and the CDK/Cyclin A complex. Quantification of the binding affinity by isothermal titration calorimetry produced a K_d of 15 μM for the complex (Figure 2.11). Interestingly, the stoichiometry of the interaction as determined by ITC was 2:1 Mre11 to CDK2/Cyclin A. Mapping of the Mre11^{C76} residues that interact with the CDK2/Cyclin A complex was performed by collecting NMR spectra for ^{13}C ^{15}N-labeled Mre11^{C76} in the presence of CDK2/Cyclin A. Strong peak broadening was observed for Mre11^{C76} residues involved in the interaction with CDK2/CyclinA due to the slower molecular tumbling of the complex, while sharp resonance peaks were observed for the unrestricted regions of Mre11^{C76} (Figure 2.11, Figure 2.12). A combined analysis of the ^{1}H-^{15}N and ^{13}C-^{13}Cα peak broadening indicates that two distinct sequences are involved in the interaction with CDK2/Cyclin A (Figure 2.13). Both motif 1 (aa 654-658) and motif 2 (aa 684-701) contain a hydrophobic core preceded by a short acidic sequence. These results indicate that the Mre11 C-
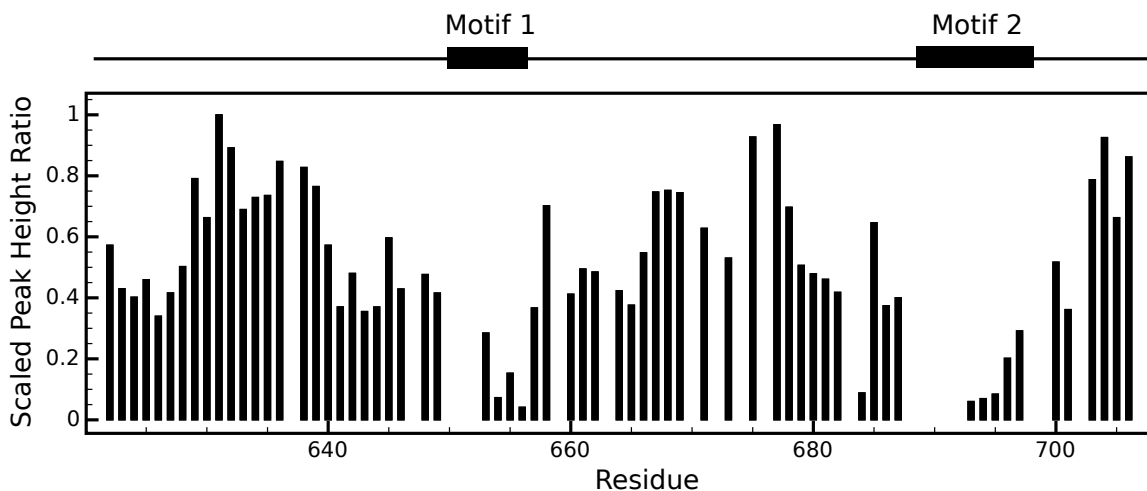
Figure 2.13. *Mre11^{C76} interacts with the CDK2/Cyclin A complex through two motifs.* Combined analysis of peak intensity for each residue derived from ^{1}H^{15}N-HSQC and ^{13}C-detected experiments.
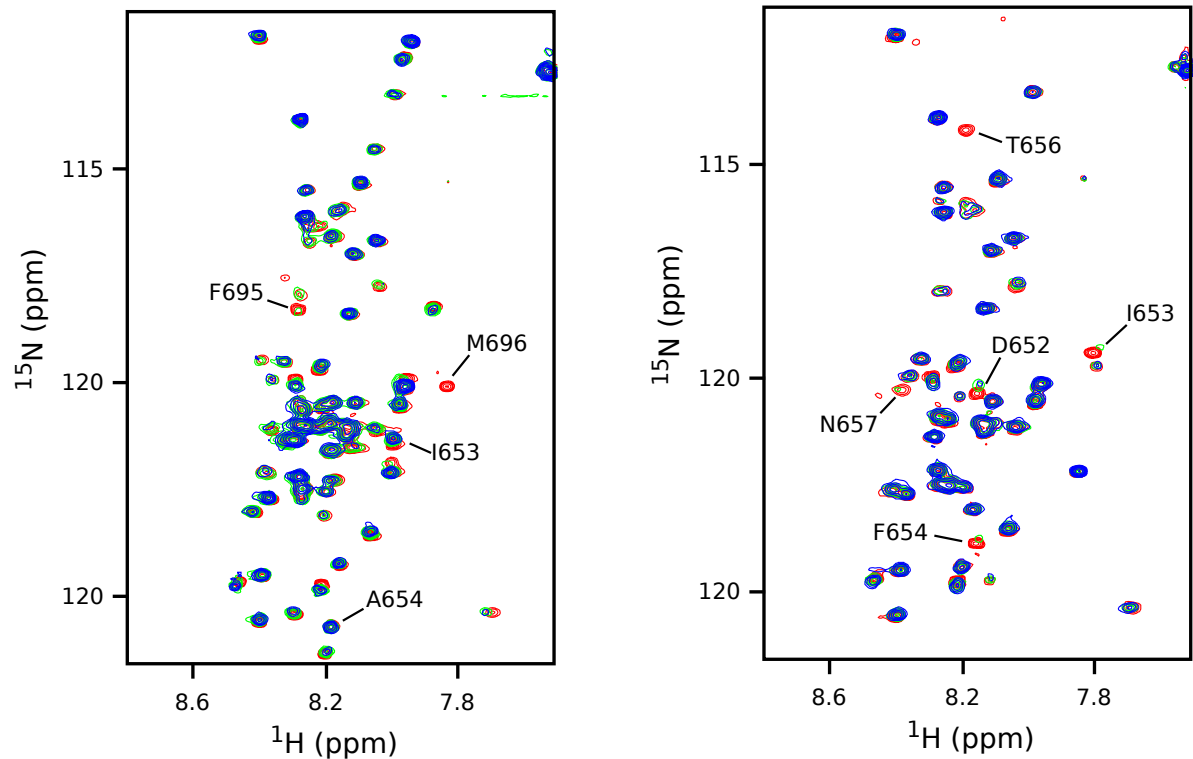
Figure 2.14. *Both motifs on Mre11^{C76} interact with CDK2/Cyclin A independently.* Left: ^{1}H^{15}N-HSQC spectrum of Mre11^{C76} F654A/P655A mutant in the presence (green at 1:1 molar equivalent, blue at 1:2) and absence (red) of CDK2/Cyclin A. Several residues showing loss of peak intensity are labeled. Right: ^{1}H^{15}N-HSQC spectrum for Mre11^{C76} truncated at residue 674 in the presence or absence of CDK2/Cyclin A. Colors are as described in A.

terminus interacts directly with the CDK2/Cyclin A complex in vitro and is mediated by two

motifs in the Mre11 C-terminus.

To understand how these two motifs mediate the Mre11-CDK2/Cyclin A interaction, we

introduced mutations into Mre11^{C76}. Upon mutation of two residues in the hydrophobic core of

the first motif to alanines (F654A, P655A), the interaction of this entire motif with CDK2/Cyclin

A is abolished, however the second motif remains bound (Figure 2.14). Conversely, truncation

of the protein at residue 674 prior to the second motif does not affect the interaction between the

first motif and CDK2/Cyclin A (Figure 2.14). Mre11^{C76} contains an SQSQ motif (residues
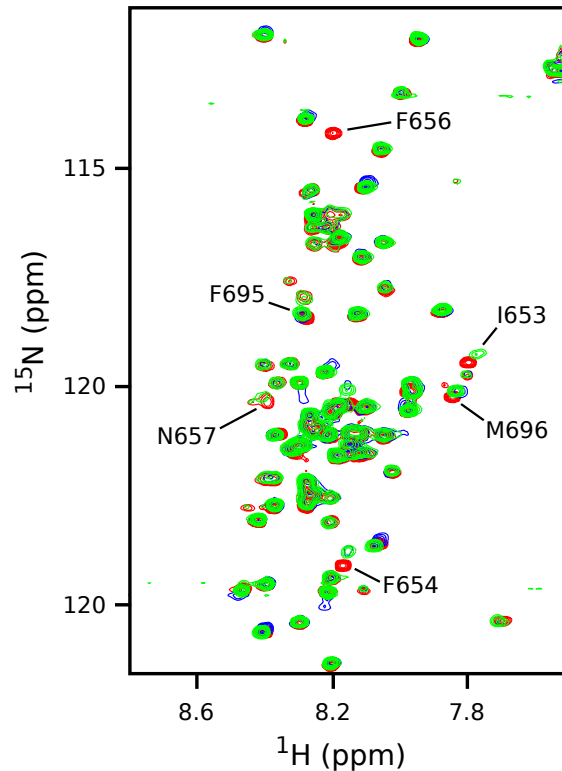
Figure 2.15. *Cyclin A RxL-binding site mutant has a weaker affinity for Mre11[C76]*. [1]H[15]N-HSQC spectrum for the Mre11[C76] wild-type in the absence (red) or presence of either CDK2/Cyclin A wild-type (blue) or the I213E mutation (green).

674-677) between the two CDK2/Cyclin A binding motifs; such SQ and TQ repeats have been shown previously to be potential phosphorylation sites for the DNA damage related kinases ATM and ATR[28], and therefore we wanted to probe the effect of phosphorylation at this site of Mre11[C76] on CDK2/Cyclin A binding in vitro. Mutation of the SQSQ motif to a phosphomemetic EQEQ does not affect the interaction of either motif (Appendix Figure 2.A4), indicating that phosphorylation at this site is unlikely to regulate the direct binding between Mre11[C76] and CDK2/Cyclin A.

To identify potential binding sites for Mre11[C76] on CDK2/Cyclin A we made the Cyclin A I213E mutant. This mutation affects a key residue in the so-called RxL binding site on Cyclin A, which has been shown previously to interact with a wide variety of peptides[29]. The [1]H[15]N-HSQC spectra of the Mre11[C76] peptide in the presence of CDK2/Cyclin A I213E mutant shows

significantly less broadening for many of the residues involved in both binding motifs, indicative of a weaker binding affinity for the mutant complex (Figure 2.14).

2.7 Discussion

In this study, we characterized the CDC25B catalytic domain in solution, determined the binding interfaces on CDC25B responsible for its interaction with CDK2/Cyclin A, and characterized the novel CDK2/Cyclin A interaction with Mre11. We found that the catalytic domain of CDC25B is relatively rigid in solution, and that the structure in solution is very close to the crystal structure. This finding is in contrast to previous molecular dynamics studies of this protein; specifically, that the 20 amino acids in the α-helix near the C-terminus in the crystal structure predicted to be dynamic in solution by molecular dynamics did not show any dynamics experimentally[5,6]. Experimental analysis of backbone dynamics on slow timescales shows no conformational exchange in either the C-terminal helix or anywhere near the active site, and therefore is highly unlikely to undergo any partial unfolding as previously suggested. Because we observed no backbone dynamics near the active site, it is unlikely that there are any transient or cryptic binding pockets near this site.

Our work has important implications for future structure-based small molecule design, since it provides strong evidence that the crystal structure of the CDC25B catalytic domain accurately reflects its conformation in solution. This study further demonstrates a need to experimentally validate findings from molecular dynamics simulations, particularly in cases where this may directly impact design of small molecule inhibitors.

Additionally, we have determined binding affinity of the CDC25B-CDK2/Cyclin A interaction by several methods, and characterized aspects of the protein-protein interaction by

47

NMR. Though a computational model of this interaction has been previously generated[25], these results are the first to directly observe the binding interface on the CDC25B catalytic domain or on its C-terminal tail. Our results show that the CDC25B catalytic domain does not undergo any major structural rearrangements upon binding to CDK2/Cyclin A, and that the residues after the C-terminal α-helix of the catalytic domain are unstructured and several of these residues contact the CDK2/Cyclin A complex.

Our characterization of the novel Mre11-CDK2/Cyclin A protein-protein interaction revealed that the interaction is mediated through two motifs on the Mre11 C-terminus. Previous experiments demonstrated that loss of even the final 13 residues of the Mre11 C-terminus significantly weakened its ability to bind CDK2/Cyclin A[11]. Our experiments provide a rationale for this observation; the majority of the second CDK2/Cyclin A binding motif is lost upon removal of these C-terminal residues, though the first binding motif remains and therefore Mre11 retains some binding affinity.

Correspondingly, we have demonstrated through mutagenesis that the Mre11 C-terminus interacts at least in part with the RxL-binding pocket on Cyclin A. Interestingly, mutation in the RxL-binding pocket disrupts the binding of both Mre11 motifs. Such a result indicates that both Mre11 motifs may interact with the same site on Cyclin A. The similar character of the sequences of the two motifs further helps rationalize this hypothesis; both contain several negatively charged aspartic or glutamic acid residues, followed by a pair of hydrophobic residues.

The Mre11-CDK2/Cyclin A interaction is not the first observation of a peptide-CDK2/Cyclin A interaction occurring through two motifs. Both CDK2/Cyclin A substrates and protein inhibitors have been shown to interact with the CDK2/Cyclin A complex through two critical motifs. For example, the CDK2/Cyclin A substrates p107, E2F1, and Rb all interact with both

the CDK2 active site as well as the RxL-binding site[30]. In addition to CDK2/Cyclin A substrates, inhibitors of this complex also bind through multiple motifs. An example is the CDK2 protein inhibitor p27[Kip1], which interacts with the CDK2/Cyclin A complex through both the RxL-binding site as well as a second regulatory site on the CDK2 N-terminal lobe[31,32]. Interestingly, approximately 40 residues separate these two binding sites, which is similar to the distance between the two interaction motifs in Mre11. These studies indicate that there are multiple sites on the CDK2/Cyclin A complex with a capacity for peptide binding. Our mutagenesis studies regarding the Mre11-CDK2/Cyclin A interaction indicate that Mre11 interacts at least in part with the Cyclin A RxL-binding pocket. However, given the number of peptide binding sites on CDK2/Cyclin A it is possible that the one of the two motifs on Mre11 interacts with a second site on CDK2/Cyclin A, but disruption of just the RxL-binding site is sufficient to disrupt the entire interaction.

2.8 Experimental Procedures

Expression and purification of the CDC25B catalytic domain

The CDC25B catalytic domain (372-551) and variants were expressed in *E. coli* BL21 (DE3) with an N-terminal GST tag. The CDC25B cDNA with an N-terminal TEV cleavage site was purchased from Genscript and cloned into a pGST-21a vector with NcoI/XhoI. Cells were grown to in either LB or labeled M9 medium. After 16 hr induction with 0.5 mM IPTG at 18 °C, *E. coil* cells were lysed by cell disruption in a buffer containing 50 mM Tris (pH 8.0), 150 mM NaCl, 1 mM TCEP, and 0.5 mM PMSF. The cell lysate was subjected to centrifugation, after which the soluble fraction was incubated with glutathione resin. The resin was then washed with lysis buffer, and eluted with lysis buffer containing 50 mM L-glutathione. The eluate was

proteolytically cleaved with TEV protease, followed by S-75 size exclusion chromatography in buffer containing 50 mM Tris (pH 8.0), 50 mM NaCl, and 1 mM TCEP. Pure fractions were pooled and frozen at -80 °C.

Expression and purification of CDK2/Cyclin A proteins

The CDK2/Cyclin A complex was expressed in *E. coli* BL21 (DE3) by co-expression of TEV cleavable N-terminally His tagged full-length human CDK2 in a pET24 vector, and residues 173-432 of human Cyclin A with an N-terminal His-Smt3 tag in a pET24 vector (generously gifted by Dr. Matthew Young, University of Michigan). The E. coil cells were lysed in a buffer containing 50 mM Tris (pH 8.0), 500 mM NaCl, 1 mM β-mercaptoethanol, and 0.5 mM PMSF after a 16 hr induction with 0.1 mM IPTG at 18 °C. After centrifugation, the soluble cell lysate was purified using Ni-affinity chromatography. The fractions containing 1:1 molar ratio CDK2/ Cyclin A complex were pooled and proteolytically cleaved with both TEV and ULP1 proteases, followed by S-75 gel filtration chromatography in buffer containing 50 mM Tris (pH 8.0), 150 mM NaCl, and 1 mM TCEP. Pure fractions were pooled and frozen at −80 °C.

Expression and purification of Mre11 proteins

Mre11^{C76} and variants were expressed in E. coli BL21 (DE3) as 3C protease-cleavable N-terminally His tagged peptides cloned into the pET32 vector. Cultures were induced with 0.1 mM IPTG at 18 °C overnight, and then lysed in a buffer containing 50 mM Tris (pH 7.5), 150 mM NaCl, 1 mM (TCEP), and 0.5 mM PMSF. The soluble cell lysate was purified using Ni-affinity chromatography. The eluted fractions were pooled and proteolytically cleaved with the rhinovirus 3C protease, followed by a second Ni-affinity chromatography step to separate the

cleaved protein from the tag. Pure fractions were pooled and frozen at –80 °C in buffer of 50 mM

sodium phosphate (pH 6.5), 50 mM NaCl, and 1 mM TCEP.

NMR spectroscopy and assignment of CDC25B catalytic domain

Samples for backbone assignment were made with [13]C[15]N-labeled CDC25B C473S (residues

372-551) prepared in a buffer containing 50 mM Tris (at either pH 7.0 or 8.0), 50 mM NaCl, 1

mM TCEP and 5 % D_2O. Spectra were acquired at 30 °C on a 600MHz Bruker Avance III

spectrometer equiped with cryoprobe, running Topspin version 2.1. Backbone assignment was

done using a series of triple-resonance experiments including HNCACB, CBCA(CO)NH,

HNCA, HN(CO)CA, HNCO, HN(CA)CO, and ^{15}N-separated NOESY-HSQC[33–35]. Processing

and spectral visualization was performed using NMRPipe[36] and Sparky[37].

NMR spectroscopy for CDC25B-CDK2/Cyclin A

For [1]H[15]N-HSQC experiments, uniformly ^{15}N labeled CDC25B (residues 372-551) at 40 μM was

mixed with unlabeled CDK2/Cyclin A complex at 80 μM in a buffer of 50mM Tris (pH 8.0)

50mM NaCl, 1mM TCEP and 5% D_2O at 25 °C. For ^{13}C-detected experiments, spectra for

samples containing 100 μM uniformly [13]C[15]N labeled CDC25B (residues 372-566) and 100 μM

unlabeled CDK2/Cyclin A were acquired in a buffer of 50mM Tris (pH 8.0) with 50mM NaCl,

1mM TCEP and 5% D_2O at 30 °C. All spectra were acquired on a 600MHz Bruker Avance III

spectrometer running Topspin version 2.1 and equipped with a TCI cryogenic probe. Processing

and spectral visualization was performed using NMRPipe[36] and Sparky[37].

NMR-based relaxation measurements

51

All relaxation measurements were acquired at 30 °C using ^{15}N-labeled CDC25B C473S or the wild type CDC25B in buffer containing 50 mM Tris (pH 7.0), 50 mM NaCl, 1 mM TCEP, and 5 % D_2O. T_1 and T_2 relaxation measurements, as well as the [1]H-^{15}N heteronuclear NOE measurement were obtained using experiments similar to those described by Bax et al.[19]. The relaxation delays for the T_1 and T_2 experiments were 10, 30, 70, 150, 330, 750, 1500, 2200ms, and 17, 34, 51, 68, 85, 102, 136, 170ms, respectively. [1]H-^{15}N heteronuclear NOE experiments were recorded as interleaved experiments with and without NOE saturation. Experimental relaxation delays were set at 6 seconds for T_2 and [1]H-^{15}N heteronuclear NOE measurements, and 4 seconds for T_1 measurements. T_2 and [1]H-^{15}N heteronuclear NOE experiments were performed in duplicate. T_1 and T_2 values were calculated by fitting relaxation curves in Sparky[37].

Relaxation dispersion experiments were recorded at 30 °C at 600MHz using a series of CPMG pulse trains as reported previously[21]. Two-dimensional spectra were acquired with CPMG field strengths of 25, 50, 75, 150, 300, 750, and 1000 Hz. Peak lists with intensities were used as input into the program NESSY for calculation of $R_{2,eff}$ and subsequent model fitting[17].

Model-free analysis

Model free analysis was performed using the modelfree4 and FASTModelfree programs[39,40]. The PDB structure used was prepared using the pdbinertia program[41], and the initial estimate for the diffusion tensor ($D_{par/per}$) was obtained using the r2r1_diffusion program[42]. An axially symmetric diffusion model was used with the following initial parameters: rotational correlation time τ_c = 11.4 μs, diffusion tensor $D_{par/per}$ = 1.25, and rotation angles θ = 6.3 °, Φ = -220 °, which describe the re-orientation of the molecule to the principal axis system. The protocol for model selection was as described by Mandel et al[43]. FASTModelfree was employed to iteratively adjust the global

parameters between optimizations of the internal parameters (S^2, τ_c, etc.). The global parameters converged after 8 iterations.

Measurement of residual dipolar couplings

Samples for measurement of residual dipolar couplings were made using ^{15}N CDC25B C473S in buffer containing 50 mM Tris (pH 7.0), 50 mM NaCl, 1 mM TCEP, with 5 % D_2O and acquired at 30 °C. Charged polyacrylamide gels for alignment were prepared as described previously[24]. Samples were prepared for isotropic measurements (gel-free) and two different anisotropic measurements, including a positively charged gel (50+M) and a negatively charged gel (50-S). $^1J_{NH}$ couplings were measured for isotropic and anisotropic using the IPAP experiment[44]. Residual dipolar couplings were calculated by subtracting the $^1J_{NH}$ couplings of the isotropic sample from the couplings for the anisotropic sample. Comparison of experimental and predicted RDC values was performed with the DC program in NMRPipe[36], using PDB code 2A2K[25] for the RDC back calculations.

Isothermal titration calorimetry

CDC25B C473S (residues 372-566) and CDK2/Cyclin A were extensively dialyzed at 4 °C against a buffer containing 50mM sodium phosphate (pH 7.0), 50mM NaCl, 1mM TCEP and degassed prior to the experiment. Experiments were performed using the VP-ITC system (MicroCal). CDC25B C473S at 100 μM was injected in 10 μL volumes into the calorimetric cell containing 10 μM CDK2/Cyclin A at 25 °C. Data was analyzed with Origin 7.0 (OriginLab).

Experiments for Mre11[C76] and CDK2/Cyclin A were performed as above with an alternate buffer of 50mM sodium phosphate (pH 6.5), 50mM NaCl, 1mM TCEP, and

concentrations of 200 μM Mre11^{C76} in the injectant and 10 μM CDK2/Cyclin A in the calorimetric cell at 25 °C.

Biolayer interferometry *for the CDC25B-CDK2/Cyclin A interaction*

CDK2/Cyclin A protein as previously described with the addition of a N-terminal Avi-tagged on CDK2 was co-purified with the biotin ligase BirA to produce biotinylated CDK2/Cyclin A. This protein was immobilized on a Super streptavidin sensor (ForteBio, Menlo Park, CA, USA) in a PBS buffer during a 600 second incubation at 25 °C. CDK2/Cyclin A immobilized sensors were then placed in a cell containing CDC25B C473S (residues 372-566) at various concentrations for 300 seconds, followed by a 300 second washout with PBS. Data was collected and analyzed using the Octet RED96 system and software.

NMR spectroscopy of the Mre11 C-terminal domain

NMR experiments for assignment were acquired for uniformly $^{13}C^{15}N$ labeled Mre11^{C76} at 140 μM in a buffer of 50mM Tris (pH 7.5) 50mM NaCl, 1mM TCEP and 5% D_2O at 25 °C. Spectra were acquired on a 600MHz Bruker Avance III spectrometer running Topspin version 2.1 and equipped with a TCI cryogenic probe. Backbone assignment was done using a series of triple-resonance experiments including HNCACB, CBCA(CO)NH, HNCA, HN(CO)CA, HNCO, and HN(CA)CO, as well as several ^{13}C-detected experiments including CACO, CBCACO, and CANCO. Samples for characterization of the Mre11^{C76}-CDK2/Cyclin A protein-protein interaction were acquired in a buffer of either 50mM Tris (pH 6.5) or 50mM phosphate buffer (pH 6.5), with 50mM NaCl, 1mM TCEP and 5% D_2O at 30 °C. The same conditions were used for all experiments with Mre11 mutant proteins. Processing and spectral visualization was

performed using NMRPipe[36] and Sparky[37].

Notes

Characterization of the CDC25B catalytic dynamics in solution has been published[45] by George Lund and Tomasz Cierpicki as "Solution NMR studies reveal no global flexibility in the catalytic domain of CDC25B" (2014) Proteins 82, 2889–95.

2.9 Appendices
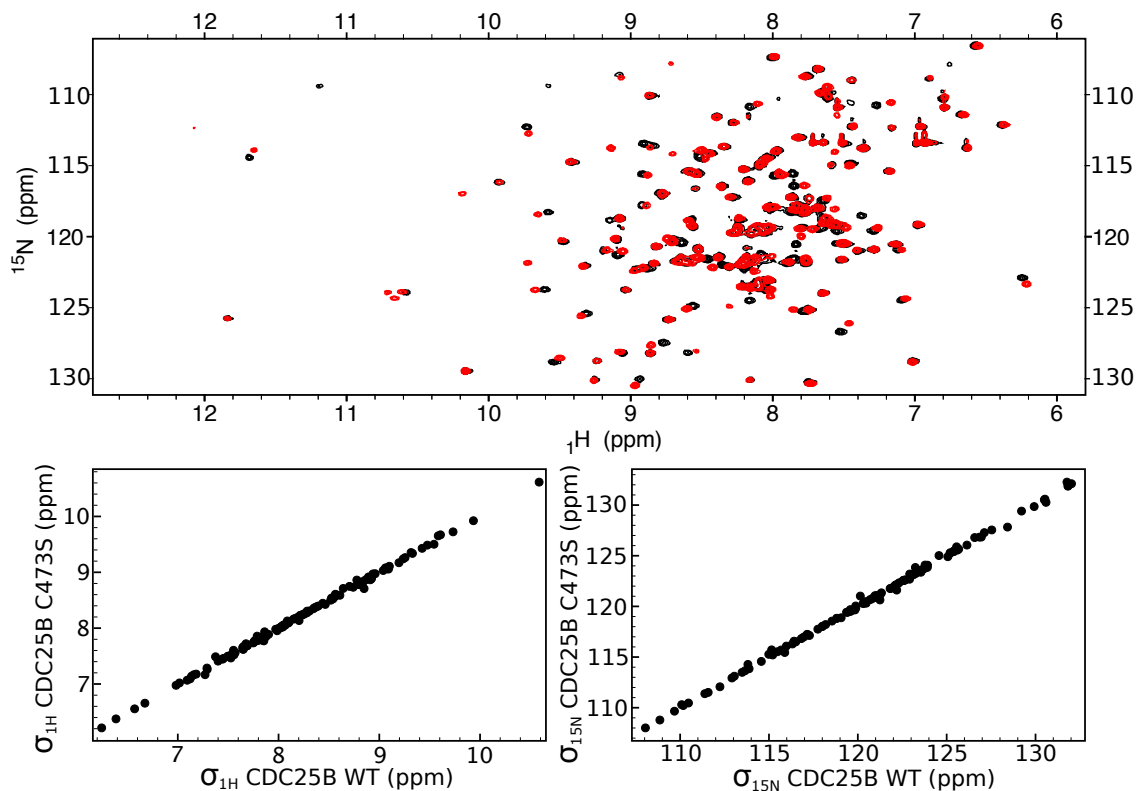
Appendix Figure 2.A1. *Comparison of chemical shifts between CDC25B WT and the C473S mutant.* A) Overlap of ^{1}H^{15}N-HSQC spectra for CDC25B WT (black) and C473S (red). B) Comparison of ^{1}H chemical shifts for the same residues in CDC25B WT and C473S mutant proteins from the ^{1}H^{15}N-HSQC spectra. C) Same as in B, comparing ^{15}N chemical shifts. Analyses B and C omit 6 residues from the mutant protein including and immediately adjacent to the mutated residue (residues H472, S473, S476, S477, E478, and R479) that differed significantly enough in chemical shift such that they could not be definitely assigned in the WT spectrum.
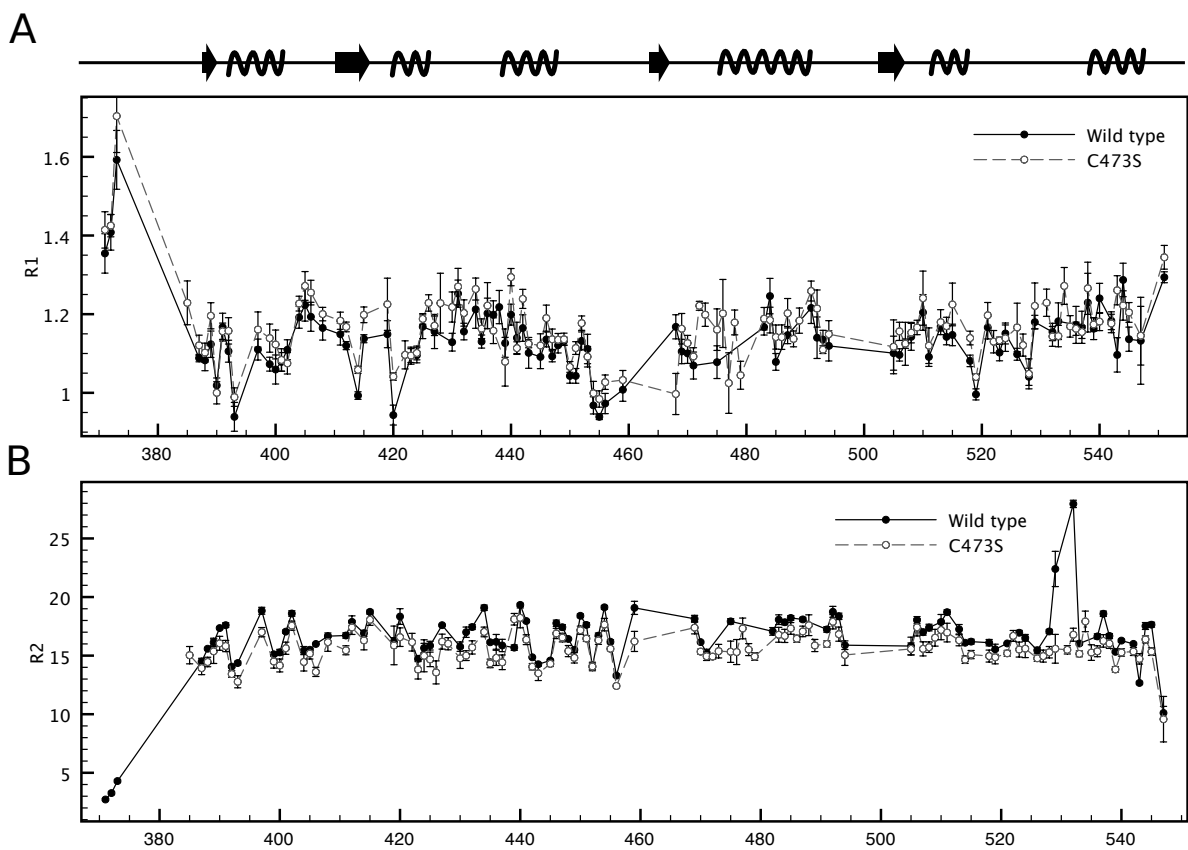
Appendix Figure 2.A2. *Comparison of relaxation measurements between CDC25B WT and the C473S mutant.* A) R_1 values for CDC25B WT (black dots, solid line) and the C473S mutant (white dots, dotted line). A schematic of CDC25B secondary structure is shown above. B) Same as in A, comparing R_2 values.
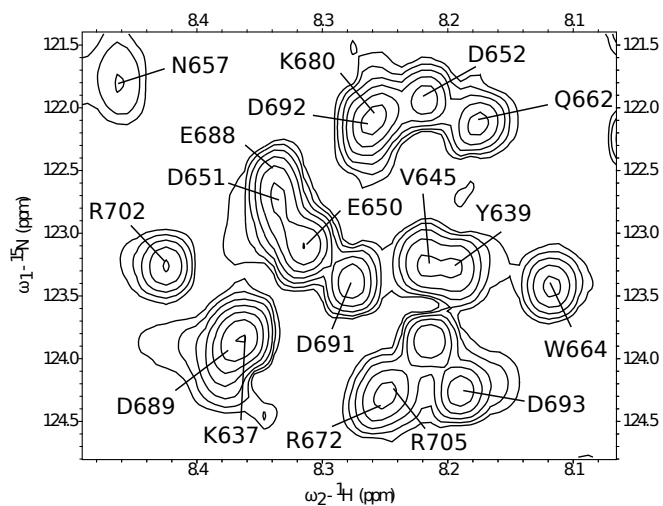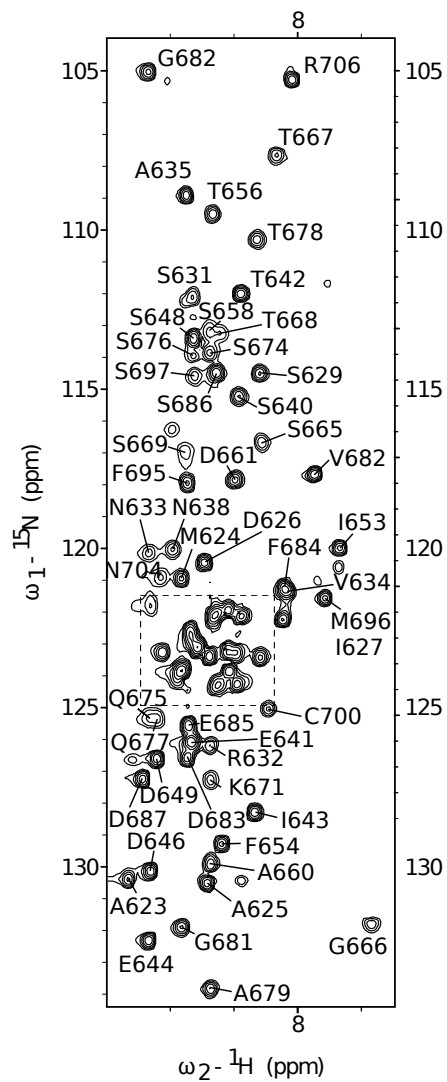
Appendix Figure 2.A3. *Assignment of Mre11 $^1H^{15}N$-HSQC spectrum.* Left: entire $^1H^{15}N$-HSQC spectrum is shown with assignment; right: zoomed in section of the $^1H^{15}N$-HSQC spectrum denoted by the dotted box on the left side.
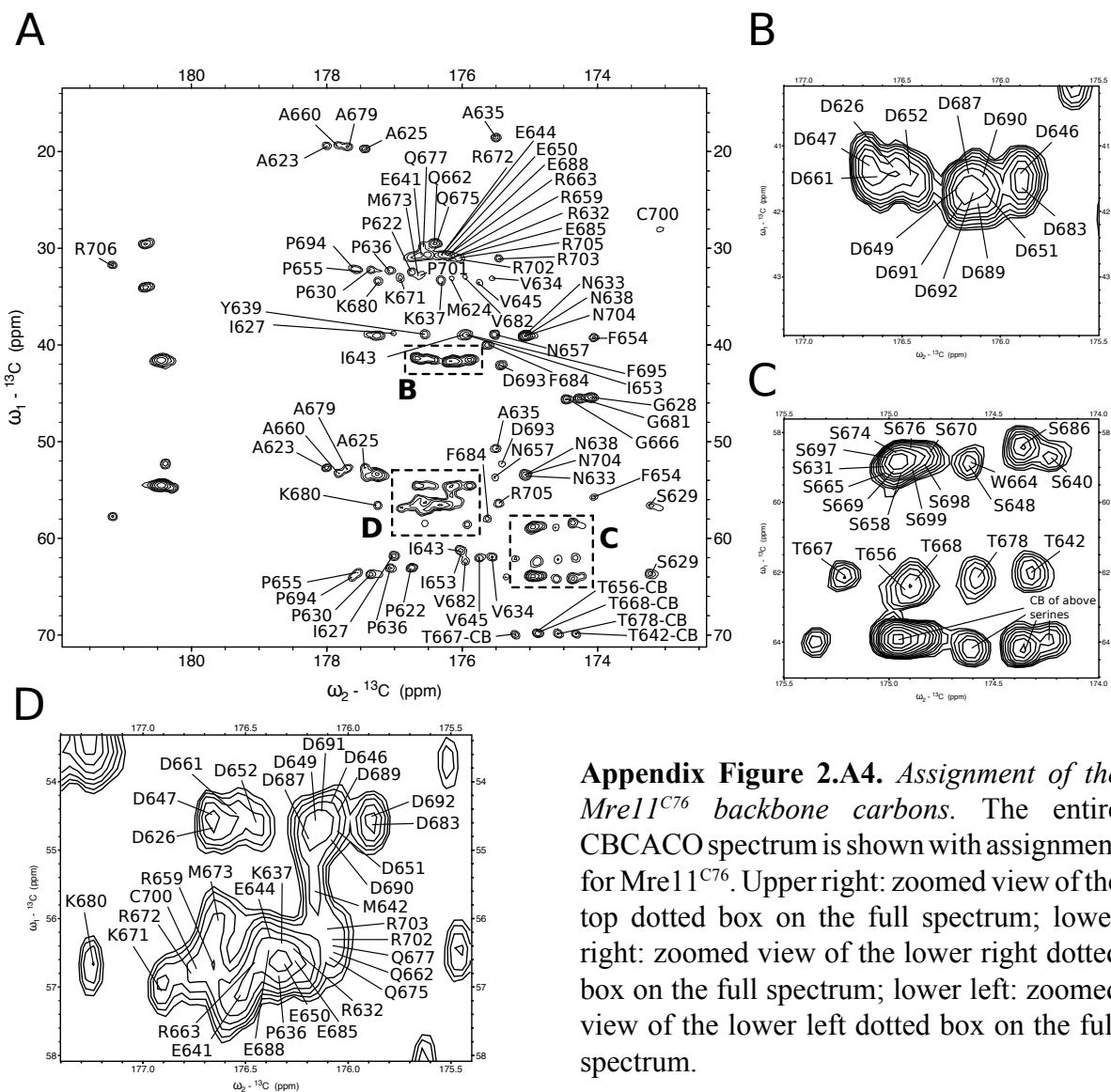
Appendix Figure 2.A4. *Assignment of the Mre11^{C76} backbone carbons.* The entire CBCACO spectrum is shown with assignment for Mre11^{C76}. Upper right: zoomed view of the top dotted box on the full spectrum; lower right: zoomed view of the lower right dotted box on the full spectrum; lower left: zoomed view of the lower left dotted box on the full spectrum.
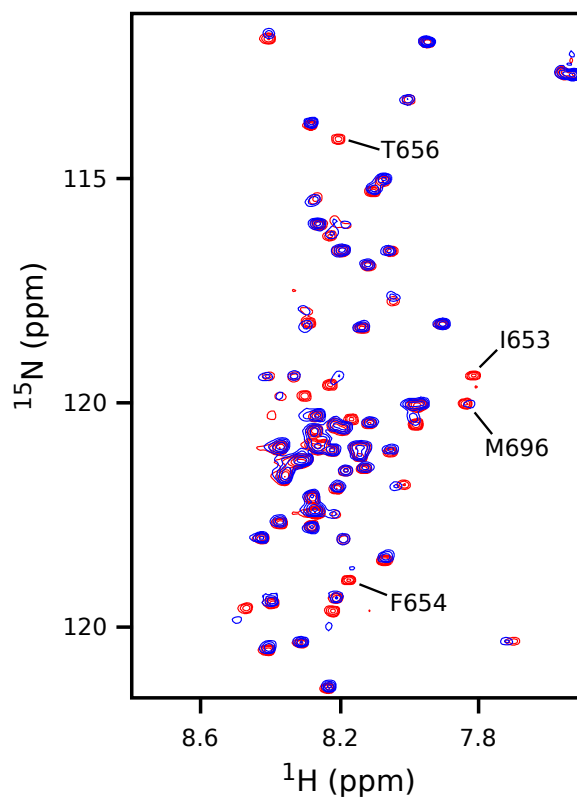
Appendix Figure 2.A5. *Phosphomemetic of ATM/ATR phosphorylation does not affect Mre11^{C76} binding to CDK2/Cyclin A.* ^{1}H^{15}N-HSQC spectrum for the Mre11^{C76} SQSQ -> EQEQ (674-677) mutant in the presence (blue) and absence (red) of CDK2/Cyclin A.

2.10 References

1. Boutros, R., Lobjois, V. & Ducommun, B. CDC25 phosphatases in cancer cells: key players? Good targets? *Nat. Rev. Cancer* **7,** 495–507 (2007).

2. Kristjánsdóttir, K. & Rudolph, J. Cdc25 phosphatases and cancer. *Chem. Biol.* **11,** 1043–1051 (2004).

3. Lavecchia, A., Di Giovanni, C. & Novellino, E. Inhibitors of Cdc25 phosphatases as anticancer agents: a patent review. *Expert Opin. Ther. Pat.* **20,** 405–25 (2010).

4. Lavecchia, A., Di Giovanni, C. & Novellino, E. CDC25 phosphatase inhibitors: an update. *Mini Rev. Med. Chem.* **12,** 62–73 (2012).

5. Mamonov, A. B., Bhatt, D., Cashman, D. J., Ding, Y. & Zuckerman, D. M. General library-based Monte Carlo technique enables equilibrium sampling of semi-atomistic protein models. *J. Phys. Chem. B* **113,** 10891–904 (2009).

6. Arantes, G. M. Flexibility and inhibitor binding in cdc25 phosphatases. *Proteins* **78,** 3017–3032 (2010).

7. Sohn, J. & Rudolph, J. The energetic network of hotspot residues between Cdc25B phosphatase and its protein substrate. *J. Mol. Biol.* **22,** 4109 (2008).

8. Chen, W., Wilborn, M. & Rudolph, J. Dual-specific Cdc25B phosphatase: in search of the catalytic acid. *Biochemistry* **39,** 10781–10789 (2000).

9. Wilborn, M., Free, S., Ban, A. & Rudolph, J. The C-terminal tail of the dual-specificity Cdc25B phosphatase mediates modular substrate recognition. *Biochemistry* **40,** 14200–14206 (2001).

10. Sohn, J., Buhrman, G. & Rudolph, J. Kinetic and structural studies of specific protein-protein interactions in substrate catalysis by Cdc25B phosphatase. *Biochemistry* **46,** 807–818 (2007).

11. Buis, J., Stoneham, T., Spehalski, E. & Ferguson, D. O. Mre11 regulates CtIP-dependent double-strand break repair by interaction with CDK2. *Nat. Struct. Mol. Biol.* **19,** 246–52 (2012).

12. Williams, G. J., Lees-Miller, S. P. & Tainer, J. A. Mre11-Rad50-Nbs1 conformations and the control of sensing, signaling, and effector responses at DNA double-strand breaks. *DNA Repair (Amst).* **9,** 1299–306 (2010).

13. San Filippo, J., Sung, P. & Klein, H. Mechanism of eukaryotic homologous recombination. *Annu. Rev. Biochem.* **77,** 229–57 (2008).

14. Dinkelmann, M. *et al.* Multiple functions of MRN in end-joining pathways during isotype class switching. *Nat. Struct. Mol. Biol.* **16,** 808–13 (2009).

15. Williams, R. S. *et al.* Mre11 dimers coordinate DNA end bridging and nuclease processing in double-strand-break repair. *Cell* **135,** 97–109 (2008).

16. Buis, J. *et al.* Mre11 nuclease activity has essential roles in DNA repair and genomic stability distinct from ATM activation. *Cell* **135,** 85–96 (2008).

17. Lee, J.-H. & Paull, T. T. Direct activation of the ATM protein kinase by the Mre11/Rad50/Nbs1 complex. *Science* **304,** 93–6 (2004).

18. You, Z. *et al.* CtIP links DNA double-strand break sensing to resection. *Mol. Cell* **36,** 954–69 (2009).

19. Barbato, G., Ikura, M., Kay, L. E., Pastor, R. W. & Bax, A. Backbone dynamics of calmodulin studied by 15N relaxation using inverse detected two-dimensional NMR spectroscopy: the central helix is flexible. *Biochemistry* **31,** 5269–78 (1992).

20. Lipari, G. & Szabo, A. Model-free approach to the interpretation of nuclear magnetic resonance relaxation in macromolecules. 1. Theory and range of validity. *J. Am. Chem. Soc.* **104,** 4546–4559 (1982).

21. Tollinger, M., Skrynnikov, N. R., Mulder, F. A., Forman-Kay, J. D. & Kay, L. E. Slow dynamics in folded and unfolded states of an SH3 domain. *J. Am. Chem. Soc.* **123,** 11341–52 (2001).

22. Bax, A. Weak alignment offers new NMR opportunities to study protein structure and dynamics. *Protein Sci.* **12,** 1–16 (2003).

23. Prestegard, J. H., al-Hashimi, H. M. & Tolman, J. R. NMR structures of biomolecules using field oriented media and residual dipolar couplings. *Q. Rev. Biophys.* **33,** 371–424 (2000).

24. Cierpicki, T. & Bushweller, J. H. Charged gels as orienting media for measurement of residual dipolar couplings in soluble and integral membrane proteins. *J. Am. Chem. Soc.* **126,** 16259–66 (2004).

25. Sohn, J., Parks, J. & Buhrman, G. Experimental validation of the docking orientation of Cdc25 with its Cdk2-CycA protein substrate. *Biochemistry* **44,** 16563–16573 (2005).

26. Shen, Y., Delaglio, F., Cornilescu, G. & Bax, A. TALOS+: a hybrid method for predicting protein backbone torsion angles from NMR chemical shifts. *J. Biomol. NMR* **44,** 213–23 (2009).

27. Gray, F. L. V, Murai, M. J., Grembecka, J. & Cierpicki, T. Detection of disordered regions in globular proteins using ^{13}C-detected NMR. *Protein Sci.* **21,** 1954–60 (2012).

28. Traven, A. & Heierhorst, J. SQ/TQ cluster domains: concentrated ATM/ATR kinase phosphorylation site regions in DNA-damage-response proteins. *Bioessays* **27,** 397–407 (2005).

29. Brown, N. R., Noble, M. E., Endicott, J. a & Johnson, L. N. The structural basis for specificity of substrate and recruitment peptides for cyclin-dependent kinases. *Nat. Cell Biol.* **1,** 438–443 (1999).

30. Schulman, B. A., Lindstrom, D. L. & Harlow, E. Substrate recruitment to cyclin-dependent kinase 2 by a multipurpose docking site on cyclin A. *Proc. Natl. Acad. Sci.* **95,** 10453–10458 (1998).

31. Russo, A. A., Jeffrey, P. D., Patten, A. K., Massagué, J. & Pavletich, N. P. Crystal

structure of the p27Kip1 cyclin-dependent-kinase inhibitor bound to the cyclin A-Cdk2 complex. *Nature* **382,** 325–31 (1996).

32. Vlach, J., Hennecke, S. & Amati, B. Phosphorylation-dependent degradation of the cyclin-dependent kinase inhibitor p27. *EMBO J.* **16,** 5334–5344 (1997).

33. Schleucher, J. *et al.* A general enhancement scheme in heteronuclear multidimensional NMR employing pulsed field gradients. *J. Biomol. NMR* **4,** 301–6 (1994).

34. Kay, L. E., Xu, G. Y. & Yamazaki, T. *Enhanced-Sensitivity Triple-Resonance Spectroscopy with Minimal H2O Saturation*. *J. Magn. Reson. Ser. A* **109,** (1994).

35. Muhandiram, D. R. & Kay, L. E. Gradient-Enhanced Triple-Resonance Three-Dimensional NMR Experiments with Improved Sensitivity. *J. Magn. Reson. Ser. B* **103,** 203–216 (1994).

36. Delaglio, F. *et al.* NMRPipe: a multidimensional spectral processing system based on UNIX pipes. *J. Biomol. NMR* **6,** 277–93 (1995).

37. Goddard, T. G. & Kneller, D. G. SPARKY 3.

38. Bieri, M. & Gooley, P. R. Automated NMR relaxation dispersion data analysis using NESSY. *BMC Bioinformatics* **12,** 421 (2011).

39. Palmer, A. G. Modelfree 4.2. at <http://cpmcnet.columbia.edu/dept/gsas/biochem/labs/palmer/software.html>

40. Cole, R. & Loria, J. P. FAST-Modelfree : A program for rapid automated analysis of solution NMR spin-relaxation data. 203–213 (2003).

41. Palmer, A. G. pdbinertia. at <http://www.palmer.hs.columbia.edu/software/diffusion.html>

42. Palmer, A. G. r2r1_diffusion.

43. Mandel, a M., Akke, M. & Palmer, a G. Backbone dynamics of Escherichia coli ribonuclease HI: correlations with structure and function in an active enzyme. *J. Mol. Biol.* **246,** 144–63 (1995).

44. Ottiger, M., Delaglio, F. & Bax, A. Measurement of J and dipolar couplings from simplified two-dimensional NMR spectra. *J. Magn. Reson.* **131,** 373–8 (1998).

45. Lund, G. & Cierpicki, T. Solution NMR studies reveal no global flexibility in the catalytic domain of CDC25B. *Proteins* **82,** 2889–95 (2014).

Chapter 3

Identification of inhibitors of the CDC25B-CDK2/Cyclin A interaction through fragment screening by NMR

3.1 Abstract

CDC25 phosphatases are key cell cycle regulators and represent very attractive but challenging targets for anti-cancer drug discovery. Here, we explored whether fragment-based screening represents a valid approach to identify inhibitors of CDC25B. This resulted in identification of 2-fluoro-4-hydroxybenzonitrile, which directly binds to the catalytic domain of CDC25B. Interestingly, NMR data and the crystal structure demonstrate that this compound binds to the pocket distant from the active site and adjacent to the protein-protein interaction interface with CDK2/Cyclin A substrate. Furthermore, we developed a more potent analog that disrupts CDC25B interaction with CDK2/Cyclin A and inhibits dephosphorylation of CDK2. Based on these studies, we provide a proof of concept that targeting CDC25 phosphatases by inhibiting their protein-protein interactions with CDK2/Cyclin A substrate represents a novel, viable opportunity to target this important class of enzymes.

3.2 Introduction

As described in Chapter 1, the CDC25 family of dual-specificity protein phosphatases plays a central role in cell cycle regulation by activating the cyclin-dependent kinases (CDKs) through the removal of inhibitory phosphorylations.[1] CDC25 family member CDC25B regulates the G_2/M phase transition by removing two inhibitory phosphate groups from the ATP binding loop of the CDK2 kinase.[2,3] CDC25B is often overexpressed in various cancers, leading to excessive CDK2/Cyclin A activation and aberrant cell cycle progression resulting in poor clinical outcomes.[4–7] Genetic studies have shown the vital role of CDC25B in cancer for tumor cells growth, supporting that CDC25B is an attractive therapeutic target for inhibition by small molecules.[8–10] Indeed, the CDC25 phosphatases have been actively pursued as cancer drug targets for over twenty years.[11,12] To date, all efforts to inhibit CDC25 phosphatases were focused on targeting the catalytic sites of these enzymes,[11,13] which are unusually small and shallow without well-defined binding pockets, making CDC25s somewhat recalcitrant to drug discovery efforts.[14] Furthermore, the presence of a highly reactive catalytic cysteine in the active sites of CDC25s hampers screening and drug design efforts due to covalent binding and irreversible inhibition by diverse classes of small molecules.[11] Indeed, majority of well-studied and the most potent inhibitors of CDC25s discovered to date, including quinone and Vitamin K3 derivatives, are known to covalently modify cysteines in CDC25s,[11,15] raising questions about their potential toxicity and limiting their therapeutic applications.[16] Furthermore, no biophysical or structural characterization of known CDC25 inhibitors has been reported to date, leaving the mechanism of their binding largely unknown.

3.3 NMR-based fragment screening identifies a ligand of CDC25B

To assess whether small molecule compounds binding to CDC25B can be identified, we employed fragment-based screening approach. An in-house library of fragment-like compounds consisting of approximately 1500 chemically diverse small molecules was screened by NMR spectroscopy through the observation of ^{1}H and ^{15}N chemical shift perturbations on ^{1}H-^{15}N HSQC NMR spectra for uniformly ^{15}N labeled CDC25B catalytic domain. Through this screen, we found 2-fluoro-4-hydroxybenzonitrile, (compound **1**), as the only compound that binds to CDC25B (Figure 3.1). To map the binding site of **1** on CDC25B we analyzed chemical shift perturbations using previously determined backbone assignment[17]. Interestingly, we found that **1** does not bind to the active site but rather perturbs a set of residues in a distal site on CDC25B.
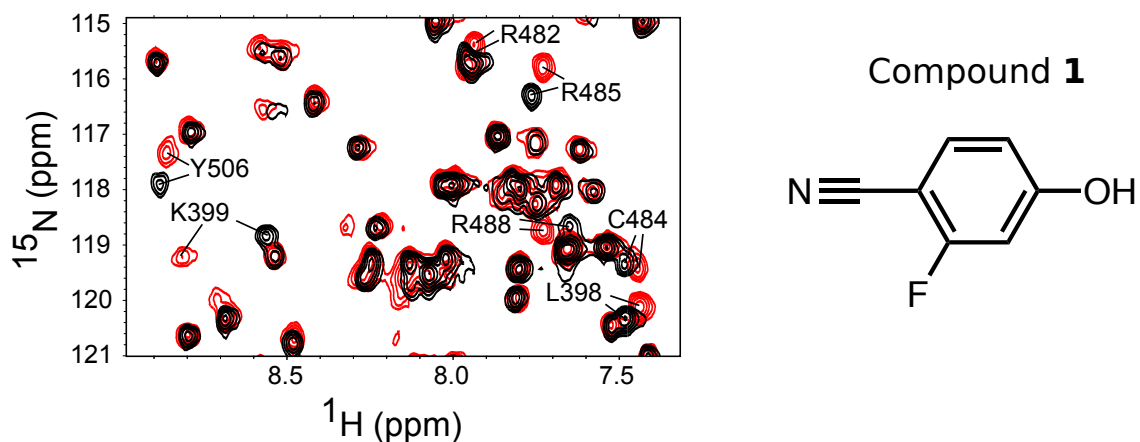
Figure 3.1. *Identification of compound **1** as a novel CDC25B ligand by fragment-based screening.* Left: a portion of the 1H-15N HSQC spectrum for the CDC25B catalytic domain in the presence (red) and absence (black) of 2mM **1**. Right: chemical structure of compound **1**.

3.4 Compound 1 binds a pocket on CDC25B adjacent to critical residues for the CDC25B-CDK2/Cyclin A protein-protein interaction

To accurately establish the binding mode of this compound we determined a high-resolution crystal structure of **1** bound to the CDC25B (Figure 3.2). The structure revealed that **1** binds to a relatively small but well-defined pocket on CDC25B located approximately 15Å away from the active site in agreement with the chemical shift perturbations. This binding pocket is primarily comprised of the Phe386, Leu398, Cys484, Arg488, and Met505 side chains. The phenyl ring of **1** inserts between the side chains of Leu398 and Arg488, forming a hydrophobic and cation-π interactions, respectively (Figure 3.2). The fluorine of **1** is present in two conformations, with one conformer pointing towards the backbone of Cys484 and the second pointing towards the solvent. The nitrile is partly solvent exposed, and the nitrile nitrogen replaces a well-defined
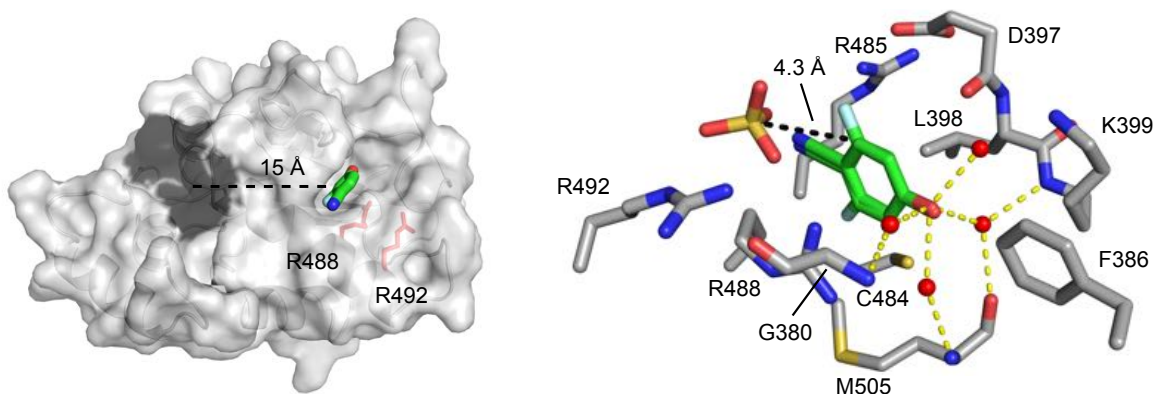
Figure 3.2. *Co-crystal structure of CDC25B bound to compound 1.* Left: crystal structure of **1** bound to CDC25B. Dark gray surface denotes the enzymatic active site. Two arginine residues involved in interaction with CDK2/Cyclin A substrate are labeled and shown in red. The distance between the catalytic cysteine and **1** is shown. Right: Molecular details of the interaction of **1** with CDC25B binding pocket. Distance between position 6 of **1** and the sulfate ion is given (PDB ID: 4WH7). The hydrogen bond network between the hydroxyl of **1** and four waters in the binding pocket is also shown.

water molecule found in the apo-structure near the backbone of Arg485. Interesting feature of this binding site is the presence of numerous well ordered water molecules which form a network of hydrogen bonds. These waters are hydrogen bonded to backbone carbonyl and amide of Met505 and amides of Lys399 and Gly380 (Figure 3.2). Binding of **1** replaces water molecule present in the structure of CDC25B and the hydroxyl group of **1** participates in a network of hydrogen bonds with remaining waters (Figure 3.2).

Interestingly, several residues directly adjacent to the binding site of **1** were shown previously to be involved in the protein-protein interaction between CDC25B and its substrate CDK2.[3,18] Based on mutagenesis studies, Arg488 and Arg492 in CDC25B (Figure 3.2) have been shown to be required for CDK2 substrate recruitment through ionic interactions with Asp206.[18] To further validate the importance of this site for interactions with CDK2/Cyclin A substrate, we introduced the R492L mutation. We assessed the ability of the R492L mutant and wild-type
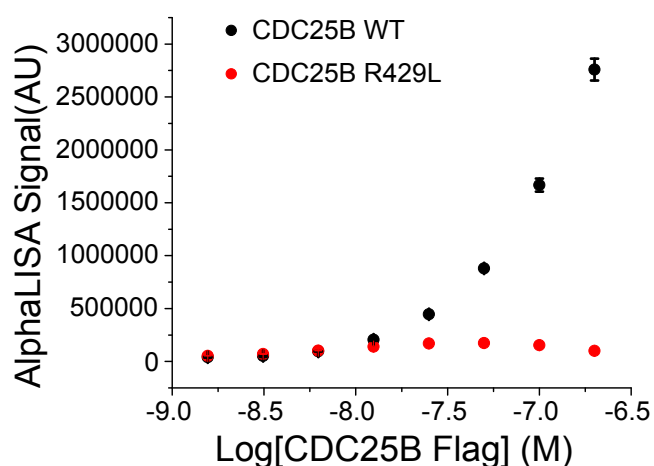
Figure 3.3. *Mutation in the compound **1** binding site disrupts the interaction between CDC25B and CDK2/Cyclin A*. AlphaLISA signal due to the protein-protein interaction between CDC25B and the CDK2/Cyclin A complex. CDC25B WT is shown in black and the hotspot mutation R492L is shown in red.

CDC25B to interact with the substrate using an AlphaLISA-based protein-protein interaction assay. Consistent with the previous report,[18] we found that CDC25B R492L mutant is unable to interact with CDK2/Cyclin A substrate (Figure 3.3). This result strongly supports our finding that compound **1** binds to a functionally important site on CDC25B that is involved in the protein-protein interactions with the substrate.

3.5 Structure guided design of higher affinity analogs of Compound 1

NMR experiments indicated that **1** binds to CDC25B with a relatively low affinity, which is typical for fragment-like compounds.[19] We subsequently explored which functional groups in **1** are essential for interactions with CDC25B. We found that removing either hydroxyl or nitrile groups was detrimental for binding to CDC25B (not shown). Then we tested several commercially available analogs of **1,** and to rank their binding to CDC25B we measured the sum
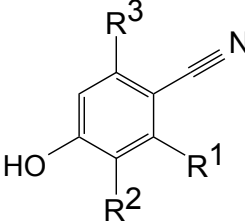
Compound	R^1	R^2	R^3	Sum $\Delta\sigma$ (Hz)
1	-F	-H	-H	169
2	-H	-H	-H	58
3	-Cl	-H	-H	164
4	-H	-Br	-H	49
5	-F	-F	-H	294
6	-F	-H	-F	232
7	-F	-H	$-S(CH_2)_2SO_4$	347
8	-F	-H	$-S(CH_2)_3SO_4$	183

Figure 3.4. *Structure activity relationship (SAR) for 2-fluoro-4-hydroxybenzonitrile analogs.* Structures of compounds tested for binding to CDC25B. Sum Δ was calculated as a sum of the chemical shift perturbations for eight of the most significantly perturbed amide resonances (in Hz) at 2mM compound concentration.
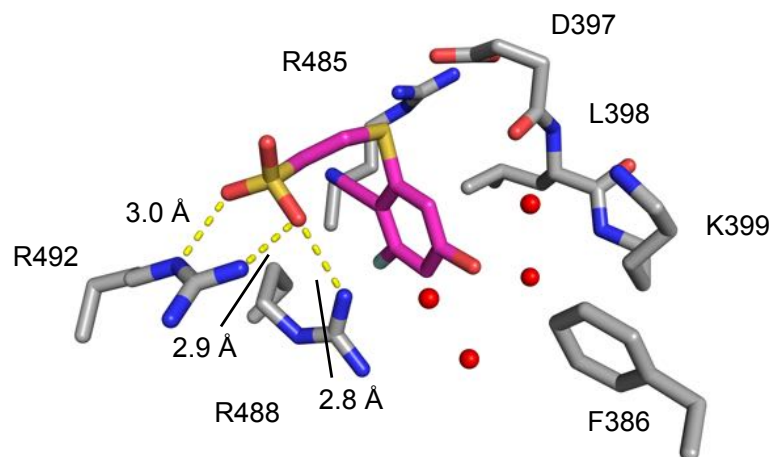
Figure 3.5. *Co-crystal structure of CDC25B bound to compound 7.* Molecular details of the interaction of compound **7** with CDC25B (PDB ID: 4WH9). Distances between the sulfate oxygens and the side-chain nitrogens of Arg488 and Arg492 are given.

of chemical shift changes for eight of the most perturbed amide resonances. Elimination of the fluorine at position R^1 (compound **2**) significantly decreased binding, while exchanging it for chlorine (**3**) had no effect (Figure 3.4). Addition of a second fluorine, either at position R^2 (**5**) or R^3 (**6**) enhanced binding, with a preference for the R^2 position.

We then explored the possibility to improve **1** by linking to an adjacent sulfate ion that was found in the CDC25B-**1** crystal structure and interacts with the side chains of Arg488 and Arg492 (Figure 3.2). Based on the structural data we designed and synthesized two compounds, with a thio-ether at R^3 position and either two- or three-carbon linker to the sulfate moiety (Appendix Figure 3.A1). Compound **8** containing a three-carbon linker showed limited improvement over **1**, while **7** with a two-carbon linker showed more pronounced binding as judged by more extensive chemical shift perturbations (Figure 3.4). Subsequently, we determined the crystal structure of **7** in complex with CDC25B and found that indeed additional

70

interactions are formed between the sulfate group of **7** and Arg488 and Arg492, which contribute to the enhanced binding of this compound (Figure 3.5). This finding further demonstrates the feasibility of developing more potent analogs of **1**.

3.6 Compound 7 inhibits CDC25B by disrupting the CDC25B-CDK2/Cyclin A interaction

We have selected compound **7,** as the most potent and bulky compound, to assess the ability of a small molecule to inhibit the interaction of CDC25B with the CDK2/Cyclin A substrate. For this purpose we employed the AlphaLISA-based protein-protein interaction assay. A dose-dependent decrease in the AlphaLISA signal was observed upon titration with **7**, demonstrating disruption of the CDC25B-CDK2/Cyclin A protein-protein interaction with the IC_{50} value around 1 mM (Figure 3.6). Contrary, much weaker activity has been observed for compound **1**, which binds CDC25B with lower affinity. In addition, only **7** forms hydrogen bonds with two
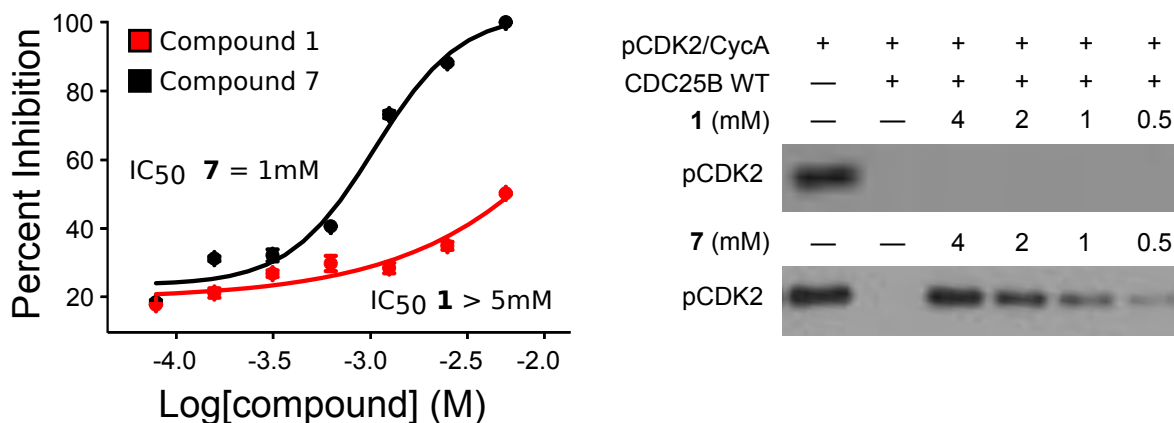
Figure 3.6. *Small molecule ligand binding to the protein-protein interaction site inhibits CDC25B activity*. Left: activity of compound **1** and **7** in an AlphaLISA-based protein-protein interaction assay. Right: *In vitro* phosphatase assay utilizing phosphorylated CDK2/Cyclin A as a substrate for CDC25B in the presence or absence of **1** or **7**. Remaining phosphorylated CDK2/Cyclin A is shown as detected by western blot.

71

arginines (Arg488 and Arg492) which are required for binding of CDK2/CyclinA substrate[20] which may result in higher activity of this compound when compared to **1**. Though activity of **7** is relatively modest, this result provides a proof of principle that ligands that bind to this newly identified site on CDC25B can prevent CDC25B from interacting with the substrate.

Finally, to determine whether disruption of the CDC25B-CDK2/Cyclin A protein-protein interaction by a small molecule results in inhibition of CDC25B activity, we assessed the effect of **7** in an *in vitro* phosphatase assay. We found that incubation with **7** results in a dose-dependent inhibition of CDC25B phosphatase activity towards p-CDK2/Cyclin A substrate (Figure 3.6). At the highest concentration of **7**, CDC25B activity is completely inhibited and it continues to show inhibitory effect down to 500 µM, with an apparent IC_{50} between 1 and 2 mM. Importantly, no inhibitory effect of **1** has been observed emphasizing that activity in phosphatase
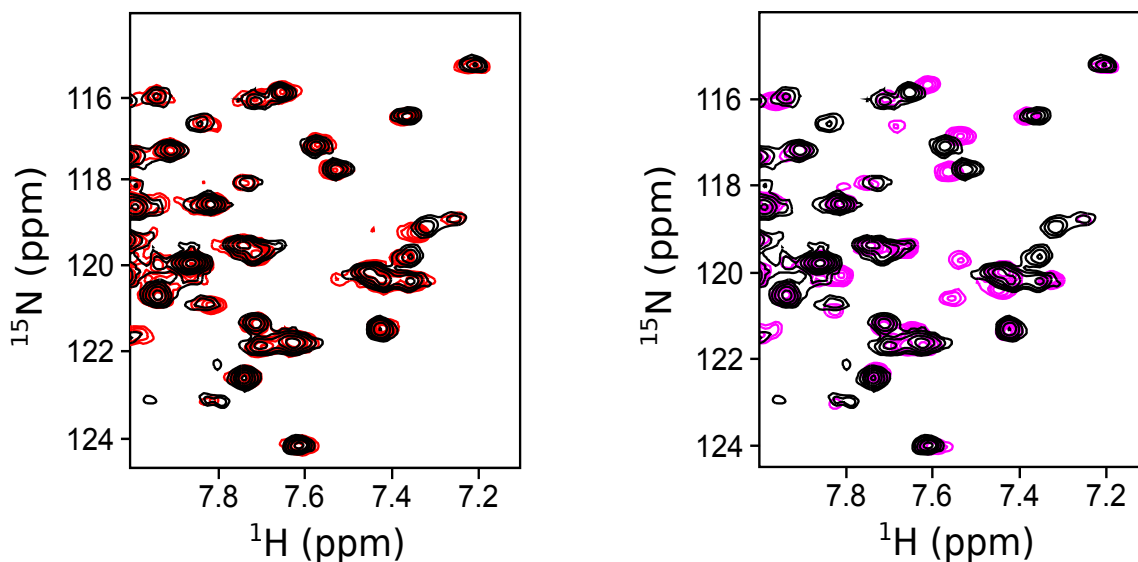
Figure 3.7. *Compound 1 and 7 interact with CDC25A*. Left: A portion of the 1H15-HSQC of CDC25A showing the largest chemical shift perturbations induced by compound **1**. Right: $^1H^{15}N$ chemical shift perturbations induced by compound **7**. The same portion of the spectrum shown for compound **1** is shown. In both spectra CDC25A without compound is shown in black.

assay is correlated with binding affinity to CDC25B (Figure 3.6). These results strongly validate that a small molecule that binds to the protein-protein interaction pocket distal from the active site disrupts the interaction of CDC25B phosphatase with CDK2/Cyclin A substrate and inhibits its phosphatase activity.

3.7 Compounds 1 and 7 also inhibit CDC25A

We have also assessed whether compounds **1** and **7** bind to CDC25A, a close homolog of CDC25B. We found that **1** and **7** binds to CDC25A, although the chemical shift perturbations are less pronounced than for CDC25B (Figure 3.7). In addition compound **7** inhibits the interaction of CDC25A with CDK2/CyclinA with IC_{50}=2.2 mM (Figure 3.8). The binding pockets in CDC25A and CDC25B are very similar though it is likely that selectivity can be achieved for more elaborated analogs.
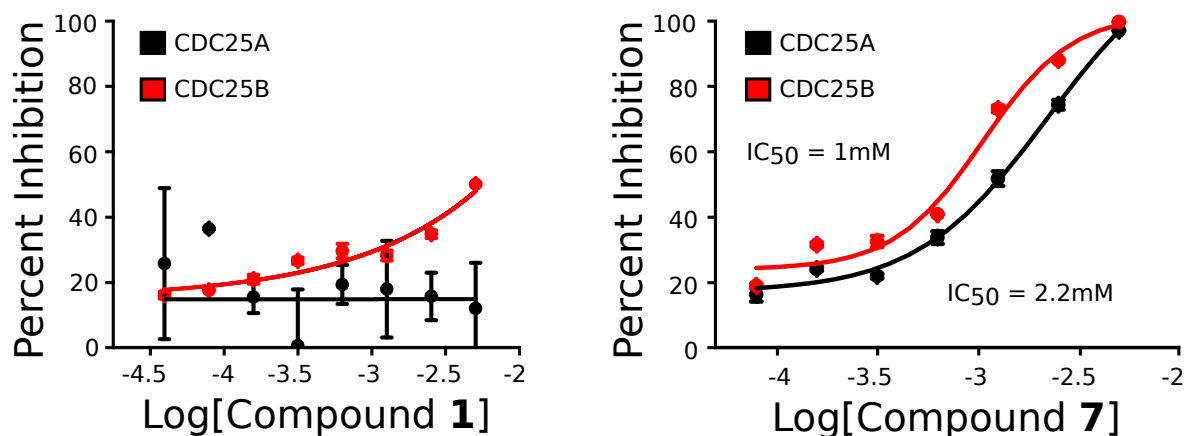
Figure 3.8. *Inhibition of protein-protein interactions by compound 1 and 7*. Left: effect of titration with compound **1** on the interactions of CDC25A and CDC25B with CDK2/CycA. Right: same plot as in A for compound **7**.

3.8 Discussion

In this study, through a fragment-based screening approach, we have identified a small molecule binding site on CDC25B that is distant from the active site and is located adjacent to the residues mediating substrate recognition. Although it has been previously speculated that this pocket might represent a suitable site for inhibitor development,[14] our study demonstrates for the first time that: i) it is possible to identify small molecules that can bind to this site; ii) 2-fluoro-4-hydroxybenzonitrile (compound **1**) represents an attractive small molecule scaffold which binds to this site and can be further optimized into more potent ligands; iii) compounds that bind to this site can disrupt the protein-protein interaction of CDC25B with CDK2/Cyclin A substrate and inhibit the phosphatase activity of CDC25B.

Despite extensive efforts to develop inhibitors of CDC25 phosphatases through targeting the active site,[11–13] no structural information for the phosphatase catalytic domain with bound inhibitor has been reported to date. Here, we describe the structure of CDC25B catalytic domain with two small molecule ligands that bind to a pocket in the vicinity of a protein-protein interaction hot-spot. Interestingly, this pocket is relatively polar and fits a network of hydrogen bonded water molecules. Ligands identified in our study can be likely improved through further modifications to replace these water molecules and optimize contacts with the protein. For example, the extensive network of intermolecular hydrogen bonds between biotin and streptavidin is known to contribute to a very high affinity interaction.[20] In summary, we propose a novel approach to block activity of CDC25 phosphatases via inhibiting their protein-protein interactions with the substrate as an attractive strategy to develop inhibitors for this important class of enzymes.

3.9 Experimental Procedures

Expression and purification of recombinant proteins

The CDC25B catalytic domain (372-551) and variants were expressed in E. coli BL21 (DE3) with an N-terminal GST tag. The CDC25B cDNA with an N-terminal TEV cleavage site was purchased from Genscript and cloned into a pGST-21a vector with NcoI/XhoI. Cells were grown to in either LB or labeled M9 medium. After 16 hr induction with 0.5 mM IPTG at 18 °C, E. coil cells were lysed in a buffer containing 50 mM Tris (pH 8.0), 150 mM NaCl, 1 mM TCEP, and 0.5 mM PMSF. The soluble fraction of the cell lysate was purified using glutathione resin and eluted with lysis buffer containing 50 mM L-glutathione. The eluate was proteolytically cleaved with TEV protease, followed by S-75 size exclusion chromatography in buffer containing 50 mM Tris (pH 8.0), 50 mM NaCl, and 1 mM TCEP. Pure fractions were pooled and frozen at –80 °C. The wild type CDC25A catalytic domain (331-524) and N-terminally Flag tagged CDC25A with the C431S active site mutation were expressed and purified as described above.

pCDK2/Cyclin A was expressed in E. coli BL21 (DE3) by co-expression of three proteins: full-length human CDK2 with a TEV cleavable N-terminal His tag in a pET24 vector, residues 173-432 of human Cyclin A with an N-terminal His-Smt3 tag in a pET24 vector (generously gifted by Dr. Matthew Young, University of Michigan), and full length xenopus Myt1 kinase in the pGS21a vector (gifted from Dr. Sally Kornbluth, Duke University School of Medicine). Unphosphorylated CDK2/Cyclin A was expressed as above, but without the addition of Myt1. After 16 hr induction with 0.1 mM IPTG at 18 °C, E. coil cells were lysed in a buffer containing 50 mM Tris (pH 8.0), 500 mM NaCl, 1 mM β-mercaptoethanol, and 0.5 mM PMSF. The soluble cell lysate was purified using Ni-affinity chromatography. The eluted fractions were pooled and proteolytically cleaved with TEV and ULP1 proteases, followed by S-75 size

exclusion chromatography in buffer containing 50 mM Tris (pH 8.0), 150 mM NaCl, and 1 mM TCEP. Pure fractions were pooled and frozen at −80 °C.

NMR-based fragment screen

The fragment library used for screening was a combination of commercially available fragments and compounds synthesized in-house. Samples for fragment screening were made with 80 μM ^{15}N-labeled CDC25B C473S prepared in a buffer containing 50 mM Tris (pH 7.0), 50 mM NaCl, 1 mM TCEP and 5 % D_2O. Fragments were screened in mixtures of 20 compounds per sample at 250 μM final concentration, in 5% DMSO. ^1H-^{15}N HQSC spectra were acquired at 30 °C on a 600MHz Bruker Avance III spectrometer equipped with cryoprobe, running Topspin version 2.1. Processing and spectral visualization was performed using NMRPipe[21] and Sparky[22]. ^1H-^{15}N HQSC peak assignments were determined previously[17].

Crystallization and structure determination

Crystals of apo-CDC25B C473S ΔC (372-551) were produced as previously published[3]. For compound **1**, crystals were transferred to the mother liquor solution to containing 50 mM **1** in 5% DMSO to soak for 30 minutes and were then transferred to the mother liquor solution containing 50 mM **1**, 5% DMSO, and 20% glycerol for cryoprotection prior to freezing in liquid nitrogen. For compound **7**, crystals were transferred directly to the same cryoprotection solution in the presence of 2mM **7** and 5% DMSO for 2 minutes prior to freezing. Diffraction data was collected for the CDC25B-**1** crystals using an X-ray difractometer at the Center for Structural Biology at the University of Michigan. Diffraction data for the CDC25B-**7** complex was collected at the 21-ID-F beamline at the Life Sciences Collaborative Access Team at the Advanced Photon Source.

The data was integrated and scaled using HKL-3000[23] for **1** and Mosflm[24] for **7** and both structures were solved by molecular replacement with MOLREP[25] using the known apo-CDC25B C473S structure for the search model (PDB code: 2A2K)[3]. Refinement for both structures was performed using REFMAC[26], COOT[27], and the CCP4 program suite[28] (Appendix Table 3.A1). Refinement of anisotropic B-factors was done in the late stages of refinement. The structure was validated using the MOLPROBITY[29] server.

Protein-protein interaction assay

C-terminally 6xHis tagged CDK2/Cyclin A complex and N-terminally Flag tagged CDC25B C473S (372-566) were expressed and purified as stated above. Proteins were incubated together at a final concentration of 10 nM each for 1 hr prior to incubation with compound for 1 hr, followed by addition of Ni-chelate AlphaScreen donor beads (Perkin-Elmer) and Anti-Flag AlphaLISA acceptor beads (Perkin-Elmer) at a final dilution of 1:1000 for 1 hr. Protein-protein interaction assays were quantified using a PheraStar plate reader with excitation at 680 nm wavelength and emission at 615 nm in 20 uL volumes in an uncoated, white, low-volume, 384-well plate (Corning). Assays were performed in a buffer containing 50 mM MOPS (pH 7.25), 50 mM NaCl, 10mM $MgCl_2$, 1mM TCEP, with addition of 1mM ATP, 0.01% BSA, and 0.01% Tween-20 immediately prior to the start of the assay. The protein-protein interaction assay for the interaction between CDK2/Cyclin A and N-terminally Flag tagged CDC25A C431S (331-524) was performed as above.

CDC25B phosphatase activity assay

Wild-type CDC25B (372-566) at 250 nM was incubated with **7** for 1 hr in buffer containing 50

mM Tris (pH 8.0), 50 mM NaCl, 1 mM TCEP, and 5% DMSO, followed by the addition of 500

nM pCDK2/Cyclin A. After 50 minutes at room temperature, the reaction was quenched by

adding 1:1 equivalents of 2x SDS-PAGE loading buffer. Reaction samples were separated on a

4-20% SDS gel 170 volts for 45 minutes. Proteins were transferred to nitrocellulose with a wet

electrotransfer system (BioRad) for 60 min at 25 volts. Subsequently, the membrane was blocked

with 5% BSA in Tris-buffered saline with 0.1% Tween-20 (TBS-T), and incubated overnight at

4 °C with anti-pT15-cdc2 monoclonal antibody (#9111, Cell Signaling Technology, 1:2000).

After washing, the membrane was incubated with an HRP conjugated anti-rabbit antibody

(1:10,000) and visualized.

Compound Synthesis*

All solvents and reagents (including compounds **1-6**) were used as obtained from commercial
sources unless otherwise indicated. The ^{1}H NMRs were taken on a Bruker Avance III 600MHz
or Varian MR400. Chemical shifts were reported in ppm relative to tetramethylsilane or residual
solvent signal. The mass measurements were determined on a Micromass LCT time-of-flight
mass spectrometer using positive mode and electrospray ionization. The exact mass
measurements were determined on Agilent Q-TOF time-of-flight mass spectrometer using
positive or negative ion mode and electrospray ionization. Analytical TLC was performed on
Merck TLC aluminum plates precoated with F_{254} silica gel 60 (UV, 254 nm, and iodine). Infrared
(IR) spectra were recorded on Perkin-Elmer FT-IR Spectrum BX on neat powder and only major
characteristic signals are reported.

2,6-difluoro-4-(methoxymethoxy)benzonitrile (6)
In 10 mL of DCM were dissolved 1 g of 2,6-difluoro-4-hydroxybenzonitrile (6.45 mmol, 1 eq)
and 1 g of DIPEA (7.74 mmol, 1.2 eq). Then 0.571 g of MOMCl (7.09 mmol, 1.1 eq) were added,
and the reaction mixture was allowed to stand at r.t. overnight. Next day the mixture was filtered
through 20 g of silica gel, eluting with DCM, and the solvent was evaporated.
> Yield 1.28 g (100%). Colorless oil.
> ^{1}H NMR (499.68 MHz, CDCl$_3$): δ = 3.49 (s, 3H, MeO), 5.21 (s, 2H, CH$_2$), 6.72 (d,
> 2H, $^3J_{(H-F)}$ = 9.95 Hz).
> ^{19}F NMR (470.12 MHz, CDCl$_3$): δ = 103.0 (d, $^3J_{(H-F)}$ = 9.95 Hz).

*All compound sythesis was performed by Sergii Dudkin

^{13}C NMR (150.92 MHz, CDCl$_3$): δ = 56.75 (OMe), 85.44 (t, $^2J_{(C-F)}$ = 19.8 Hz, C-1), 94.75 (OCH$_2$O), 100.8 (dd, $^2J_{(C-F)}$ = 23.1 Hz, $^4J_{(C-F)}$ = 2.2 Hz, CH$_{Ar}$-3, CH$_{Ar}$-5), 109.6 (CN), 162.9 ($^3J_{(C-F)}$ = 13.2 Hz, C-4), 164.2 (dd, $^1J_{(C-F)}$ = 259.1 Hz, $^1J_{(C-F)}$ = 6.7 Hz). IR (ATR, cm^{-1}): ṽ = 3098 (w), 2942 (w), 2836 (w), 2240 (w), 2156 (w), 2082 (w), 2008 (w), 1634 (s), 1574 (m), 1496 (m), 1454 (m), 1350 (m), 1308 (w), 1218 (m), 1158 (m), 1140 (s), 1076 (s), 1044 (s), 1004 (s), 920 (s), 842 (m), 716 (m), 688 (w).

2-[(2-Cyano-3-fluoro-5-hydroxyphenyl)thio]ethanesulfonic acid, sodium salt (7)

Into a 25-mL round bottom flask were placed 0.150 g of 2,6-difluoro-4-(methoxymethoxy) benzonitrile 9 (0.753 mmol, 1 eq), 0.124 g of sodium 2-mercaptoethanesulfonate (0.753 mmol, 1 eq), 0.160 g of sodium carbonate (1.51 mmol, 2 eq) and 1.5 mL of DMF. The reaction mixture was stirred at 100 °C under argon for 3 days. Then DMF was evaporated, the residue was dissolved in water and treated with 0.78 mL of conc. HCl. After ½ h the acid was removed in vacuum, the residue was dissolved in methanol and evaporated with 2 g of silica gel. Column chromatography was performed with 7 g of silica gel, eluting first with pure EtOAc, then with EtOAc/EtOH 5:2.

Yield 0.068 g (30%). Off-white solid.

^{1}H NMR (600.13 MHz, DMSO-d$_6$): δ = 2.72 (t, 2H, ^3J = 8.16 Hz, CH$_2$-SO$_3$Na), 3.24 (t, 2H, ^3J = 8.16 Hz, CH$_2$-S), 6.61 (dd, 1H, $^3J_{(H-F)}$ = 11.33 Hz, ^4J = 1.59 Hz, H-4), 6.71 (d, 1H, ^4J = 1.59 Hz, H-6), 11.37 (br s, 1H, OH).

^{13}C NMR (150.92 MHz, DMSO-d$_6$): δ = 27.7 (CH$_2$-S), 50.0 (CH$_2$-SO$_3$Na), 89.3 (d, $^2J_{(C-F)}$ = 17,6 Hz, C-2), 100.4 (d, $^2J_{(C-F)}$ = 22.1 Hz, CH-4), 109.7 (CH-6), 112.9 (CN), 144.7 (d, $^3J_{(C-F)}$ = 2.2 Hz, C-1), 163.5 (d, $^3J_{(C-F)}$ = 13.2 Hz, C-5), 164.8 (d, $^1J_{(C-F)}$ = 239.5 Hz, C-3).

^{19}F NMR (282.38 MHz, DMSO-d$_6$): δ = –105.9 (d, 1F, $^3J_{(H-F)}$ = 11.33 Hz).

HRMS (ESI): Calcd. for C$_9$H$_7$FNO$_4$S$_2$ [M-Na]$^-$: 275.9806, found: 275.9813.

3-[(2-Cyano-3-fluoro-5-hydroxyphenyl)thio]propane-1-sulfonic acid, sodium salt (8)

This compound was prepared similarly to 2-[(2-Cyano-3-fluoro-5-hydroxyphenyl)thio] ethanesulfonic acid, sodium salt (7), starting from 0.150 g of 2,6-difluoro-4-(methoxymethoxy)benzonitrile (0.753 mmol, 1 eq) and 0.134 g of sodium 3-mercaptopropanesulfonate (0.753 mmol, 1 eq).

Yield 0.154 g (65%).

^{1}H NMR (600.13 MHz, DMSO-d$_6$): δ = 1.86-1.95 (m, 2H, CH$_2$), 2.56 (t, 2H, ^3J = 6.97 Hz, CH$_2$-SO$_3$Na), 3.14 (t, 2H, ^3J = 6.97 Hz, CH$_2$-S), 6.44 (d, 1H, $^3J_{(H-F)}$ = 9.54 Hz, H-4), 6.60 (s, 1H, H-6), 8.31 (br s, 1H, OH).

^{19}F NMR (470.12 MHz, DMSO-d$_6$): δ = 106.87 (s, 1F).

^{13}C NMR (150.92 MHz, DMSO-d$_6$): 24.7 (CH$_2$), 30.52 (CH$_2$-S), 49.87 (CH$_2$-SO$_3$Na), 87.1 (C-2), 100.5 (CH-4), 110.6 (CH-6), 113.6 (CN), 144.1 (C-1), 162.3 (C-5), 165.0 (d, $^1J_{(C-F)}$ = 253.1 Hz, C-3).

HRMS (ESI): Calcd. for C$_{10}$H$_9$FNO$_4$S$_2$ [M-Na]$^-$: 289.9963, found: 289.9979.

Notes

This chapter is based on the publication "Inhibition of CDC25B phosphatase through disruption of protein-protein interaction", (2014) ACS Chem Biol by George Lund, Sergii Dudkin, Dmitry Borkin, Wendi Ni, Jolanta Grembecka, and Tomek Cierpicki. George Lund and Tomek Cierpicki designed the experiments; George Lund performed the NMR experiments, crystallography studies and in vitro assays; Sergii Dudkin and Dmitry Borkin synthesized compounds **6**, **7**, and **8**; Wendi Ni helped with protein expression and purification; Jolanta Grembecka advised the project and helped edit the manuscript.

3.10 Appendices
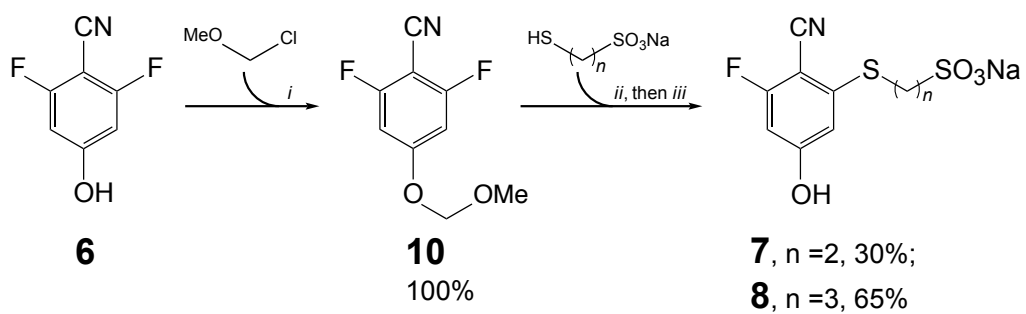
Appendix Figure 3.A1. *Synthesis of compounds 7 and 8.* Schematics and yields are shown for the synthesis of compounds **7** and **8**.
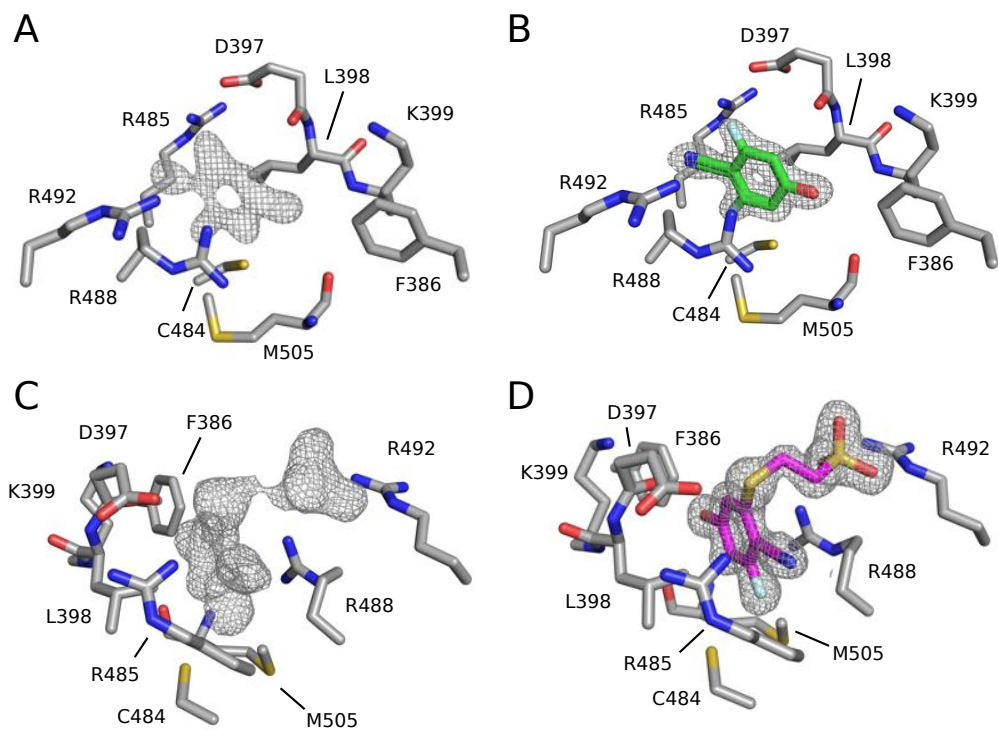
Appendix Figure 3.A2. *Electron density for compounds 1 and 7 before and after refinement.*
A) Fo-Fc electron density map cut at 3.0 σ for compound **1** prior to molecular replacement.
B) 2Fo-Fc map cut at 1.5 σ for compound **1** after refinement. C) Fo-Fc map cut at 2.0 σ for
compound **7** prior to molecular replacement. D) 2Fo-Fc map cut at 1.0 σ for compound **7**
after refinement.

Appendix Table 3.A1. *Crystallographic data collection and refinement statistics*.

	CDC25B-**1**	CDC25B-**7**
PDB code	4WH7	4WH9
Data collection		
Space group	$P2_12_12_1$	$P2_12_12_1$
Cell dimensions		
a, b, c (Å)	51.2, 71.4, 73.5	51.7, 71.5, 73.9
Resolution (Å)	1.62 (1.65-1.62)	1.50 (1.58-1.50)
Unique reflections	35426 (1746)	44620 (6450)
R_{sym}	0.154 (0.467)	0.081 (0.538)
$I / \sigma I$	28.6 (2.3)	14.3 (3.8)
Completeness (%)	90.7 (90.2)	100.0 (100.0)
Redundancy	2.3 (2.2)	7.3 (7.3)
Refinement		
R_{work} / R_{free} (%)	15.7 / 19.8	12.8 / 15.2
No. atoms		
Protein	1511	1528
Water	287	296
Mean B-factors ($Å^2$)	24.4	20.3
R.m.s. deviations		
Bond lengths (Å)	0.011	0.012
Bond angles (°)	1.187	1.928
Ramachandran plot		
Most favored regions (%)	97.2	97.3
Additional allowed regions (%)	2.8	2.7

3.11 References

1.   Nilsson, I. & Hoffmann, I. Cell cycle regulation by the Cdc25 phosphatase family. *Prog. Cell Cycle Res.* **4,** 107–14 (2000).

2.   Sebastian, B., Kakizuka, A. & Hunter, T. Cdc25M2 activation of cyclin-dependent kinases by dephosphorylation of threonine-14 and tyrosine-15. *Proc. Natl. Acad. Sci. U. S. A.* **90,** 3521–4 (1993).

3.   Sohn, J., Buhrman, G. & Rudolph, J. Kinetic and structural studies of specific protein-protein interactions in substrate catalysis by Cdc25B phosphatase. *Biochemistry* **46,** 807–818 (2007).

4.   Nishioka, K. *et al.* Clinical significance of CDC25A and CDC25B expression in squamous cell carcinomas of the oesophagus. *Br. J. Cancer* **85,** 412–21 (2001).

5.   Ito, Y. *et al.* Expression of cdc25B and cdc25A in medullary thyroid carcinoma: cdc25B expression level predicts a poor prognosis. *Cancer Lett.* **229,** 291–7 (2005).

6.   Takemasa, I. *et al.* Overexpression of CDC25B phosphatase as a novel marker of poor prognosis of human colorectal carcinoma. *Cancer Res.* **60,** 3043–50 (2000).

7.   Broggini, M. *et al.* Cell cycle-related phosphatases CDC25A and B expression correlates with survival in ovarian cancer patients. *Anticancer Res.* **20,** 4835–40

8.   Yan, X., Chua, M., He, J. & So, S. Small interfering RNA targeting CDC25B inhibits liver tumor growth in vitro and in vivo. *Mol Cancer* **7,** 19 (2008).

9.   Liffers, S.-T. *et al.* MicroRNA-148a is down-regulated in human pancreatic ductal adenocarcinomas and regulates cell survival by targeting CDC25B. *Lab. Invest.* **91,** 1472–9 (2011).

10.   Zhang, Z., Zhang, G. & Kong, C. High expression of Cdc25B and low expression of 14-3-3σ is associated with the development and poor prognosis in urothelial carcinoma of bladder. Tu*mour Biol.* **35,** 2503–12 (2014).

11.   Lavecchia, A., Di Giovanni, C. & Novellino, E. Inhibitors of Cdc25 phosphatases as anticancer agents: a patent review. *Expert Opin. Ther. Pat.* **20,** 405–25 (2010).

12.   Lavecchia, A., Di Giovanni, C. & Novellino, E. CDC25 phosphatase inhibitors: an update. *Mini Rev. Med. Chem.* **12,** 62–73 (2012).

13.   Lyon, M. A., Ducruet, A. P., Wipf, P. & Lazo, J. S. Dual-specificity phosphatases as targets for antineoplastic agents. *Nat. Rev. Drug Discov.* **1,** 961–76 (2002).

14.   Rudolph, J. Inhibiting transient protein–protein interactions: lessons from the Cdc25 protein tyrosine phosphatases. *Nat. Rev. Cancer* **7,** 202–11 (2007).

15.   Kristjánsdóttir, K. & Rudolph, J. Cdc25 phosphatases and cancer. *Chem. Biol.* **11,** 1043–1051 (2004).

16.   Bolton, J. L., Trush, M. A., Penning, T. M., Dryhurst, G. & Monks, T. J. Role of quinones in toxicology. *Chem. Res. Toxicol.* **13,** 135–60 (2000).

17.   Lund, G. & Cierpicki, T. Solution NMR studies reveal no global flexibility in the

catalytic domain of CDC25B. *Proteins* **82,** 2889–95 (2014).

18.   Sohn, J., Parks, J. & Buhrman, G. Experimental validation of the docking orientation of Cdc25 with its Cdk2-CycA protein substrate. *Biochemistry* **44,** 16563–16573 (2005).

19.   Scott, D. E., Coyne, A. G., Hudson, S. A. & Abell, C. Fragment-based approaches in drug discovery and chemical biology. *Biochemistry* **51,** 4990–5003 (2012).

20.   Sohn, J. & Rudolph, J. The energetic network of hotspot residues between Cdc25B phosphatase and its protein substrate. *J. Mol. Biol.* **22,** 4109 (2008).

21.   Delaglio, F. *et al.* NMRPipe: a multidimensional spectral processing system based on UNIX pipes. *J. Biomol. NMR* **6,** 277–93 (1995).

22.   Goddard, T. G. & Kneller, D. G. SPARKY 3.

23.   Minor, W., Cymborowski, M., Otwinowski, Z. & Chruszcz, M. HKL-3000: the integration of data reduction and structure solution--from diffraction images to an initial model in minutes. *Acta Crystallogr. D. Biol. Crystallogr.* **62,** 859–66 (2006).

24.   *Evolving Methods for Macromolecular Crystallography*. **245,** (Springer Netherlands, 2007).

25.   Vagin, A. & Teplyakov, A. Molecular replacement with MOLREP. *Acta Crystallogr. D. Biol. Crystallogr.* **66,** 22–5 (2010).

26.   Murshudov, G. N., Vagin, A. A. & Dodson, E. J. Refinement of macromolecular structures by the maximum-likelihood method. *Acta Crystallogr. D. Biol. Crystallogr.* **53,** 240–55 (1997).

27.   Emsley, P. & Cowtan, K. Coot: model-building tools for molecular graphics. *Acta Crystallogr. D. Biol. Crystallogr.* **60,** 2126–32 (2004).

28.   The CCP4 suite: programs for protein crystallography. *Acta Crystallogr. D. Biol. Crystallogr.* **50,** 760–3 (1994).

29.   Davis, I. W. *et al.* MolProbity: all-atom contacts and structure validation for proteins and nucleic acids. *Nucleic Acids Res.* **35,** W375–83 (2007).

Chapter 4

High-throughput screening to identify inhibitors of the CDC25B-CDK2/Cyclin A protein-protein interaction

4.1 Abstract

Aberrant activation of the CDK2/Cyclin A complex by the phosphatase CDC25B in cancer has resulted in significant drug discovery efforts to inhibit CDC25B activity. To date, all high-throughput screening efforts targeting CDC25B have used artificial substrates in order to identify inhibitors of CDC25B enzymatic activity. As discussed in Chapter 1, the inhibitors identified in such screens have several drawbacks. In order to identify new classes of CDC25B inhibitors, alternative screening methods must be developed.

Here, we describe the development of multiple assays for the quantification of the CDC25B-CDK2/Cyclin A protein-protein interaction (PPI). These assays were used to screen for small molecule inhibitors of the CDC25B-CDK2/Cyclin A interaction in three separate high-throughput screening campaigns at the University of Michigan Center for Chemical Genomics. From these screening campaigns, we identified several inhibitors of the CDC25B-CDK2/Cyclin A PPI with activity in vitro and for one compound, in pancreatic cancer cells. Importantly, we have established a novel, high-quality screening assay for the identification of CDC25B-CDK2/ Cyclin A PPI inhibitors. This assay represents a novel approach to the identification of new CDC25B inhibitor classes.

4.2 Introduction

As described in Chapter 1, the CDC25 phosphatases are critical regulators of the cell cycle and are overexpressed in many types of cancer. Furthermore, many studies detailed in Chapter 1 have implicated CDC25B as a target for therapeutic intervention. Previous attempts to identify CDC25B inhibitors using high-throughput screening (HTS) efforts have been exclusively focused on the use of artificial substrates to observe inhibition of CDC25B enzymatic activity[1–4]. As discussed in Chapter 1, this approach has been shown to have several limitations. First, the reactivity of the catalytic cysteine has led to the discovery of reactive covalent modifiers of CDC25s that have been unsuccessful as therapeutic candidates[5,6]. Second, several previously characterized inhibitors of CDC25B inhibit its cellular activity indirectly through the generation of intracellular reactive oxygen species[7–10], which has many other cellular effects outside of CDC25B inhibition[11]. Third, the active sites of the CDC25s are shallow, and do not confer substrate recognition[12]. For these reasons, new approaches for the discovery of small molecule inhibitors targeting this class of enzymes are required.

Recently, the concept of "gray box" screening approach to discovery of small molecule inhibitors or activators has been introduced[13,14]. Gray box screening involves reconstituting an entire biologically relevant system in a biochemical assay for use in inhibitor screening. This includes using entire protein complexes with their relevant cofactors, phosphorylation states, etc. The advantage of the "gray box" approach over a typical biochemical assay is to better recapitulate the entire biological system. The "gray box" screening concept is also contrasted with cell-based screening approach, sometimes referred to as "black box" screening. A Limitation of cell-based screening is the significant effort required to determine the molecular target of identified hits and determine their mechanism of action.

"Gray box" screening represents an attractive approach to target CDC25B. As detailed in Chapter 1, a primary pitfall of previous assays targeting CDC25B was the use of artificial substrates to target CDC25B enzymatic activity. Reconstituting the entire biological system of CDC25B and its substrate CDK2/Cyclin A removes the bias towards identification of active site inhibitors. As characterized in Chapter 2, recognition of the CDK2/Cyclin A complex by CDC25B is mediated primarily through two sites distant from the active site. The gray box screening approach has the potential inhibit substrate recognition by targeting these PPI sites.

Here, we describe our efforts to identify and optimize a high-quality "gray box" screening assay for the CDC25B-CDK2/Cyclin A interaction. We have iteratively optimized multiple assays and tested them in three distinct HTS campaigns. Ultimately, we used the optimized assay in large-scale screen in order to identify small molecule inhibitors of the CDC25B-CDK2/Cyclin A PPI.

4.3 Biochemical assays and high-throughput screening strategy

Several biochemical assays are compatible with "gray box" screening to identify protein- protein interaction (PPI) inhibitors. Two assays have been frequently used to quantify the extent of the PPI between proteins[15–17]. One of these is the Amplified Luminescent Proximity Homogeneous Assay, or AlphaLISA assay[16,18]. This assay uses the transfer of a singlet oxygen species between two fluorophore-conjugated beads to detect the proximity of the two fluorophores. Upon fluorescent excitation, the singlet oxygen is released from the donor bead. If an acceptor bead is within approximately 1000 Å of the donor, the transfer of the singlet oxygen induces the acceptor bead to fluoresce. When conjugated with antibodies, the AlphaLISA reagents can quantify the interaction of two proteins of interest.

A second frequently used assay for PPI quantification is the homogeneous time-resolved

fluorescence (HTRF) assay[19,20]. Conceptually, the HTRF assay is similar to the AlphaLISA assay. Antibody-conjugated fluorescent beads recognizing proteins of interest are used to quantify the extent of the PPI. The primary difference between the two assays is the fluorescent induction mechanism of the acceptor fluorophore. Instead of the reactive singlet oxygen species used in the AlphaLISA assay, the HTRF assay relies on fluorescent resonance energy transfer (FRET) to quantify bead proximity. HTRF energy transfer occurs most efficiently at distances of less than 100 Å.

The development of a high-quality biochemical assay for HTS depends on the rigorous assessment of its statistical robustness during assay development and through the HTS campaign. Several statistical measures have been established as important metrics for assessing the quality of a given assay. We primarily employed three of these measures: the signal-to-noise (S/N), the coefficient of variation (CV)[21], and the Z-factor[22]. In our assays, the S/N is calculated as the ratio of the positive control measurement with all assay components to the negative control measurement without protein reagents. The second measure used is the CV, which is a standardized measure of the variability between measurements and reported as a percentage. Lower CVs indicate lower measurement variability. The third statistical metric, the Z-factor, is widely used for determining the quality of a high-throughput assay. The Z-factor takes into account both the S/N between positive and negative controls as well as the standard deviations of both controls (Equation 1). With an upper limit of 1, an assay with a Z-factor greater than 0.5 is considered an acceptable assay[22].

Equation 4.1

$$Z\text{-}factor = 1 - \frac{3(\sigma_p + \sigma_n)}{|\mu_p - \mu_n|}$$

The HTS approach used in in our screening campaigns described below employed a 3 stage format: a primary screening stage with a single point measurement per compound, followed by a confirmation screening stage where selected compounds from the primary screen were retested, and a final dose-response stage where compounds titrations were performed. Hits in our assays were defined as compounds demonstrating inhibition greater than 3 standard deviations compared to plate negative controls (hereafter called 3SD).

4.4 HTS-1: AlphaLISA-based high-throughput screening for inhibitors of CDC25B-CDK2/Cyclin A

4.4.1 Optimization of the AlphaLISA assay for HTS

To identify inhibitors of the CDC25B-CDK2/Cyclin A protein-protein interaction, we tested both the AlphaLISA and HTRF assays. For assay development, we designed a C-terminally Flag tagged, catalytically inactive CDC25B phosphatase domain mutant C473S (CDC25B-Flag) and an N-terminally 6xHis tagged CDK2 protein in complex with the CDK2 binding domain of Cyclin A (His-CDK2/Cyclin A). Protein constructs are detailed in Table 4.A1. We first
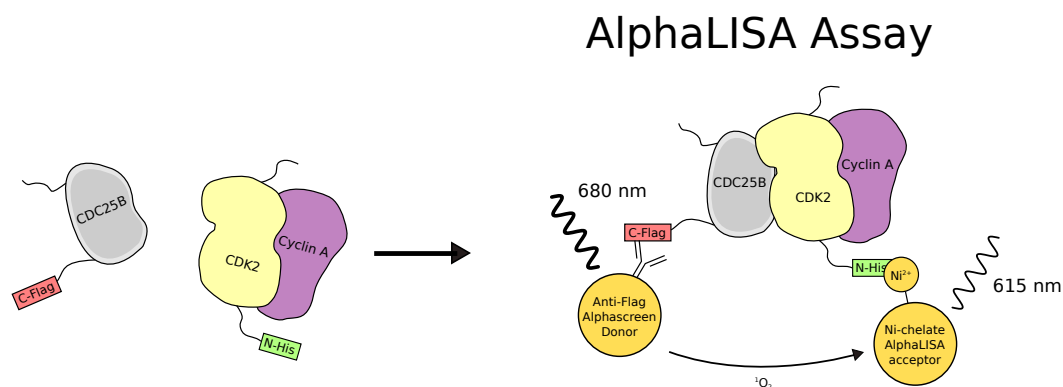

Figure 4.2. *Design of the AlphaLISA assay*. Schematic of the CDC25B-CDK2/Cyclin A AlphaLISA assay.

optimized the AlphaLISA assay using Ni-chelate Alpha donor beads and anti-Flag AlphaLISA

acceptors beads (Figure 4.2). Compared to buffer controls, the optimized AlphaLISA assay with

our protein reagents produced a 10-fold S/N. We also attempted to develop the HTRF assay using

anti-6xHis europium cryptate donor beads and anti-Flag XL-665 acceptor beads. However,

development of the HTRF assay was unsuccessful. We therefore moved ahead with validation

of the AlphaLISA assay. In competition experiments with untagged CDK2/Cyclin A complex,

the AlphaLISA signal showed dose-dependent inhibition of the CDC25B-Flag and His-CDK2/

Cyclin A PPI. As CDC25B dephosphorylates Thr14 and Tyr15 on CDK2, we assessed whether

or not this modification affected the CDC25B-CDK2/Cyclin A PPI in our assay. Titration with

either untagged CDK2/Cyclin A or untagged pT14-pY15-CDK2/Cyclin A disrupted the

AlphaLISA signal in a dose-dependent matter with similar affinities (Figure 4.3). This indicated

that the PPI between CDC25B and CDK2/Cyclin A was not affected by CDK2 phosphorylation

state at Thr14 and Tyr15. Once our AlphaLISA assay was validated for sensitivity to inhibition

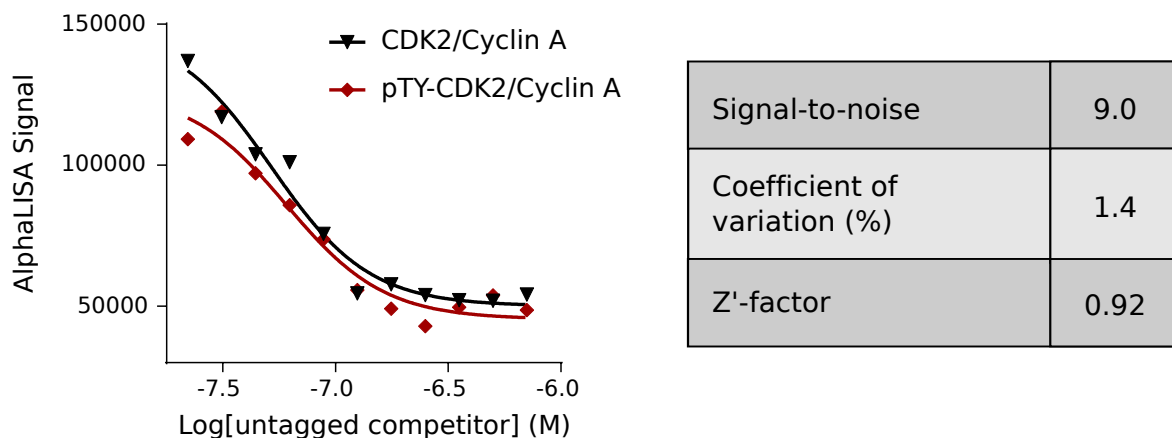| Signal-to-noise | 9.0 |
| Coefficient of variation (%) | 1.4 |
| Z'-factor | 0.92 |

Figure 4.3. *Validation of the HTS-1 AlphaLISA assay.* Left: Competition of untagged pT14pY15-CDK2/Cyclin A (red) and unphosphorylated CDK2/Cyclin A (black) in the AlphaLISA assay. Right: Pre-HTS assay statistics for the AlphaLISA assay.

by untagged CDK2/Cyclin A, the assay was optimized for HTS. The S/N, CV, and Z-factor for a single 384-well control plate using our AlphaLISA assay under HTS conditions was 9.0, 1.4% and 0.92 respectively, indicating that our assay was of high quality.

4.4.2 Primary screening for HTS-1

In the primary screening stage, we screened 64,640 compounds from the compound library of the University of Michigan's Center for Chemical Genomics (UM-CCG). In order to allow for the identification of potentially weak inhibitors, we screened using a relatively high compound concentration of approximately 35 μM. Compared to assay plate controls, the AlphaLISA assay performed well under HTS conditions with an average Z-factor of 0.80; data from an example 16 plate day of screening is shown in Figure 4.4. Despite the high performance of the assay with respect to the controls, we observed a very high hit rate of 17.8% as determined by 3SD for the primary screen, resulting in 11,514 hit compounds.
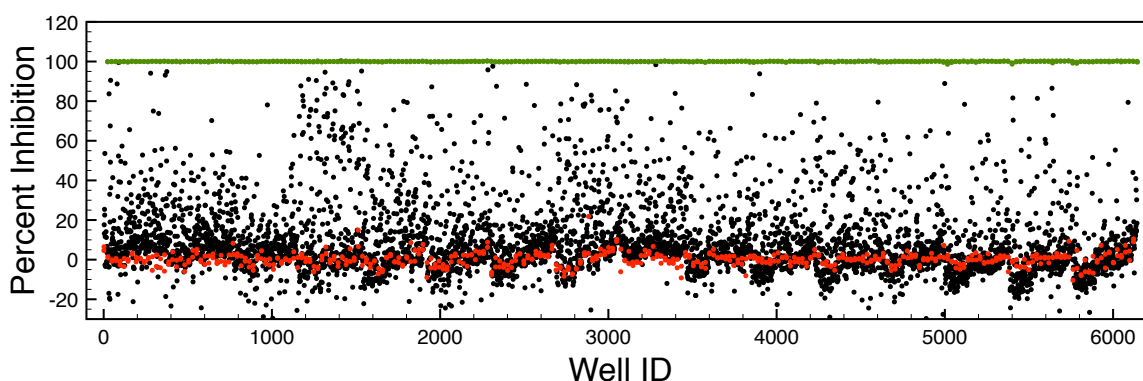

Figure 4.4. *HTS-1 performance.* High-throughput screening performance of 16 384-well plates (plate numbers 5318-5333) from a single day of screening. A scatter plot containing positive controls (green), negative controls (red), and compound wells (black) is shown.

Due to the high hit rate in the primary screen, additional analysis was required to select compounds for progression to the confirmation stage. First, the 11,514 hit compounds defined in the primary screen were clustered by similarity as detailed in the methods section to eliminate chemically redundant compounds. The most potent compound from each cluster was selected for further analysis. The 4039 compounds remaining after clustering were analyzed by manual inspection to further eliminate redundant scaffolds and to remove quinone-containing compounds for the reasons detailed in Chapter 1. After manual analysis, the top 3200 compounds with the strongest inhibition were selected for advancement to the confirmation screening stage.

4.4.3 Confirmation screening for HTS-1

Confirmation screening was conducted by testing compounds in two assays, the AlphaLISA assay used for the primary screening stage as well as a control AlphaLISA counter screen. The AlphaLISA counter screening assay was developed as a method to eliminate compounds that
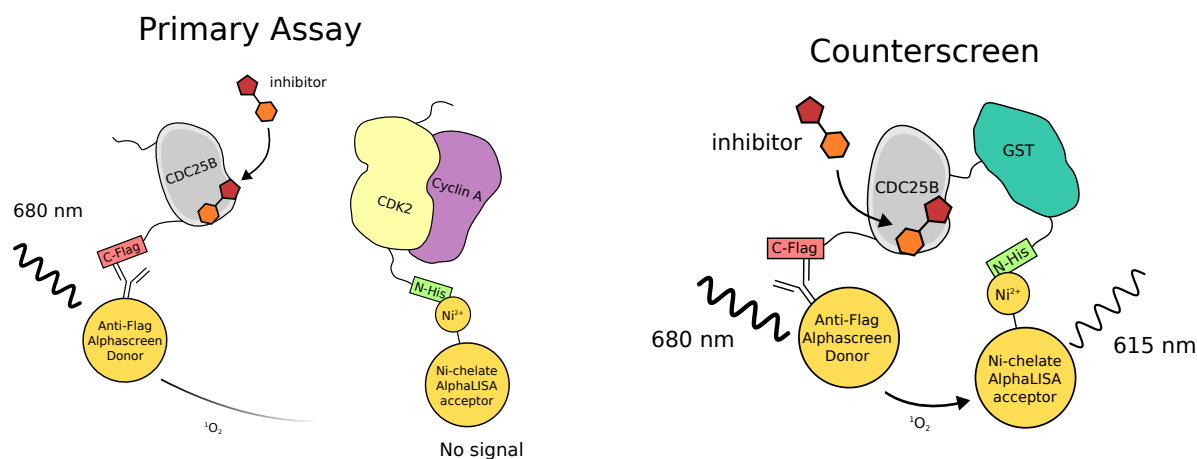

Figure 4.5. *Primary and counter screening assays.* Left: schematic of inhibition in the AlphaLISA primary screening assay by small molecule inhibitors. Right: schematic of the AlphaLISA-based counter screening method for the elimination of assay interfering compounds.
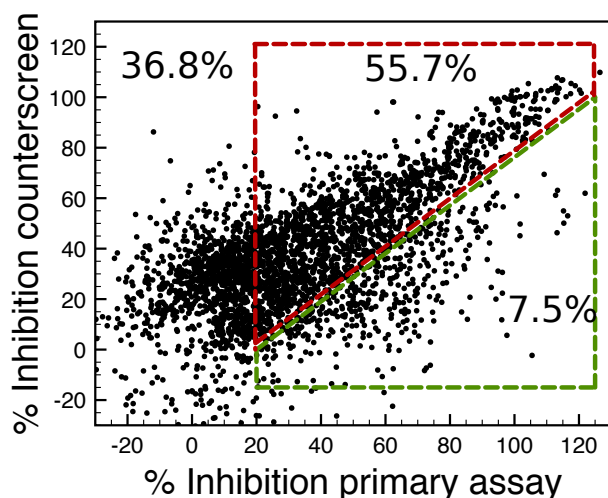
Figure 4.6. *HTS-1 confirmation screening results*. The green dotted box denotes compounds selected for dose-response experiments; the red dotted box denotes compounds eliminated by the AlphaLISA counter screen. Percentages are given for each area.

potentially interfere with the AlphaLISA assay. To this end, we designed a protein construct with a N-terminal 6xHis tag, the CDC25B catalytic domain, and a C-terminal Flag tag (His-CDC25B-Flag) as described in Table 4.A1. This protein was then used in the AlphaLISA assay in place of the CDC25-Flag and His-CDK2/Cyclin A protein combination used in the primary assay. Since the tags in the His-CDC25B-Flag counter screening assay cannot be separated, any decrease in AlphaLISA signal observed in this assay must be due to compound interference (Figure 4.5). The 3200 compounds selected from the primary screening stage were tested using both assays in duplicate at 35 µM concentration. Of the 3200 compounds, 2023 that showed activity greater than 20% in the primary assay were selected for further analysis. Of this set, the 360 compounds with at least 20% more inhibition in the primary assay than in the counter screening assay were selected for the dose-response stage. The bounded box in Figure 4.6 shows a visual representation of compound selection.

4.4.4 Dose response and follow up for HTS-1

For the final dose-response stage, the 360 compounds selected from the confirmation screen were tested in duplicate in titration experiments using the AlphaLISA primary assay. Titration experiments were performed in an 8-point, 2-fold dilution series format starting at 150μM concentration, followed by sigmoidal curve fitting analysis. Of the 360 compounds tested, 63 exhibited dose-dependent inhibition of the AlphaLISA signal with an IC_{50} greater than 50μM and were considered as active hits. A breakdown of HTS-1 results is given in Figure 4.7.

Twenty-six of these active compounds were ordered from commercial sources for retesting. Of the compounds dissolved from fresh powder, 18 showed activity similar to or greater than that observed during the dose response experiments. The validated compounds had a variety of scaffolds, and included seven compounds with IC_{50} of less than 15μM (Table 4.1). The most potent inhibitor identified was compound CCG-17950 with an IC_{50} of 6 μM (Figure 4.8A).

Primary screen	64,640
Primary hits	11,514
Tested in confirmation	3,200
Tested in DR	360
Active in DR	63
Validated from fresh powder	18
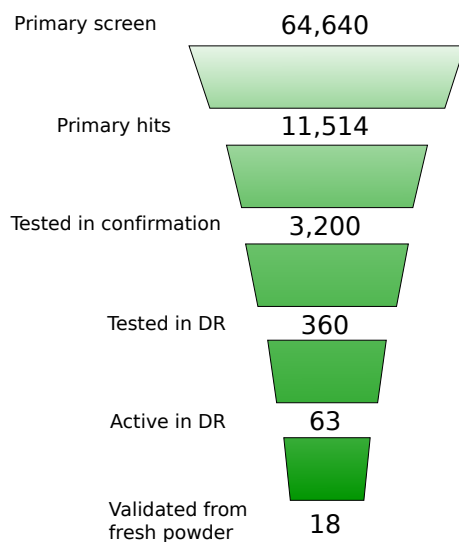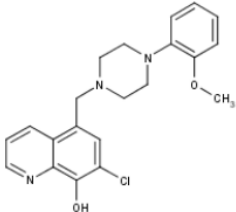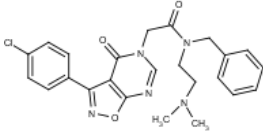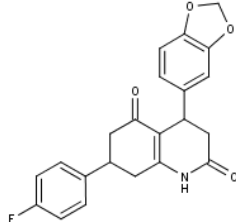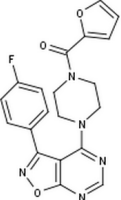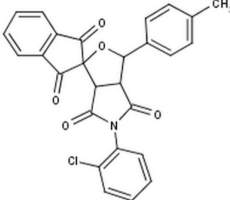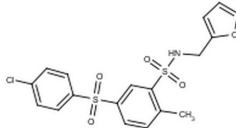
Figure 4.7. *Breakdown of HTS-1 results*

Table 4.1. *Most potent hits validated from HTS-1.*

Name	Structure	Percent primary	Percent secondary	Percent counterscreen	IC50 DR (uM)	IC50 Fresh (uM)
CCG-17950		100.4	88.6	44.5	38.0	5.9
CCG-125215		92.4	101.8	49.8	25.1	8.9
CCG-28155		92.3	96.1	11.8	3.9	14.5
CCG-172232		84.0	94.9	31.1	66.1	15.5
CCG-17560		69.7	77.8	17.4	79.4	17.4
CCG-106526		72.7	88.9	48.3	128.8	18.2

4.4.5 Characterization of CCG-17950

The most potent validated hit compound obtained from HTS-1 was 7-chloro-5-((4-(2-methoxyphenyl)piperazin-1-yl)methyl)quinolin-8-ol, or CCG-17950 (Figure 4.8A). In order to address the mechanism of inhibition for CCG-17950, we used NMR to determine the protein to which it binds. No chemical shift perturbations were observed on a $^1H^{15}N$-HSQC spectrum for CDC25B, indicating that it was not the target of CCG-17950. However, ligand-detected NMR experiments indicated that CCG-17950 binds to the CDK2/Cyclin A complex (Figure 4.8B). In addition to its ability to disrupt the CDC25B-CDK2/Cyclin A protein-protein interaction, titration with CCG-17950 inhibited the dephosphorylation of pTpY-CDK2/Cyclin A by CDC25B in vitro (Figure 4.8C).
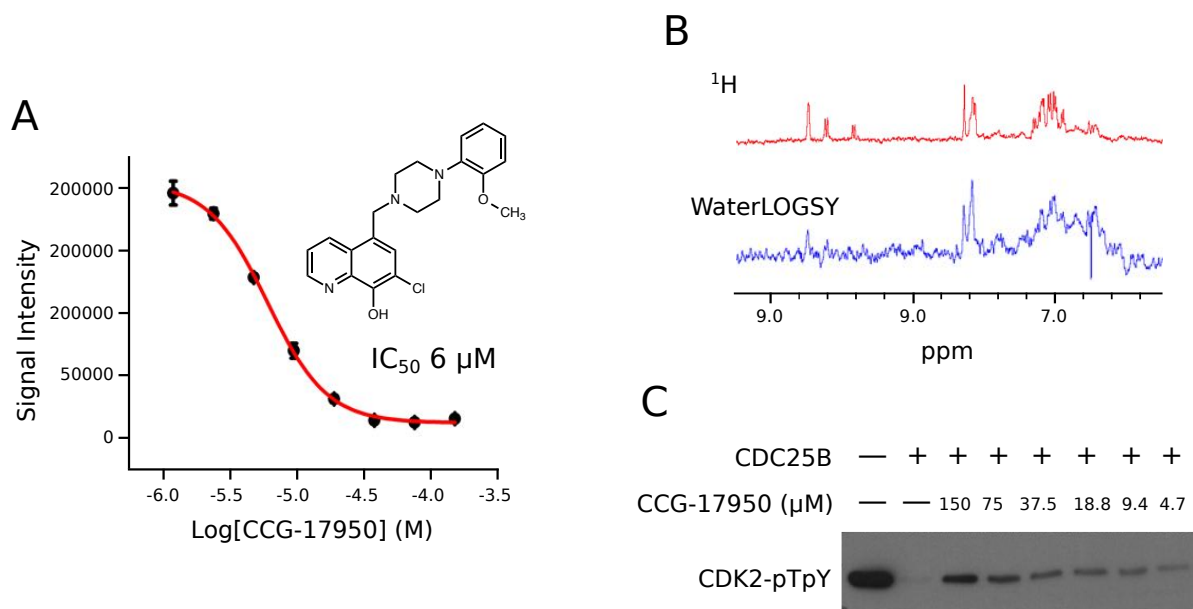
Figure 4.8. *CCG-17950 binds to CDK2/Cyclin A and inhibits its dephosphorylation in vitro.* A) Inhibition of the CDC25B-CDK2/Cyclin A PPI by CCG-17950 in an AlphaLISA experiment (structure inlaid). B) ^1H 1D NMR spectrum for CCG-17950 alone (red) or WaterLOGSY spectrum of CCG-17950 in the presence of CDK2/Cyclin A. C) *In vitro* phosphatase assay utilizing phosphorylated CDK2/Cyclin A as a substrate for CDC25B in the presence or absence of CCG-17950. Remaining phosphorylated CDK2/Cyclin A is detected by western blot.

Because CDC25B is highly overexpressed in pancreatic cancers, we tested the effect of CCG-17950 on the viability of pancreatic carcinoma cell line MIA PaCa-2. MIA PaCa-2 cell line expresses high levels of CDC25B and has been previously been shown to be sensitive to CDC25B inhibitors[23]. In a dose-dependent manner, MIA PaCa-2 cells showed slower growth upon treatment with CCG-17950, with greater than fifty percent growth inhibition at 25 μM (Figure 4.9A). We further examined the CDK2 phosphorylation status upon compound treatment in order to examine whether the reduction in cell growth was due to the inhibition of CDK2 dephosphorylation. CCG-17950-treated cells showed a marked inhibition of CDK2 dephosphorylation as compared to vehicle control (Figure 4.9B). The inhibition of CDK2 dephosphorylation by CCG-17950 closely resembled that of the CDK2 kinase inhibitor NU-6102, which arrests cells in G2 phase[24]. Analysis of the cell cycle upon treatment with CCG-17950 revealed a dose-dependent arrest in the S and G2 phases as compared to vehicle
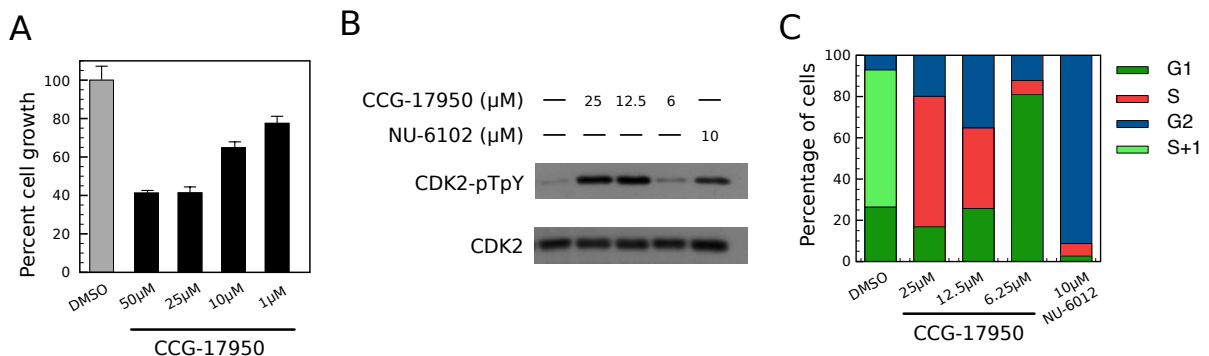
Figure 4.9. *CCG-17950 inhibits CDK2 dephosphorylation and causes cell cycle arrest in vivo.* A) MTT assay showing cell viability of MIA PaCa-2 cells in the presence of CCG-17950, normalized to DMSO control (gray). B) Western blot showing CDK2 phosphorylation in response to treatment with CCG-17950 in synchronized MIA PaCa-2 cells. The CDK2 kinase inhibitor NU-6102 is shown as a pseudo-positive control. C) Percentage cell distribution for different cell cycle phases in response to CCG-17950 treatment of synchronized MIA PaCa-2 cells. NU-6102 is shown as a pseudo-positive control.

controls (Figure 4.9C). These results indicate that CCG-17950 is an inhibitor of the CDC25B-CDK2/Cyclin A interaction in vitro and inhibits CDK2 dephosphorylation in cells, leading to cell cycle and growth arrest in pancreatic cancer cells.

4.5 HTS-2: Improvements upon the AlphaLISA assay and re-screening of a subset library

4.5.1 Redesigning the AlphaLISA assay

Two observations from HTS-1 prompted a redesign of the AlphaLISA assay. First, the very high hit rate of the HTS-1 assay severely limited our ability to follow up with potential hit compounds. Second, our characterization of validated hits from HTS-1 found that the inhibition of several compounds was lost upon the addition of ATP. Since ATP binds the active site of CDK2, we inferred that the loss of activity of these compounds was due either to competition with ATP for the active site, or to any structural changes associated with ATP binding.

We made several modifications to the AlphaLISA assay to address the high hit rate and the ATP sensitivity. First, we optimized the assay in the presence of ATP and Mg, which is
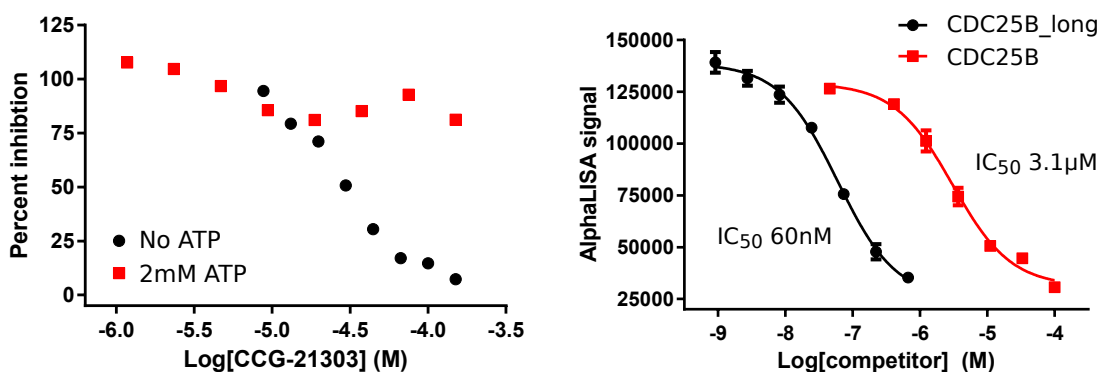
Figure 4.10. *AlphaLISA assay modifications for HTS-2.* Left: Inhibition in the AlphaLISA assay by CCG-21303 in the presence (red) and absence (black) of 2mM ATP. Right: Disruption of AlphaLISA signal upon titration with either the CDC25B catalytic domain (red) or CDC25B_long (black).

required for proper ATP binding[25]. At saturating concentrations of ATP•Mg, compounds showing ATP-dependent inhibition no longer had any effect in the assay (Figure 4.10). To attempt to reduce the hit rate, we decided to alter our CDC25B protein construct. Our initial CDC25B protein construct used for HTS-1 contained only the CDC25B catalytic domain, without the C-terminal unstructured region. Further analysis of the literature[26] and our own characterization of this region (see Chapter 2) revealed that several residues contribute to the CDC25B-CDK2/Cyclin A interaction. We hypothesized that by including this C-terminal region we might increase the affinity of the PPI and limit the number of compounds affecting our assay. We therefore redesigned our CDC25B construct to include the 9 remaining residues in the C-terminus of CDC25B (CDC25B_long-Flag). We also added a 5 residue gly-ser linker prior to the C-terminal Flag tag to separate the Flag tag from the C-terminal residues of CDC25B. In the redesigned AlphaLISA assay, titration with untagged CDC25B containing the additional C-terminal residues (CDC25B_long) showed a 50-fold increase in potency compared to the untagged construct used in HTS-1 (CDC25B), confirming that the inclusion of these residues significantly increases binding affinity (Figure 4.10).

Ultimately, the new AlphaLISA assay increased the S/N over 10-fold compared to the assay used in HTS-1. Testing of a single 384-well control plate using our new AlphaLISA assay under HTS conditions produced a S/N of 125, a CV of 6.9%, and a Z-factor of 0.79, indicating that the revised AlphaLISA assay was high quality.

4.5.2 Primary screening for HTS-2

Using our revised AlphaLISA assay, we screened a 20,000 compound subset of the UM-CCG library screened previously in HTS-1. As in HTS-1, we screened using a relatively high

compound concentration around 35 μM to allow for identification of low-potency inhibitors. The AlphaLISA assay performed well under high-throughput screening conditions with an average Z-factor of 0.70. Similarly to HTS-1, we observed a high hit rate of 29.6% for the primary screen, resulting in 5,918 hit compounds. Of these compounds, 1,500 were selected for advancement to the confirmation screening stage as described in Table 4.A2.

4.5.3 Confirmation screening for HTS-2

Confirmation screening was conducted with both the primary AlphaLISA assay as well as the control AlphaLISA counter screen as described in HTS-1. The 1500 compounds selected from the primary screening stage were tested in both assays in duplicate at 35 μM concentration (Figure 4.11). Of these compounds, the 246 that showed activity greater than 5% inhibition in the primary than in the counter screening assay were considered for further analysis. The 246 remaining compounds were inspected manually to cluster redundant compounds, and the top 120 compounds were selected for advancement to the dose-response stage.
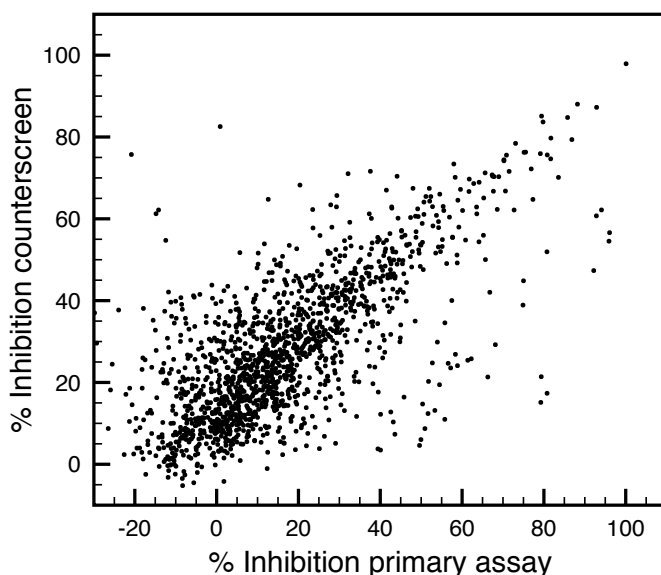
Figure 4.11. *HTS-2 confirmation screening results.* Hit selection from confirmation screening results is given in Appendix Table 4.A2.

4.5.4 Dose response and follow up for HTS-2

The 120 compounds selected for the dose response screening stage were tested in duplicate titration experiments using the HTS-2 primary assay. Compounds were titrated in an 8-point, 2-fold dilution series format starting at 150µM concentration. Of the 120 compounds tested, 23 compounds exhibiting dose-dependent inhibition with an IC_{50} greater than 50µM and were considered active inhibitors. Figure 4.12 gives a breakdown of HTS-2 results.

Of the 23 compounds identified as active in the dose response screening stage, six compounds were ordered from commercial sources. Four of the ordered compounds showed comparable activity to that determined during dose response screening, with IC_{50} between 5 and 15 µM (Table 4.2). One of these four inhibitors was the compound CCG-18861, which inhibited the CDC25B-CDK2/Cyclin A interaction with an IC_{50} of 15 µM (Figure 4.13)

Primary screen	20,000
Primary hits	5,918
Tested in confirmation	3,200
Tested in DR	120
Active in DR	23
Validated from fresh powder	4
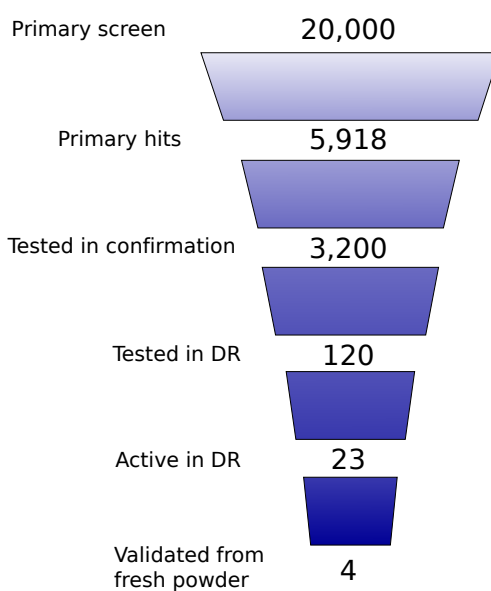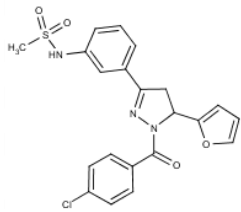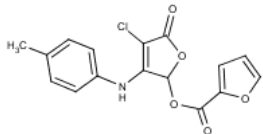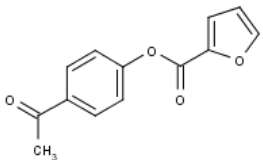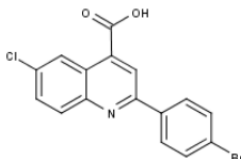
Figure 4.12. *Breakdown of HTS-2 results.*

Table 4.2. *Most potent hits validated from HTS-2.*

Name	Structure	Percent primary	Percent secondary	Percent counterscreen	IC50 DR (uM)	IC50 Fresh (uM)
CCG-28496		56.6	49.5	5.9	28.8	6.9
CCG-21280		41.1	52.9	13.0	49.0	7.2
CCG-20311		52.4	80.6	17.2	45.7	11.6
CCG-18861		87.9	79.0	15.0	13.8	14.9

4.5.5 Characterization of CCG-18861

We selected the compound CCG-18861, or 2-(4-bromophenyl)-6-chloroquinoline-4-carboxylic acid, for further characterization. Similar to the characterization of CCG-17950, we employed NMR to identify the target of CCG-18861. No chemical shift perturbations were observed on a $^{1}H^{15}N$-HSQC spectrum for CDC25B, but ligand-detected NMR experiments with CDK2/Cyclin A indicated that CCG-18861 binds to the CDK2/Cyclin A complex (Figure 4.13). To further understand the binding mode of this compound, we crystalized the CDK2/Cyclin A complex in
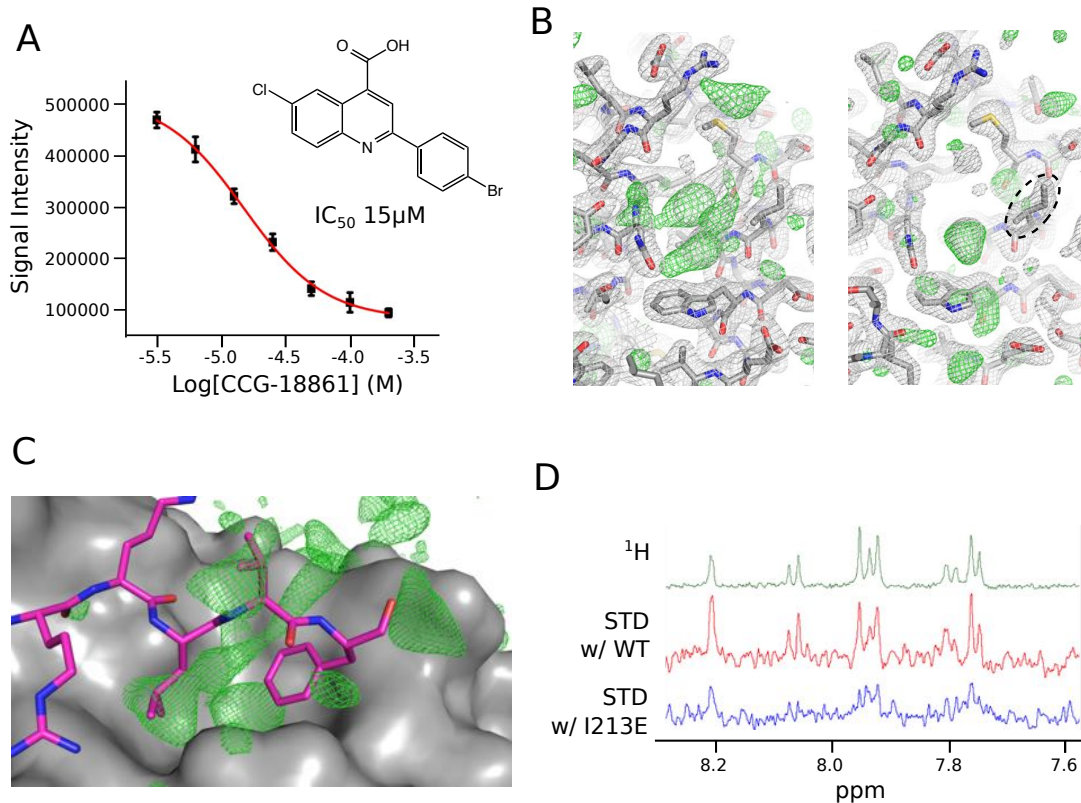
Figure 4.13. *CCG-18861 binds to the RxL motif on Cyclin A and inhibits CDC25B-CDK2/Cyclin A.* A) Inhibition of the CDC25B-CDK2/Cyclin A PPI by CCG-18861 in an AlphaLISA experiment (structure inlaid). B) Crystal structures in the presence (left) and absence (right) of CCG-18861. 2Fo-Fc density map cut at 1.0σ is shown as a gray mesh; Fo-Fc difference map cut at 2.5σ is shown as a green mesh. I213 is encircled with a dotted ellipse. C) ^{1}H 1D NMR spectra for CCG-18861 alone (green) and saturation transfer difference (STD) experiments in the presence of either wild-type CDK2/Cyclin A (red) or CDK2/Cyclin A complex with Cyclin A I213E mutation (blue).

the presence of CCG-18861 (Figure 4.13). Crystals soaked with compound reproducibly produced unaccounted for electron density in the RxL-binding pocket on Cyclin A, a site known to be important for substrate recognition of the CDK2/Cyclin A complex[27]. This site has also been hypothesized to interact with the CDC25B C-terminal tail[26]. Superimposition of the CCG-18861 Fo-Fc electron density map onto a crystal structure of CDK2/Cyclin A bound to a CDK2 substrate containing the RxL motif[28] shows that portions of the CCG-18861 density overlap with the
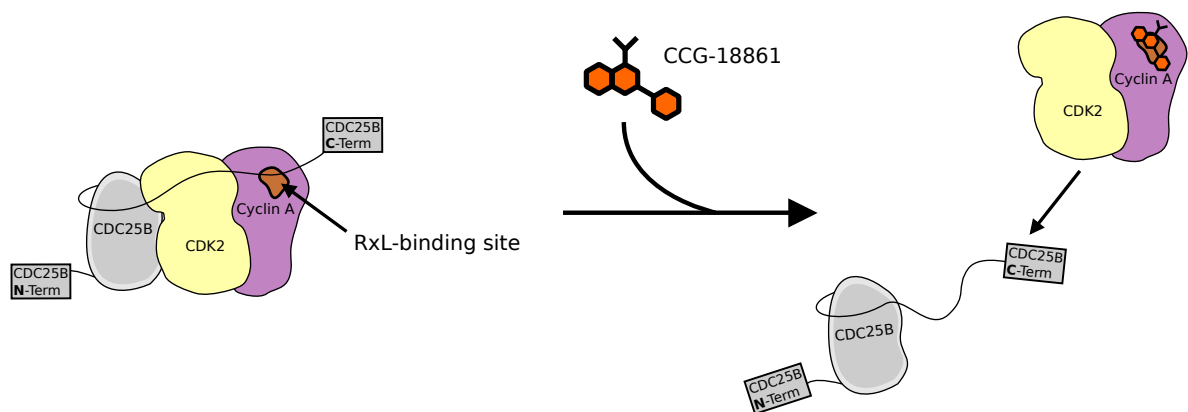
Figure 4.14. *Disruption of the CDC25B-CDK2/Cyclin A PPI by CCG-18861.* Model of the disruption of CDC25B-CDK2/Cyclin A by CCG-18861 competing with CDC25B for the RxL-binding motif.

peptide (Figure 4.13). Specifically, the electron density for CCG-18861 clearly overlaps the leucine of the RxL peptide, which has been previously demonstrated to be critical for the interaction between RxL-containing peptides and the Cyclin A binding pocket[29]. Although the observed electron density was not sufficiently well defined to accurately determine the structure of CCG-18861 in this site, we hypothesized that the inhibitory activity of CCG-18861 was due to competition for this site with CDC25B. To address this hypothesis, we mutated a key hydrophobic residue in this pocket to a glutamic acid (I213E). As indicated by STD NMR experiments, binding of CCG-18861 to the mutant complex was significantly reduced (Figure 4.13). To ensure this mutation did not affect the structure of the CDK2/Cyclin A complex, we determined the crystal structure of the mutant and found no significant changes between the mutant and the wild-type structures (not shown). Combined, these data indicates that CCG-18861 binds to the CDK2/Cyclin A complex in the RxL-binding pocket of Cyclin A and disrupts the PPI with CDC25B (Figure 4.14).

4.6 HTS-3: Optimization of an HTRF-based assay for high-throughput screening

4.6.1 Design of the HTRF assay

Due to the high hit rate from both HTS-1 and HTS-2 AlphaLISA-based screens, we decided a new, more robust assay was required. For this reason we developed the HTRF assay. Though the energy transfer in the HTRF assay requires 10-fold shorter distance between donor and acceptor when compared to the AlphaLISA, the HTRF assay has several advantages. Primarily, the europium cryptate donor has a long fluorescent lifetime in the range of µs-ms[30], compared to most fluorescent organic compounds that have fluorescent lifetimes in the nanosecond range[30]. By incorporating a delay between donor excitation and acceptor detection, the HTRF assay is less sensitive to fluorescent compounds.

As mentioned above, we tested both AlphaLISA and HTRF with our CDC25B-Flag and His-CDK2/Cyclin A constructs during HTS-1 optimization and observed signal for only the AlphaLISA assay. Because the HTRF requires shorter distance between donor and acceptor beads, this result indicated that the protein tag orientations used were sufficiently close for
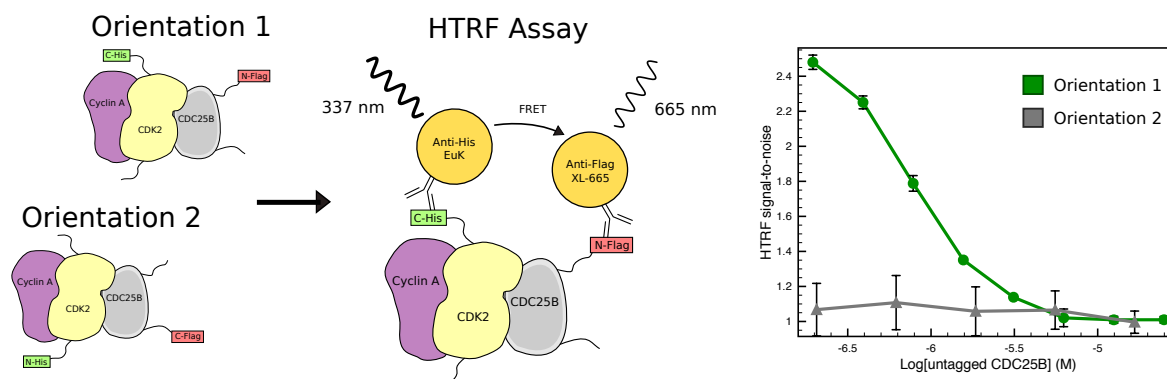
Figure 4.15. *Development of the HTRF-based high-throughput screening assay for CDC25B-CDK2/Cyclin A.* Left: schematic of the HTRF assay showing both tag orientations tested on the left, and the final assay configuration to the right. Right: Titration of untagged CDC25B_long competitor in HTRF assays for both tag configurations.
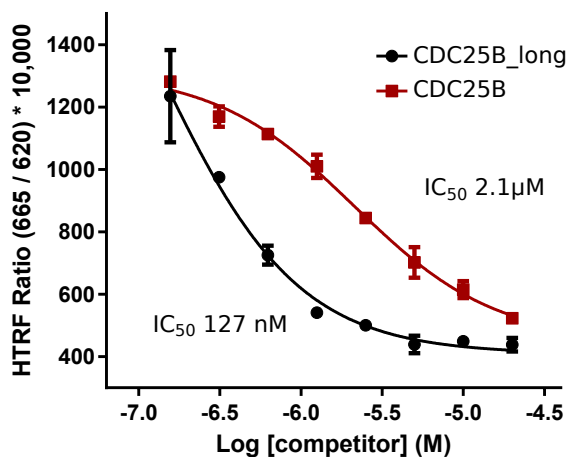
Figure 4.16. *Validation of the HTRF-based for assay high-throughput screening.* Left: disruption of HTRF signal upon titration with either CDC25B (red) or CDC25B_long (black). Right: pre-HTS assay statistics for the HTRF assay.

AlphaLISA, but not close enough for HTRF. Previously published computational models suggested that the N-terminus of CDC25B is close to the C-terminus of CDK2[31], and therefore we designed new protein constructs for use in the HTRF assay with an N-terminally Flag tagged CDC25B and a C-terminally 6xHis tagged CDK2 in complex with Cyclin A (Flag-CDC25B_long and CDK2-His/Cyclin A, Table 4.A1). Using these protein constructs we observed HTRF signal, demonstrating that the new protein tag orientations were sufficiently close for FRET to occur (Figure 4.15).

We titrated the HTRF assay with either untagged CDC25B or untagged CDC25B_long to ensure the HTRF assay was sensitive to disruption by protein competitors. Both of the competitors exhibited dose-dependent inhibition of the HTRF signal with IC_{50} of 2.1 μM and 128 nM for CDC25B and CDC25B_long respectively (Figure 4.16). After validation, the HTRF assay was tested under HTS conditions using a control plate as was done in HTS-1 and 2. With a S/N, CV, and Z-factor of 9.9, 6.9%, and 0.87 respectively, the HTRF assay was deemed a high-

quality assay with a similar performance to the AlphaLISA assays in HTS-1 and 2. In addition

to assessment using a control plate, we performed a small-scale screen of four plates from the

UM-CCG compound library to determine the hit rate for the HTRF assay. As the primary

problem with our first two HTS campaigns was the high hit rate, testing HTRF assay performance

with compounds was critical prior to large-scale screening. Importantly, the 3SD hit rate for this

small-scale screen was 2.5 %, a 7-fold reduction as compared to HTS-1 and a 12-fold reduction

as compared to HTS-2. Once the HTRF assay had demonstrated increased robustness, we

proceeded with large scale HTS.

4.6.2 Primary screening for HTS-3

The optimized HTRF assay was used to screen 103,780 compounds from the UM-CCG

compound library. To reduce the number of hits compared to HTS-1 and 2, we screened at a

slightly lower compound concentration of approximately 25 μM. The HTRF assay performed

well under high-throughput screening conditions as judged by the average Z-factor of 0.75. The

hit rate by 3SD for the entire screen was 0.9%, far lower than the 17.8% and 29.6% observed for
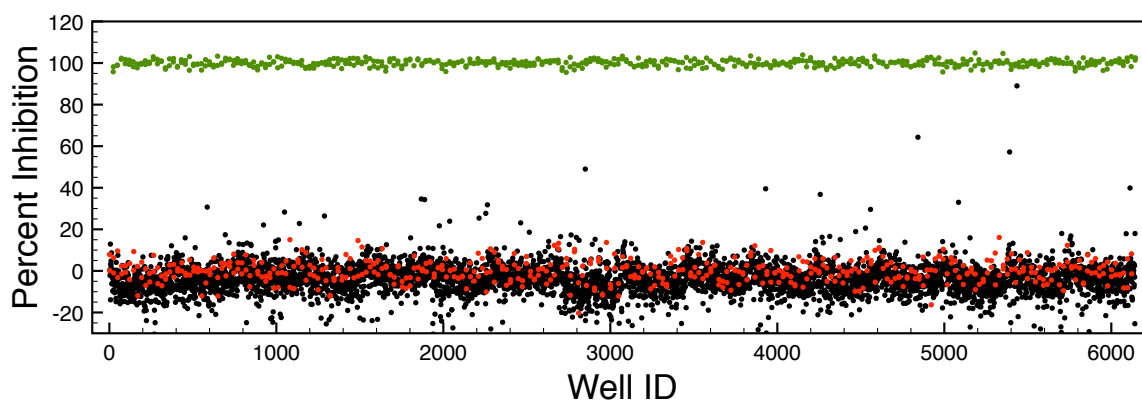
Figure 4.17. *HTS-3 performance*. High-throughput screening performance of 16 384-well plates (plate numbers 5318-5333) from a single day of screening. A scatter plot containing positive controls (green), negative controls (red), and compound wells (black) is shown.

HTS-1 and 2 respectively. A representative set of 16 plates from a single day of screening is shown in Figure 4.17. All 902 hits as defined by 3SD were selected for the confirmation screening stage. We additionally selected weaker hits with inhibition less than 3SD but greater than 12%, adding 598 more compounds for a total of 1,500.

4.6.3 Confirmation screening for HTS-3

Compounds selected for the confirmation screening stage were retested at the same 25μM concentration in triplicate in both the HTRF assay used in the primary screen and the AlphaLISA assay as used in HTS-2. Of the 1,500 compounds screened in the confirmation stage, 71 compounds showed inhibition greater than 3SD in both assays. Again, in order to further explore weaker compounds, we selected the top 49 compounds with inhibition less than 3SD but greater than 5% in both the HTRF and AlphaLISA assays. A total of 120 compounds from the confirmation screening were selected for progression to the dose-response screening stage. The bounded box in Figure 4.18 shows a visual representation of compound selection.
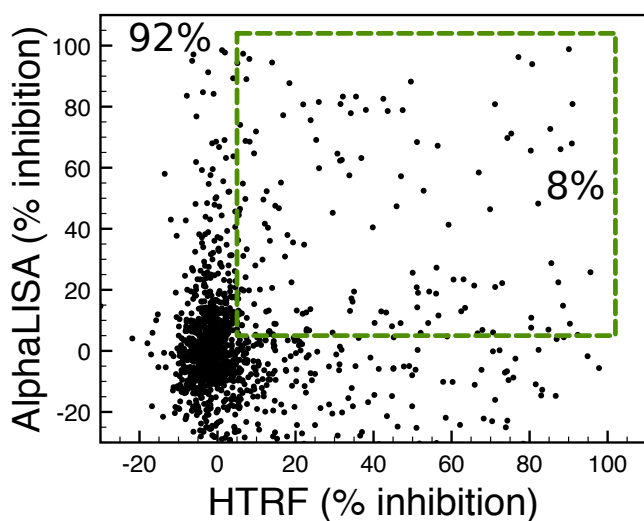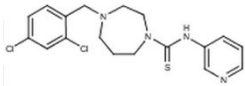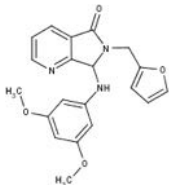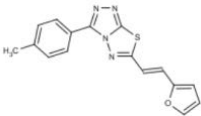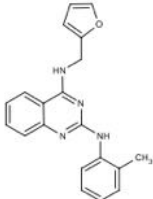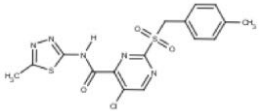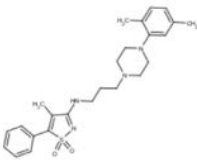
Figure 4.18. HTS-3 *confirmation screening results.* Scatter plot of the 1,500 compounds tested in confirmation screening. The green dotted box denotes the 150 compounds selected for dose-response experiments.

Table 4.3. *Most potent hits validated from HTS-3.*

Name	Structure	Percent primary	Percent secondary	Percent counterscreen	IC50 DR (uM)	IC50 Fresh (uM)
CCG-42172		47.3	56.1	27.3	11.0	2.0
CCG-30182		21.2	9.8	8.23	95.5	10.9
CCG-144491		47.2	18.7	22.5	20.0	44.6
CCG-111697		17.5	13.4	6.0	55.0	48.4
CCG-149631		32.2	14.0	20.6	>150	65.4
CCG-159120		53.7	54.3	19.4	20.9	69.0

4.6.4 Dose response and follow up for HTS-3

For the final dose-response stage, the 120 compounds selected from the confirmation screening were tested in duplicate with a starting concentration of 150μM followed by an 8-point, 2-fold dilution series. 46 compounds exhibiting greater than 50% inhibition at 150 μM were considered to be active hits for further study. A breakdown of HTS-3 is shown in Figure 4.19.

Of the 46 compounds considered active from HTS-3, 28 were ordered from commercial sources for retesting. Six of the ordered compounds had a similar or increased potency compared to their activity in the dose-response experiments using compound from the original screening library. These validated hits ranged from 2μM to 70μM in potency (Table 4.3). The two most potent compounds identified were CCG-42172 and CCG-30182, with IC_{50} of 2.0 μM and 10.9 μM respectively.

Primary screen — 20,000
Primary hits — 5,918
Tested in confirmation — 3,200
Tested in DR — 120
Active in DR — 23
Validated from fresh powder — 4
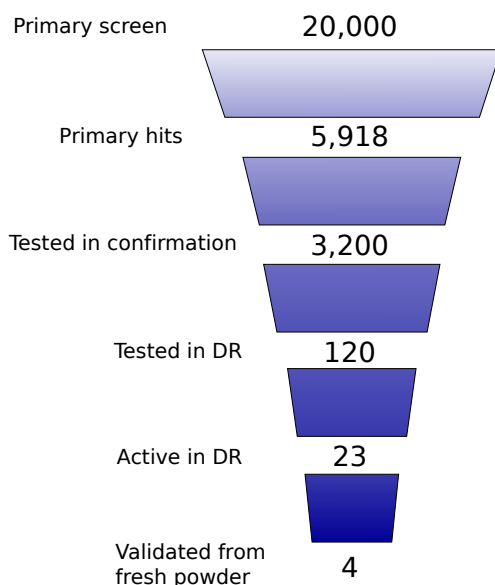
Figure 4.19. *Breakdown of HTS-3 results.*

4.6.5 Characterization of HTS-3 hits: CCG-42172 and CCG-30182

The most potent of the hits validated from HTS-3 was 4-(2,4-dichlorobenzyl)-N-(pyridin-3-yl)-1,4-diazepane-1-carbothioamide, or CCG-42172. Freshly dissolved CCG-42172 from commercial sources disrupted the CDC25B-CDK2/Cyclin A PPI with an IC_{50} of 2.0 μM (Figure 4.20). The freshly prepared commercially acquired compound was more than 20-fold more potent as compared to compound from the UM-CCG screening library, indicating that CCG-42172 might have undergone degradation or precipitation in the compound library over time. NMR experiments with this compound show that CCG-42172 does not interact with CDC25B, but interacts with the CDK2/Cyclin A complex (Figure 4.21).

The second most potent compound identified from HTS-3 was CCG-30182 (7-((3,5-dimethoxyphenyl)amino)-6-(furan-2-ylmethyl)-6,7-dihydro-5H-pyrrolo[3,4-b]pyridin-5-one). CCG-30182 inhibited the CDC25B-CDK2/Cyclin A PPI with a 10.9 μM IC_{50} when prepared from fresh powder (Figure 4.20). The limited inhibition by CCG-30182 in both the
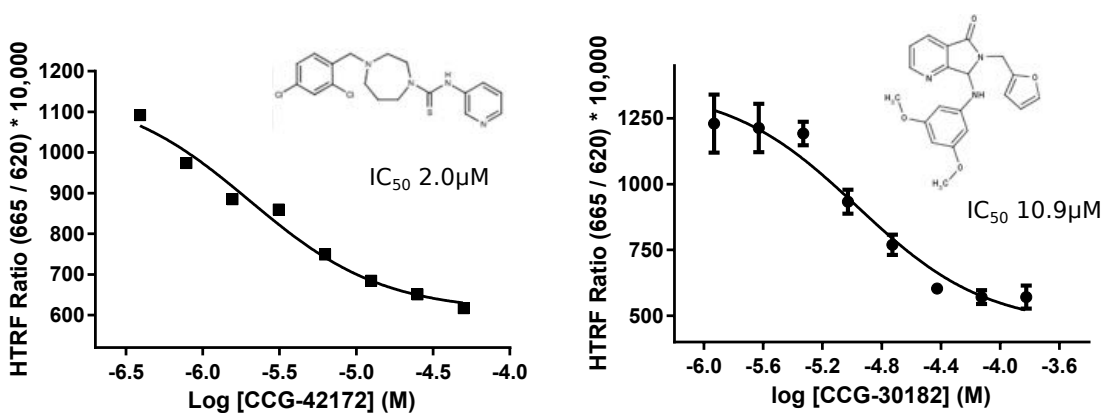
Figure 4.20. *Validated hits CCG-42172 and CCG-30182 identified in the HTRF-based high-throughput screen.* Left: inhibition of the CDC25B-CDK2/Cyclin A PPI by CCG-42172 in a HTRF experiment (structure inlaid). Right: inhibition of the CDC25B-CDK2/Cyclin A PPI by CCG-30182 (structure inlaid) in an HTRF experiment. IC_{50}s are given for both compounds.
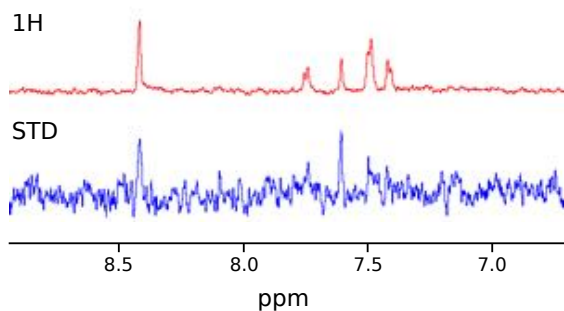
Figure 4.21. *CCG-42172 binds to CDK2/ Cyclin A.* ^{1}H 1D NMR spectra for CCG-42172 alone (red) and saturation transfer difference (STD) experiments in the presence of CDK2/ Cyclin A (blue).

primary and confirmation screens indicated that it was a relatively weak hit under the 25 μM screening concentrations. The 95.5 μM IC_{50} derived from the dose-response experiments also demonstrated that this compound was a relatively weak inhibitor; however, freshly ordered was more than 8-fold more potent. CCG-30182 was also tested by NMR for binding to CDC25B or CDK2/Cyclin A. The [1]H[15]N-HSQC experiment demonstrated no binding to CDC25B and we did not observe binding to CDK2/Cyclin A in 1D STD. Of note, one limitation of the STD experiment is a need for a relatively fast dissociation rate, and therefore this experiment may not be suitable to validate binding of more potent ligands. More extensive characterization of CCG-30182 is needed in order to confirm its mechanism of action.

4.7 Discussion

Here, we describe our efforts to develop a high-quality "gray box" screening assay for identifying inhibitors of the CDC25B-CDK2/Cyclin A PPI. This entailed the development and optimization of three separate screening assays. We initially tested both AlphaLISA and HTRF-based assays for the quantification of the CDC25B-CDK2/Cyclin A PPI. The AlphaLISA assay initially proved to be more straightforward to develop, since no HTRF signal was observed using the

original protein constructs. As judged by the statistics of pre-HTS control experiments, the AlphaLISA assay was highly suitable for HTS. And though the assay itself performed well during HTS-1 with an average Z-factor of 0.8, the utility of the AlphaLISA was limited by a very high hit rate under compound screening conditions. The high hit rate of 17.8% in HTS-1 resulted in a large number of hits (Figure 4.22), which required time consuming statistical and manual analysis to select compounds for confirmation screening.

We attempted to reduce the hit rate by increasing the robustness of the AlphaLISA assay. The extension of the CDC25B C-terminus to enhance affinity to CDK2/CyclinA and the inclusion of ATP in this assay resulted in over a 10-fold increase in S/N as compared to the assay used in HTS-1. Similarly to the HTS-1 assay, the HTS-2 AlphaLISA was of high quality for use in HTS as determined in our pre-HTS control experiments. We employed the HTS-2 assay to screen a subset of the compound library including 20,000 compounds. Similar to HTS-1, the new AlphaLISA assay performed well under screening conditions with a Z-factor of 0.70, but the 29.6% hit rate indicated that the new assay was still highly susceptible to interference (Figure 4.22).
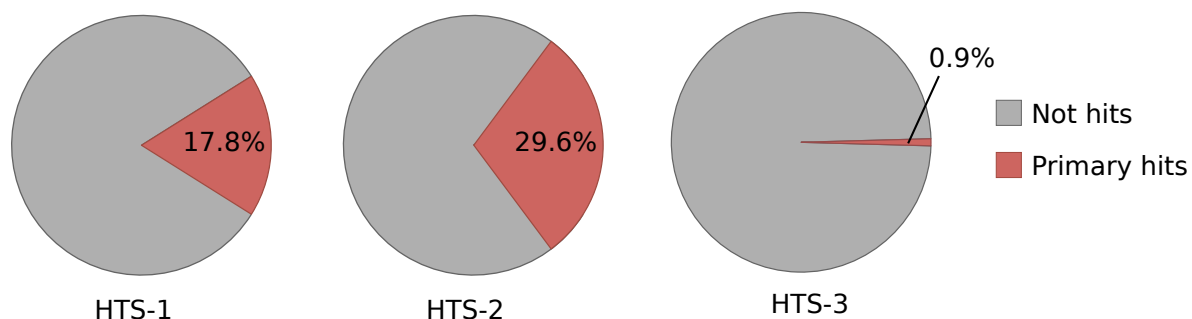
Figure 4.22. *Comparison of the hit rate between HTS-1, HTS-2, and HTS-3.* Pie chart of the hit rate from the primary screening campaigns for HTS-1, 2, and 3. Hits are defined as compounds with inhibition greater than 3 standard deviations compared to plate negative controls.

In order to address the high hit rate in our first two screens, we revisited the HTRF assay. Optimization of the HTRF assay for HTS-3 was comparatively more extensive due to required protein construct redesigns. The HTRF assay we developed proved to be of high quality as determined in our pre-HTS control experiments. In addition to the use of an entirely different assay, we reduced the compound concentration by 30% in order to limit compound interference. Interestingly, the performance of the HTRF assay during HTS was nearly identical to that of the first two screens, as judged by its Z-factor of 0.75. However, the 0.9% hit rate indicated that this assay was much more robust for compound screening and less susceptible to false positives (Figure 4.22). The increased robustness of this assay allowed us to screen a relatively large library, including over 100,000 compounds. Importantly, the low hit rate of the HTRF assay allowed for more thorough follow up studies of HTS hits.

Through our three high-throughput screening campaigns we identified and characterized several hit compounds: CCG-17950, CCG-18861, CCG-42172, and CCG-30182. The first compound identified, CCG-17950, inhibits the CDC25B-CDK2/Cyclin A interaction in vitro with an IC_{50} of 6 μM by binding to the CDK2/Cyclin A complex. This compound also inhibits CDK2 dephosphorylation by CDC25B in vitro and in pancreatic cancer cells. Inhibition of CDK2 dephosphorylation by CCG-17950 in these cells led to cell cycle arrest and cell growth inhibition. The second hit compound, CCG-18861, also inhibits the CDC25B-CDK2/Cyclin A interaction in vitro by binding to CDK2/Cyclin A, with an IC_{50} of 15 μM. Structural and mutagenesis studies have indicated that CCG-18861 binds to the RxL-binding motif on Cyclin A, likely disrupting the interaction with the CDC25B C-terminal tail. The third validated hit, CCG-42172, inhibited the CDC25B-CDK2/Cyclin A interaction with an IC_{50} of 2 μM. NMR experiments indicated that this compound also binds to the CDK2/Cyclin A complex. The final hit identified was

CCG-30182, which inhibited the CDC25B-CDK2/Cyclin A interaction with an IC_{50} of 11 μM. However, its mechanism of action remains unclear.

In summary, we have developed a high quality HTRF assay for CDC25B-CDK2/Cyclin A interaction that is both robust and sensitive, and highly suitable for screening large compound libraries. Furthermore, the HTRF assay represents an example of a high quality "gray box" assay which overcomes number of limitations of previously reported attempts to identify inhibitors of CDC25 phosphatases. Despite the fact that we identified several small molecule inhibitors blocking CDC25B-CDK2/Cyclin A interaction, we have not found any compounds that directly bind CDC25B. Identification of PPI inhibitors is challenging, in part due to lack of high quality compound libraries optimized for targeting PPI interfaces[32,33]. The HTRF assay we developed could be employed to screen more suitable focused libraries to identify inhibitors of CDC25B.

4.8 Experimental procedures

Expression and purification of recombinant CDC25B and CDK2/Cyclin A

All CDC25B and CDK2/Cyclin A proteins and their variants were expressed as described in Chapters 1 and 2.

AlphaLISA HTS assays and the AlphaLISA counter screen

C-terminally 6xHis tagged CDK2/Cyclin A complex and N-terminally Flag tagged CDC25B C473S (either 372-557 for the first HTS, or 372-566 for the rescreen) were expressed and purified as stated above. Proteins were incubated together at a final concentration of 300 nM each for 1 hr prior to incubation with compound for 1 hr, followed by addition of Ni-chelate AlphaScreen donor beads (Perkin-Elmer) and Anti-Flag AlphaLISA acceptor beads (Perkin-Elmer) at a final

concentration of 3 μg/mL for 1 hr. Assay reagents were dispensed using a multidrop liquid dispenser (Thermo Scientific) onto uncoated, white, low-volume, 384-well plates (Corning). Assay plates were quantified using an Envision plate reader (Perkin-Elmer) with excitation at 680 nm wavelength and emission at 615 nm in 9 μL volumes. Assays were performed in a buffer containing 50 mM MOPS (pH 7.25), 50 mM NaCl, 1mM TCEP, with addition of 0.01% BSA, and 0.01% Tween-20 immediately prior to the start of the assay.

The AlphaLISA assay used in HTS-2 was as described above except for the following alterations. Final protein concentrations were 75nM each, and final Alpha reagent concentrations were 0.5 μg/mL each. Assay volumes were 18 μL. The buffer described above for HTS-1 was supplemented with 10mM $MgCl_2$ and 1mM ATP.

The AlphaLISA counter screening assays for both HTS-1 and 2 were performed as in the HTS-1 and 2 primary assays without the CDK2/Cyclin A protein complex, and instead with a His-GST-CDC25B-Flag protein.

Compound similarity clustering

Compounds were clustered by first splitting structures into Daylight-based substructure fingerprints[34]. Compound daylight fingerprints were the compared using a variation of the Tanimoto coefficient to calculate similarity[35]. Compounds with a Tanimoto coefficient greater than 0.65 were clustered.

HTRF HTS assay

C-terminally 6xHis tagged CDK2/Cyclin A complex and N-terminally Flag tagged CDC25B C473S (372-566) were expressed and purified as stated above. Proteins were incubated together

117

at a final concentration of 125 nM each for 1 hr prior to incubation with compound for 1 hr, followed by addition of anti-6xHis europium cryptate donor beads (Cisbio) and anti-Flag XL-665 acceptor beads (Cisbio) at a final dilution of 1:350 for 1 hr. 20mM potassium fluoride was added 10 minute prior to plate reading. Assay reagents were dispensed using a multidrop liquid dispenser (Thermo Scientific) onto uncoated, black, low-volume, 384-well plates (Corning). Assay plates were quantified using an Envision plate reader (Perkin-Elmer) with excitation of the europium crytate donor at 337 nm wavelength and emission of the donor at 620 nm and emission of the XL-665 acceptor at 665 nm in 18 uL volumes. Assays were performed in a buffer containing 50 mM Tris (pH 7.5), 50 mM NaCl, 10mM $MgCl_2$, 1mM TCEP, with addition of and 1mM ATP, 0.05% BSA, and 0.05% Tween-20 immediately prior to the start of the assay.

Compound libraries screened

The compounds tested for all high-throughput screening was from the library of the University of Michigan Center for Chemical Genomics, and was comprised of a commercially available subset of compounds from ChemDiv, Maybridge HitFinder, and Chembridge screening libraries.

Ligand-detected NMR experiments

Samples for saturation transfer difference (STD) experiments were made with 2 μM CDK2/ Cyclin A or the CDK2/Cyclin A I213E mutant in 50 mM Tris (pH 8.0), 150 mM NaCl, 1 mM β-mercaptoethanol, and 5% D_2O. Compounds were tested at final concentrations of 150 μM in 5% DMSO. STD experiments used 2 s irradiation using a train of 50 ms Gaussian pulses centered

at 0 ppm using a previously described pulse sequence[36].

Samples for WaterLOGSY experiments were prepared as above with 2 μM CDK2/ Cyclin A and 150 μM compound. Pulse sequences used for WaterLOGSY experiments were as previously described[37]. Water was inverted using a 10 ms Gaussian pulse followed by a 1.5 s mixing time and a relaxation delay of 2 s. All spectra were acquired at 25 °C on a 600MHz Bruker Avance III spectrometer equipped with cryoprobe, running Topspin version 2.1.

Crystallization and structure determination CDK2/Cyclin A with CCG-18861

Crystals of apo-CDK2/Cyclin A were produced as previously published[25]. After formation, crystals were transferred to the mother liquor solution to containing either 5% DMSO control or 2 mM CCG-18861 in 5% DMSO and soaked for 4.5 hours and were then transferred to the mother liquor solution containing 5% DMSO control or 2 mM CCG-18861 in 5% DMSO, and 20% glycerol for cryoprotection prior to freezing in liquid nitrogen. Diffraction data was collected at the 21-ID-G beamline for the CCG-18861 complex and the 21-ID-D beamline for the DMSO control at the Life Sciences Collaborative Access Team at the Advanced Photon Source. The data was integrated and scaled using Mosflm[38] and the structures were solved by molecular replacement with MOLREP[39] using the known apo-CDK2/Cyclin A structure for the search model (PDB code: 4I3Z)[40]. Refinement for both structures was performed using REFMAC[41], COOT[42], and the CCP4 program suite[43] (Table 4.A3). The structure was validated using the MOLPROBITY[44] server.

In vitro CDC25B phosphatase activity assay

Western blot in vitro phosphatase activity assay was performed as described in Chapter 3.

Cell culture and reagents

Human pancreatic carcinoma cell line MIA PaCa-2, were a generous gift from Dr. Mats Ljungman. Cells were cultured in DMEM and supplemented with 10% fetal bovine serum and 1% antibiotics in a 5% CO_2 humidified incubator at 37 °C.

MTT Assay

For cell viability experiments, 2.5 10^3 MIA PaCa-2 cells suspended in 100 μL growth media were plated in quadruplicate on tissue culture treated clear, flat bottomed, cell culture-treated 96-well plates. After 16 hours, media was aspirated and replaced by media containing either vehicle control (0.25% DMSO) or compound (0.25% final DMSO concentration) and incubated for 72 hours. MTT labeling was done using the Vybrant MTT Cell Proliferation Assay Kit and absorbance at 570 nm was read using a PheraStar plate reader.

Immunoblotting

MIA PaCa-2 cells for immunoblotting experiments were plated in a 6-well cell culture-treated plate (2mL/well at 50,000 cells/mL) and synchronized at the G_1/S phase transition using a double thymidine block with two 17 hour 2 mM thymidine treatments and 9 hours between treatments. Immediately after release of the block, cells were treated with either 0.25% DMSO control or compound (0.25% final DMSO concentration) for 16 hours, followed by lysis with BC300 buffer (20mM Tris (pH8.0), 300mM KCl, 1mM EDTA, 200 μM Na_3VO_4, 10% glycerol and 0.1% NP-40 added fresh prior to lysis). Samples were separated on a 4-20% SDS-PAGE gel 170 volts for 45 minutes. Proteins were transferred to nitrocellulose with a wet electrotransfer system (BioRad) for 60 min at 25 volts. Following transfer, the membrane was blocked with 5% BSA

in Tris-buffered saline with 0.1% Tween-20 (TBS-T), and incubated overnight at 4 °C with anti-pT15-cdc2 monoclonal antibody (#9111, Cell Signaling Technology, 1:2000). After washing, the membrane was incubated with an HRP conjugated anti-rabbit antibody (1:10,000) and visualized using enhanced chemiluminescence. Blots were then stripped and reblotted for total CDK2 with an anti-cdk2 polyclonal antibody (sc-163, Santa Cruz Biotechnology, 1:5000) followed by secondary antibody incubation and visualization as above.

Cell cycle analysis

For cell cycle analysis experiments, 2 mL MIA PaCa-2 cells (5.0×10^4 cells/mL) were plated on a 6-well culture treated plate and synchronized as described above. Cells were treated with 0.25% DMSO control or compound in 0.25% DMSO for 16 hours. Each sample was trypsinized, washed with PBS, and fixed in 70% ethanol. Samples were then treated with RNaseA and stained with propidium iodide. 30,000 events were collected using a BD LSR II flow cytometer (BD Biosciences), and analysis of the cell cycle distribution was performed using the BD FACSDiva software (BD Biosciences).

4.9 Appendices

Appendix Table 4.A1. Protein constructs used for high-throughput screening.

Construct name	N-terminal tag	Protein	C-terminal tag
HTS-1			
CDC25B-Flag	--	CDC25B (372-557)	Flag
His-CDK2/Cyclin A	6xHis	CDK2 (1-296)/ Cyclin A (173-432)	--
His-CDC25B-Flag	6xHis	CDC25B (372-557)	Flag
HTS-2			
CDC25B_long-Flag	--	CDC25B (372-566)	Flag
His-CDK2/Cyclin A	6xHis	CDK2 (1-296)/ Cyclin A (173-432)	--
His-CDC25B_long-Flag	6xHis	CDC25B (372-566)	Flag
HTS-3			
Flag-CDC25B_long	Flag	CDC25B (372-566)	--
CDK2-His/Cyclin A	--	CDK2 (1-296)/ Cyclin A (173-432)	6xHis

Appendix Table 4.A2. *Hit selection process for HTS-2 confirmation screening.* Hits from the HTS-2 primary screen were selected by the categories shown below. Compounds were were selected for confirmation screening based on 4 factors: their percent inhibition in HTS-1, their percent inhibition in HTS-2, the difference in percent inhibition between HTS-1 and HTS-2, and the molecular weight of the compound. Group 1 represents hits that were inactive in HTS-1 but active in HTS-2. Group 2 contains hits that were highly active in HTS-1 and also active in HTS-2. Group 3 contains hits that were active in both HTS-1 and HTS-2, but were at least 10% more active in HTS-2. Group 4 contains hits that were not hits in HTS-1 and were weak in HTS-2, but were of low molecular weight.

Group	HTS-1 (%)	HTS-2 (%)	HTS-1 – HTS-2 (%)	Molecular weight (g/mol)	Number of compounds selected
1	< 30	> 30	> 5	--	739
2	> 75	> 30	--	--	9
3	> 30	> 30	> 10	--	47
4	--	15 – 30	> 5	< 350	605

Appendix Table 4.A3. *Crystallographic data collection and refinement statistics.*

PDB code	CDK2/Cyclin A w/ CCG-18861	CDK2/Cyclin A w/ DMSO
Data collection		
Space group	*C 2 2 2$_1$*	*P 1 2$_1$ 1*
Cell dimensions		
a, b, c (Å)	72.3, 146.0, 163.3	70.0, 163.4, 73.1
Resolution (Å)	2.60 (2.64-2.60)	2.20 (2.25-2.20)
Unique reflections	27138 (1332)	77430 (4565)
R_{sym}	0.427 (0.068)	0.684 (0.109)
$I / \sigma I$	13.3 (2.3)	15.4 (2.8)
Completeness (%)	99.8 (99.3)	98.4 (87.5)
Redundancy	6.2 (5.2)	3.7 (3.3)
Refinement		
R_{work} / R_{free} (%)	20.7 / 25.0	21.3 / 25.1
No. atoms		
Protein	4427	8894
Water	0	0
Mean B-factors (Å^2)	34.17	37.8
R.m.s. deviations		
Bond lengths (Å)	0.008	0.019
Bond angles (°)	1.144	0.919
Ramachandran plot		
Most favored regions (%)	95.4	97.1
Additional allowed regions (%)	4.05	2.26

4.10 References

1. Johnston, P. A. *et al.* Cdc25B dual-specificity phosphatase inhibitors identified in a high-throughput screen of the NIH compound library. *Assay Drug Dev. Technol.* **7,** 250–65 (2009).

2. Kim, K.-R. *et al.* EK-6136 (3-methyl-4-(O-methyl-oximino)-1-phenylpyrazolin-5-one): a novel Cdc25B inhibitor with antiproliferative activity. *Eur. J. Pharmacol.* **528,** 37–42 (2005).

3. Feng, X. *et al.* Discovery and characterization of a novel inhibitor of CDC25B, LGH00045. *Acta Pharmacol. Sin.* **29,** 1268–74 (2008).

4. Lazo, J. S. *et al.* Identification of a potent and selective pharmacophore for Cdc25 dual specificity phosphatase inhibitors. *Mol. Pharmacol.* **61,** 720–8 (2002).

5. Lavecchia, A., Di Giovanni, C. & Novellino, E. Inhibitors of Cdc25 phosphatases as anticancer agents: a patent review. *Expert Opin. Ther. Pat.* **20,** 405–25 (2010).

6. Kristjánsdóttir, K. & Rudolph, J. Cdc25 phosphatases and cancer. *Chem. Biol.* **11,** 1043–1051 (2004).

7. Brisson, M. *et al.* Redox regulation of Cdc25B by cell-active quinolinediones. *Mol. Pharmacol.* **68,** 1810–20 (2005).

8. Cossy, J. *et al.* Biological evaluation of newly synthesized quinoline-5,8-quinones as Cdc25B inhibitors. *Bioorg. Med. Chem.* **14,** 6283–7 (2006).

9. Brisson, M. *et al.* Independent mechanistic inhibition of cdc25 phosphatases by a natural product caulibugulone. *Mol. Pharmacol.* **71,** 184–92 (2007).

10. Zhou, Y. *et al.* LGH00031, a novel ortho-quinonoid inhibitor of cell division cycle 25B, inhibits human cancer cells via ROS generation. *Acta Pharmacol. Sin.* **30,** 1359–68 (2009).

11. Waris, G. & Ahsan, H. Reactive oxygen species: role in the development of cancer and various chronic conditions. *J. Carcinog.* **5,** 14 (2006).

12. Rudolph, J., Epstein, D., Parker, L. & Eckstein, J. Specificity of natural and artificial substrates for human Cdc25A. *Anal. Biochem.* **289,** 43–51 (2001).

13. Chang, L. *et al.* Chemical screens against a reconstituted multiprotein complex: myricetin blocks DnaJ regulation of DnaK through an allosteric mechanism. *Chem. Biol.* **18,** 210–21 (2011).

14. Wong, V. Biology in a gray box: targeting the emergent properties of protein complexes: 2011 Yale Chemical Biology Symposium. *Yale J. Biol. Med.* **84,** 491–5 (2011).

15. Al-Mawsawi, L. Q., Christ, F., Dayam, R., Debyser, Z. & Neamati, N. Inhibitory profile of a LEDGF/p75 peptide against HIV-1 integrase: insight into integrase-DNA complex formation and catalysis. *FEBS Lett.* **582,** 1425–30 (2008).

16. Szekeres, P. G., Leong, K., Day, T. A., Kingston, A. E. & Karran, E. H. Development

of homogeneous 384-well high-throughput screening assays for Abeta1-40 and Abeta1-42 using AlphaScreen technology. *J. Biomol. Screen.* **13,** 101–11 (2008).

17. Rees, M. G. *et al.* A panel of diverse assays to interrogate the interaction between glucokinase and glucokinase regulatory protein, two vital proteins in human disease. *PLoS One* **9,** e89335 (2014).

18. Bielefeld-Sevigny, M. AlphaLISA immunoassay platform- the 'no-wash' high-throughput alternative to ELISA. *Assay Drug Dev. Technol.* **7,** 90–92 (2009).

19. Degorce, F. *et al.* HTRF: A technology tailored for drug discovery - a review of theoretical aspects and recent applications. *Curr. Chem. Genomics* **3,** 22–32 (2009).

20. Bazin, H., Trinquet, E. & Mathis, G. Time resolved amplification of cryptate emission: A versatile technology to trace biomolecular interactions. *Rev. Mol. Biotechnol.* **82,** 233–250 (2002).

21. Reed, G. F., Lynn, F. & Meade, B. D. Use of coefficient of variation in assessing variability of quantitative assays. *Clin. Diagn. Lab. Immunol.* **9,** 1235–9 (2002).

22. Zhang, J.-H. A Simple Statistical Parameter for Use in Evaluation and Validation of High Throughput Screening Assays. *J. Biomol. Screen.* **4,** 67–73 (1999).

23. Guo, J. *et al.* Expression and functional significance of CDC25B in human pancreatic ductal adenocarcinoma. *Oncogene* **23,** 71–81 (2004).

24. Thomas, H. D. *et al.* Preclinical in vitro and in vivo evaluation of the potent and specific cyclin-dependent kinase 2 inhibitor NU6102 and a water soluble prodrug NU6301. *Eur. J. Cancer* **47,** 2052–9 (2011).

25. Bao, Z. Q., Jacobsen, D. M. & Young, M. A. Briefly bound to activate: transient binding of a second catalytic magnesium activates the structure and dynamics of CDK2 kinase for catalysis. *Structure* **19,** 675–90 (2011).

26. Wilborn, M., Free, S., Ban, A. & Rudolph, J. The C-terminal tail of the dual-specificity Cdc25B phosphatase mediates modular substrate recognition. *Biochemistry* **40,** 14200–14206 (2001).

27. Brown, N. R., Noble, M. E., Endicott, J. a & Johnson, L. N. The structural basis for specificity of substrate and recruitment peptides for cyclin-dependent kinases. *Nat. Cell Biol.* **1,** 438–443 (1999).

28. Cheng, K.-Y. *et al.* The role of the phospho-CDK2/cyclin A recruitment site in substrate recognition. *J. Biol. Chem.* **281,** 23167–79 (2006).

29. Wohlschlegel, J. A., Dwyer, B. T., Takeda, D. Y. & Dutta, A. Mutational analysis of the Cy motif from p21 reveals sequence degeneracy and specificity for different cyclin-dependent kinases. *Mol. Cell. Biol.* **21,** 4868–74 (2001).

30. Berezin, M. Y. & Achilefu, S. Fluorescence lifetime measurements and biological imaging. *Chem. Rev.* **110,** 2641–84 (2010).

31. Sohn, J., Parks, J. & Buhrman, G. Experimental validation of the docking orientation of Cdc25 with its Cdk2-CycA protein substrate. *Biochemistry* **44,** 16563–16573

(2005).

32.   Sperandio, O., Reynès, C. H., Camproux, A.-C. & Villoutreix, B. O. Rationalizing the
chemical space of protein-protein interaction inhibitors. *Drug Discov. Today* **15,** 220–
9 (2010).

33.   Pagliaro, L. *et al.* Emerging classes of protein-protein interaction inhibitors and new
tools for their development. *Curr. Opin. Chem. Biol.* **8,** 442–9 (2004).

34.   Daylight Chemical Information Systems. *Daylight Theory Manual. Int. Immunol.* **25,**
(2013).

35.   Willett, P., Barnard, J. M. & Downs, G. M. Chemical Similarity Searching. *J. Chem.
Inf. Model.* **38,** 983–996 (1998).

36.   Mayer, M. & Meyer, B. Group epitope mapping by saturation transfer difference
NMR to identify segments of a ligand in direct contact with a protein receptor. *J. Am.
Chem. Soc.* **123,** 6108–17 (2001).

37.   Dalvit, C., Fogliatto, G., Stewart, A., Veronesi, M. & Stockman, B. WaterLOGSY as
a method for primary NMR screening: practical aspects and range of applicability. *J.
Biomol. NMR* **21,** 349–59 (2001).

38.   *Evolving Methods for Macromolecular Crystallography*. **245,** (Springer Netherlands,
2007).

39.   Vagin, A. & Teplyakov, A. Molecular replacement with MOLREP. *Acta Crystallogr.
D. Biol. Crystallogr.* **66,** 22–5 (2010).

40.   Jacobsen, D. M., Bao, Z.-Q., O'Brien, P., Brooks, C. L. & Young, M. A. Price to be
paid for two-metal catalysis: magnesium ions that accelerate chemistry unavoidably
limit product release from a protein kinase. *J. Am. Chem. Soc.* **134,** 15357–70 (2012).

41.   Murshudov, G. N., Vagin, A. A. & Dodson, E. J. Refinement of macromolecular
structures by the maximum-likelihood method. *Acta Crystallogr. D. Biol. Crystallogr.*
53, 240–55 (1997).

42.   Emsley, P. & Cowtan, K. Coot: model-building tools for molecular graphics. *Acta
Crystallogr. D. Biol. Crystallogr.* **60,** 2126–32 (2004).

43.   The CCP4 suite: programs for protein crystallography. *Acta Crystallogr. D. Biol.
Crystallogr.* **50,** 760–3 (1994).

44.   Davis, I. W. *et al.* MolProbity: all-atom contacts and structure validation for proteins
and nucleic acids. *Nucleic Acids Res.* **35,** W375–83 (2007).

Chapter 5

Conclusions and future directions

5.1 Conclusions

The work in this dissertation describes our efforts to employ new approaches to target and identify small molecule inhibitors of the CDC25B phosphatase. We have characterized the structure and dynamics of CDC25B in solution and characterized its interaction with the CDK2/Cyclin A complex. In addition to the CDC25B-CDK2/Cyclin A interaction, we have characterized the novel interaction between the DNA damage repair protein Mre11 and the CDK2/Cyclin A complex. We have demonstrated that Mre11 interacts with CDK2/Cyclin A through two motifs in the unstructured C-terminus, and that this interaction is at least in part mediated through the RxL peptide binding site on Cyclin A. As discussed in Chapter 2, several CDK2/Cyclin A binding partners have a similar mechanism of binding. An intriguing possibility is that the MRE11 C-terminus competes with the CDK2 inhibitor protein p27 for binding to CDK2/Cyclin A. The p27 protein binds primarily in three sites, the Cyclin A RxL-binding site, the CDK2 regulatory site on the N-terminal lobe, and the CDK2 active site. Mutagenesis studies have indicated that the first two sites are the primary mediators of the p27-CDK2/Cyclin A interaction, while the very C-terminus of p27 blocks the active site[1,2]. The Mre11 C-terminus interacts at least in part through the RxL-binding site, and the length of the linker between the two binding motifs on Mre11 is very similar to that of the p27 protein. This leads to the possibility

that Mre11 and p27 bind in a similar manner to CDK2/Cyclin A. The intriguing difference between the Mre11 C-terminus and the p27 C-terminus is that the Mre11 C-terminus is much shorter than that of p27, which would prevent it from being able to reach the CDK2 active site. This may enable Mre11 to compete with p27 for CDK2/Cyclin A binding without inhibiting the CDK2/Cyclin A active site. In an experimental observation not described in this thesis, we found that Mre11 does not directly stimulate CDK2 kinase activity in vitro. The Mre11-p27 competition model may be a possible explanation for this observation. However, this model is not fully consistent, as the p27-CDK2/Cyclin A interaction affinity is much stronger than the affinity of the Mre11-CDK2/Cyclin A interaction[3]. This implies that if the Mre11-p27 competition model is correct, other factors must play a role.

In our efforts to develop novel small molecule inhibitors of CDC25B, we took a multi-faceted drug discovery approach. We simultaneously explored two directions: fragment-based drug discovery and high-throughput screening targeting the CDC25B-CDK2/Cyclin A protein-protein interaction. Using NMR-based fragment based screening, we identified a small molecule ligand of the CDC25B catalytic domain. Additionally, we were able to solve the co-crystal structure with our ligand bound to CDC25B. Guided by this structure, we designed a compound with increased binding affinity by replacing an arginine-coordinated sulfate found in the fragment binding site with a sulfonic acid linked to our ligand. We demonstrated that this compound with increased binding affinity disrupts the CDC25B-CDK2/Cyclin A interaction and inhibits CDC25B catalytic activity. To our knowledge, our inhibitor-bound crystal structure of CDC25B is the first crystal structure with CDC25B bound to a small molecule ligand. This, in combination with our characterization of CDC25B in solution, rationalizes the use of a structure-guided small molecule design approach.

In addition to its advancement of CDC25B inhibitor development, our fragment-based drug discovery (FBDD) efforts help validate the use of this approach to inhibit other difficult but important drug targets. There have been many important targets that have proven difficult for inhibitor discovery using traditional approaches. Studies employing FBDD have had some success in developing inhibitors of such proteins. One recent example of this was the use of FBDD to develop inhibitors of K-Ras[4], a well-established target for therapeutic intervention in a wide variety of cancers that has resisted inhibitor development for many years. Our fragment-based drug discovery study targeting CDC25B adds evidence to the hypothesis that the FBDD may be a more attractive approach to target proteins that have been difficult to inhibit using traditional drug discovery approaches.

In addition to fragment based drug design, we have developed PPI assays to quantify the interaction between CDC25B and CDK2/Cyclin A. We employed these assays in multiple high-throughput screens to identify several new classes of CDC25B-CDK2/Cyclin A protein-protein interaction inhibitors. These compounds have shown promising activities in our initial characterization. Importantly, we have developed a high quality screening assay system for targeting this interaction by using an HTRF-based primary screen and an AlphaLISA-based counter screen. This approach will be useful for future drug discovery efforts.

Despite the development of a high-quality screening assay, we have been unable to identify compounds directly inhibiting CDC25B in our high-throughput screens. We know from our fragment-based screening approach that inhibitors targeting CDC25B can be developed; however, no compound identified by high-throughput screening interacts with CDC25B. All the validated inhibitors we identified in our three high-throughput screening campaigns bind to CDK2/Cyclin A. A possible reason for the lack of direct CDC25B inhibitors identified relates

130

to the compound libraries we screened. Many compound screening libraries are not well suited for the discovery of protein-protein interaction inhibitors[5,6], so it is possible that the libraries we screened simply do not contain the type of compounds that bind to CDC25B. As focused protein-protein interaction inhibitor libraries become more prominent, our assay will be useful for further screening efforts targeting CDC25B.

In addition to the CDC25 family of phosphatases, other dual specificity phosphatases (DSPs) have been implicated in a variety of human diseases[7,8]. Several of these DSPs have been shown to have therapeutic potential in and cancer and other diseases[8]. However, like the CDC25 family, the DSPs superfamily in general have proven to be difficult drug targets due to their shallow active sites and complex substrate recruitment mechanisms[8]. The approaches described here, including fragment-based drug discovery and protein-protein interaction based high throughput screening, may be an attractive approach to target other members of the DSP superfamily. The validity of this approach has been recently corroborated in a study where protein-protein interaction based high throughput screening led to the identification of an allosteric inhibitor of the oncogenic DSP Wip1[9]. The studies described in this dissertation add to the growing knowledge of how inhibitors of this important class of enzymes can be identified and developed.

5.2 Future directions

The conclusions of this dissertation open several new lines of inquiry. Regarding the Mre11-CDK2/Cyclin A interaction: we have identified the motifs through which this interaction is mediated, but how Mre11 activates the CDK2/Cyclin A complex remains unknown. As hypothesized above, the increased kinase activity of CDK2 may be due to competition with the

CDK2/Cyclin A inhibitor p27. Multiple approaches could be taken to evaluate this hypothesis. Structural studies of the Mre11-CDK2/Cyclin A complex would reveal if there is similarity between the Mre11 and p27 binding modes. This hypothesis could be further assessed in vitro by determining Mre11-p27 competition for CDK2/Cyclin A binding. However, this approach is limited due to the higher affinity of p27 for CDK2/Cyclin A in vitro. This model may be better addressed in cells by overexpressing the Mre11 C-terminus and looking into the extent of p27-CDK2/Cyclin A interaction by co-immunoprecipitation. In addition to the mechanism of CDK2 activation, the regulation mode of the Mre11-CDK2/Cyclin A interaction remains unknown. Further biological studies will be required to determine the pathways and mechanisms involved in regulating this interaction in cells.

Regarding the development of CDC25B inhibitors: as mentioned above, our structure of the CDC25B-inhibitor complex is the first such structure published, and our studies have indicated that this site is amenable to structure-based design. Further development of our fragment-derived inhibitor will require involvement of medicinal chemistry in order to develop more potent compounds. Several additional approaches for enhancing the binding affinity could be tried. For example, replacing one or more of the water molecules found near the hydroxyl group of the compound might increase the binding affinity of our inhibitor. Additionally, modification at the 5-position on the benzene ring may form additional contacts with the backbone amide of glycine 80 or the side chain of arginine 488. Further chemical exploration of this molecule may lead to more potent inhibitors.

The development of our high-throughput screening assays targeting the CDC25B-CDK2/Cyclin A interaction and the compounds they identified both warrant further study. Further experimentation with our lead compounds can be done to further explain their

mechanism of action and improve their potency. We have shown by NMR that CCG-17950 interacts with the CDK2/Cyclin A complex, but its mode of action is unclear. The presence of either ATP or a potent ATP-competitive inhibitor does not affect the inhibitory activity of CCG-17950, so it unlikely to bind in the CDK2 active site. Structural studies have proven difficult due to the low solubility of the compound. The number of available commercial analogs of CCG-17950 is very limited, so analogs with increased potency and/or solubility would need to be synthesized. Such analogs may be more amenable to structural characterization. As with CCG-17950, relatively few analogs of CCG-18861 are commercially available, and of those we were able to obtain, none had an increased potency compared to the original compound. If more potent analogs of CCG-18861 can be developed, these may allow for the determination of a inhibitor-bound co-crystal structure with CDK2/Cyclin A. A co-crystal structure with a CCG-18861 analog would help us better understand its mechanism of inhibition in the context of the Cyclin A RxL-binding pocket. Such information would allow for structure-guided drug design of increasingly more potent analogs of CCG-18861. In addition to structural information, more potent CCG-18861 analogs would allow for characterization of the cellular activities of these inhibitors. The RxL-binding site on cyclins is an important structural feature, mediating interactions with a number of substrates, protein activators, and protein inhibitors. A cell-active inhibitor of this site would be useful in characterizing the biological role of this site. Additionally, this site may represent a new approach to targeting CDK activity by disrupting cyclin-dependent substrate recruitment. The RxL-binding site has been targeted previously with peptide-based inhibitors[10–12], but converting these molecules into lead compounds remains a challenge[13,14]. Our inhibitor may provide a new scaffold for targeting this site.

Importantly, our high-throughput screening assays allow for the discovery of additional inhibitors of the CDC25B-CDK2/Cyclin A interaction. Our HTRF-based high-throughput screening assay is both robust and sensitive, and uses an entirely different approach to previous high-throughput screens targeting CDC25B. The low hit rate we observed indicates that this assay could be used to potentially screen very large compound libraries while still being able to follow up with weak hits. Our assay could also be used to screen compound libraries specifically designed for the discovery of PPIs, which may be better suited for finding inhibitors of the CDC25B-CDK2/Cyclin A interaction.

5.3 Final remarks

In all, the work presented in this dissertation describes several new approaches to inhibit CDC25B that have not been tried in over 20 years of targeting the CDC25 family. We have laid the groundwork for the identification and development of novel chemical probes and potential therapeutic agents targeting CDC25B.

5.4 References

1. Russo, A. A., Jeffrey, P. D., Patten, A. K., Massagué, J. & Pavletich, N. P. Crystal structure of the p27Kip1 cyclin-dependent-kinase inhibitor bound to the cyclin A-Cdk2 complex. *Nature* **382,** 325–31 (1996).

2. Vlach, J., Hennecke, S. & Amati, B. Phosphorylation-dependent degradation of the cyclin-dependent kinase inhibitor p27. *EMBO J.* **16,** 5334–5344 (1997).

3. Bowman, P., Galea, C. A., Lacy, E. & Kriwacki, R. W. Thermodynamic characterization of interactions between p27(Kip1) and activated and non-activated Cdk2: intrinsically unstructured proteins as thermodynamic tethers. *Biochim. Biophys. Acta* **1764,** 182–9 (2006).

4. Sun, Q. *et al.* Discovery of small molecules that bind to K-Ras and inhibit Sos-mediated activation. *Angew. Chem. Int. Ed. Engl.* **51,** 6140–3 (2012).

5. Sperandio, O., Reynès, C. H., Camproux, A.-C. & Villoutreix, B. O. Rationalizing the chemical space of protein-protein interaction inhibitors. *Drug Discov. Today* **15,** 220–9 (2010).

6. Pagliaro, L. *et al.* Emerging classes of protein-protein interaction inhibitors and new tools for their development. *Curr. Opin. Chem. Biol.* **8,** 442–9 (2004).

7. Patterson, K. I., Brummer, T., O'Brien, P. M. & Daly, R. J. Dual-specificity phosphatases: critical regulators with diverse cellular targets. *Biochem. J.* **418,** 475–89 (2009).

8. Bakan, A., Lazo, J. S., Wipf, P., Brummond, K. M. & Bahar, I. Toward a molecular understanding of the interaction of dual specificity phosphatases with substrates: insights from structure-based modeling and high throughput screening. *Curr. Med. Chem.* **15,** 2536–44 (2008).

9. Gilmartin, A. G. *et al.* Allosteric Wip1 phosphatase inhibition through flap-subdomain interaction. *Nat. Chem. Biol.* **10,** 181–7 (2014).

10. Premnath, P. N. *et al.* Fragment based discovery of arginine isosteres through REPLACE: Towards non-ATP competitive CDK inhibitors. *Bioorg. Med. Chem.* (2013). at <http://www.sciencedirect.com/science/article/pii/S0968089613009139>

11. Andrews, M. J. I. *et al.* REPLACE: a strategy for iterative design of cyclin-binding groove inhibitors. *Chembiochem* **7,** 1909–15 (2006).

12. Atkinson, G. E. *et al.* Peptide inhibitors of CDK2-cyclin A that target the cyclin recruitment-Site: structural variants of the C-Terminal Phe. *Bioorg. Med. Chem. Lett.* **12,** (2002).

13. Premnath, P. N. *et al.* Iterative conversion of cyclin binding groove peptides into druglike CDK inhibitors with antitumor activity. *J. Med. Chem.* **58,** 433–42 (2015).

14. Castanedo, G. *et al.* CDK2/cyclinA inhibitors: targeting the cyclinA recruitment site with small molecules derived from peptide leads. *Bioorg. Med. Chem. Lett.* **16,** 1716–

Chapter 6

Appendix - development of the FMAP program for use in the rational design of fluorinated compounds

6.1 Abstract

Multipolar interactions involving fluorine and the protein backbone have been frequently observed in protein-ligand complexes. Such fluorine-backbone interactions may substantially contribute to high affinity binding of small molecule inhibitors. In order to facilitate the design of multipolar fluorine-backbone interactions in protein-ligand complexes we developed a computational algorithm named FMAP, which calculates fluorophilic sites in close proximity to protein backbone. We demonstrated that FMAP could be used to rationalize improvement in activity of known protein inhibitors upon introduction of fluorine. Furthermore, FMAP may also represent a valuable tool for designing new fluorine substitutions and support ligand optimization in drug discovery projects.

6.2 Rationale and implementation of FMAP

The primary impetus for developing the FMAP program was the observation of large gains in affinity upon the introduction of specifically placed fluorine atoms in our thienopyrimidine class of menin inhibitors. Substitution of a propyl group on the thienopyrimidine scaffold with trifluoroethyl resulted in a 10-fold increase in the binding affinity[1]. The crystal structure of this compound bound to menin revealed that the CF_3 group is involved in close contacts with the protein backbone. This kind of C–F$\cdots$C=O orthogonal interaction had also been previously reported in the literature as an effective method for increasing binding ligand binding affinity[2–4]. Beyond the increase in binding affinity, introduction of fluorine atoms into drug-like molecules can improve their physiochemical properties[5]. However, introduction of fluorine atoms into ligand molecules might be synthetically challenging or may require multi-step synthesis. Therefore, we wanted to develop a method for rational design of favorable fluorine interactions in protein-ligand complexes that would significantly accelerate inhibitor development in our drug discovery projects. We designed the FMAP program to predict regions of the protein backbone that are reasonably exposed in order to engineer favorable C–F$\cdots$C=O interactions. FMAP is implemented in python, and can be run either as a pymol extension or as a standalone command-line program. FMAP requires the Biopython module[6,7].

6.3 PDB search for fluorine containing protein-ligand complexes

To get an idea for the geometrical criteria of the C–F$\cdots$C=O interaction, I performed a search of the PDB to identify protein-ligand complexes containing fluorine atoms. I identified 2559 crystal structures containing a fluorinated ligand and performed an analysis using a python script to select structures in which a fluorine atom is located within 3.5 Å of either the peptide backbone

carbonyl carbon or amide nitrogen. I accepted structures with 2.2 Å resolution or better for further analysis. I found total of 442 protein-ligand complexes fitting these criteria for detailed analysis. The geometrical position of each fluorine in these complexes with respect to the protein backbone was extracted and mapped onto an example protein residue (Figure 6.1). This search demonstrated that fluorine is frequently located within a short distance of protein backbone, and exemplifies the presence of multipolar C–F⋯C=O interactions described in detail in the previous studies[3,4].

6.4 Hypothetical fluorine position calculation by FMAP

Calculation of the fluorine sites is initiated by defining an arbitrary number of 29 hypothetical fluorine positions within 3 Å distance from either the backbone carbon or nitrogen. These hypothetical fluorine positions are based on my analysis of protein-ligand complexes from the PDB; I selected geometric criteria to encompass ~80% of fluorine sites found in this analysis. The hypothetical fluorine positions are defined in spherical coordinates from either the carbonyl carbon or the amide nitrogen in a right-handed spherical coordinate system. The corresponding Cartesian coordinate system to the spherical coordinate system is defined by the positive Z-axis (zenith reference) along the C=O bond, the positive X-axis (azimuth reference) perpendicular to the Z-axis in the peptide bond plane in the direction of the amide bond, and the Y-axis perpendicular to the peptide plane. The same coordinate system axes is used for all hypothetical positions, however 11 of the hypothetical fluorine positions use the carbonyl carbon as the origin and the remaining positions use the amide nitrogen. The spherical coordinates of the 29 hypothetical fluorine positions and their reference atom are given below (Table 6.A1). Mapping of these hypothetical positions to a hypothetical peptide bond along with the fluorine positions
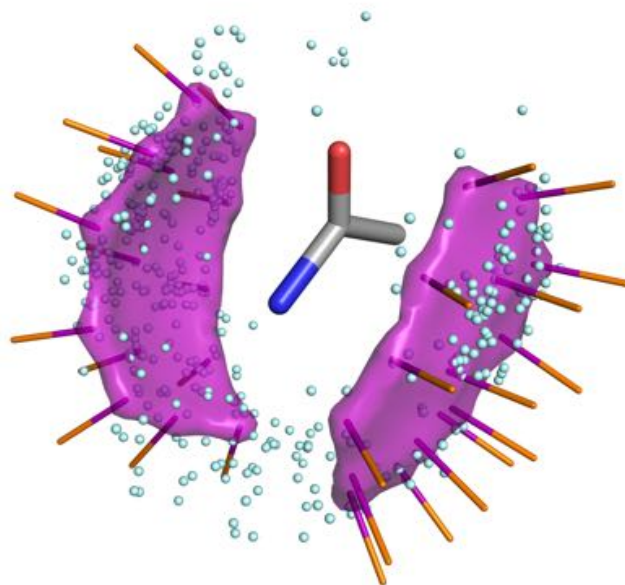
Figure 6.1. *PDB analysis and prediction of favorable C–F⋯C=O interactions using FMAP algorithm*. Combined analysis of protein-ligand structures from PDB, with FMAP predictions of the potential fluorine positions and their representative C-F bonds relative to backbone peptide bond. Positions of fluorine atoms derived from the protein-ligand complexes found in PDB are shown as cyan points. FMAP prediction is shown as purple surface with orange vectors shown for representative C-F bonds.

from my PDB analysis is shown in Figure 6.1.

The 29 hypothetical fluorine positions are then calculated for every residue in the protein of interest. This is accomplished by a translation of the origin followed by a quaternion rotation to align the coordinate system of the hypothetical peptide bond and the coordinate system of a given residue. This allows each hypothetical fluorine position to be calculated for any given residue. This process is applied iteratively for all residues in the protein. Once the complete set of hypothetical positions is calculated for the entire protein, unlikely positions are removed using a series of filters.

6.5 FMAP fluorine position filtering criteria

FMAP eliminates unlikely fluorine positions through filters based on unfavorable geometry for multipolar interactions as well as steric clashes with protein atoms. This series of filters is comprised of the following criteria: 1) steric clash; fluorines within 1.8 Å of any protein atom are removed. 2) entirely buried or overly exposed fluorines; this filter removes positions that are not accessible to small molecules or are entirely exposed, such as protein termini, loops; this is accomplished through a summation the number of Cαs closer than 10 Å and the number of total atoms closer than 5 Å; any position with a Cα count between 15-28 and a total atom count less than 30 is retained. 3) fluorines too close to carbonyl oxygens; positions are eliminated when closer than 2.7 Å from a carbonyl oxygen and less than 60 degrees off the C=O bond vector, eliminating positions that are too close to the electron lone pairs of carbonyl oxygens. 4) isolated sites; this procedure eliminates isolated fluorines, removing positions that are not clustered with other nearby fluorines; fluorines with less than 5 adjacent fluorines within 3.2 Å are removed.

A second, more restricted set of fluorine positions is also defined by FMAP. These positions are a subset of the previously defined positions, and are limited to positions further than 2.7 Å away from another atom, and 3.0 Å away from a carbonyl oxygen for positions less than 60 degrees off the C-O bond vector.

6.6 FMAP visualization in Pymol

Fluorine positions retained after the filtering process are visualized using a Pymol[8] extension and are represented as a surface spanning 2.8-3.2 Å range from the peptide bond (Figure 6.1). This allows for a clear representation of favorable sites for forming a C–F$\cdots$C=O interaction. The less restricted positions are shown in purple and the more restricted positions are shown in orange.

6.7 Training and application of FMAP

As the primary impetus for developing FMAP was to predict sites similar to those contributing to the affinity gains observed for our fluorinated menin inhibitors, I used these structures as training structures for the program. The favorable sites predicted by the final version of the FMAP program agreed well with the C–F···C=O interactions observed in the menin-inhibitor crystal structure (Figure 6.2). Once the program was fully developed and trained on these structures, it was tested against a set of protein-ligand structures with ligands for which the activity of unsubstituted and fluorine substituted analogs have been determined and the crystal structures of fluorine analogs bound to the target proteins are available.

Several structures were selected for FMAP analysis to rationalize fluorine substitutions in these known ligands. FMAP was used to analyze the protein-ligand structures of the following inhibitors in which the addition of fluorine led to an increase in ligand potency: the tricyclic class of thrombin inhibitors[9], fragment-based inhibitors of procaspace-6[10], the tetramethylpiperidine class of HIV viral envelope glycoprotein gp120 inhibitors[11], and β-lactamase inhibitors[12]. The FMAP predictions for these protein-ligand structures agreed well with the increase in potency by the introduction of fluorine in each of the inhibitors (Figure 6.3).
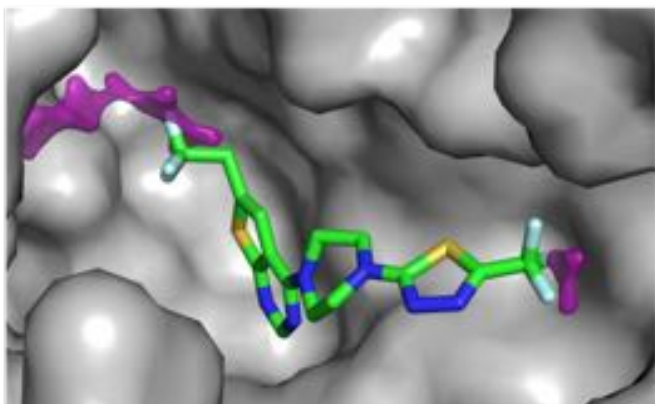

Figure 6.2. *FMAP prediction for the menin-MI-2-3 complex*. Purple surface represents favorable positions for fluorine atoms to interact with protein backbone as predicted by FMAP.
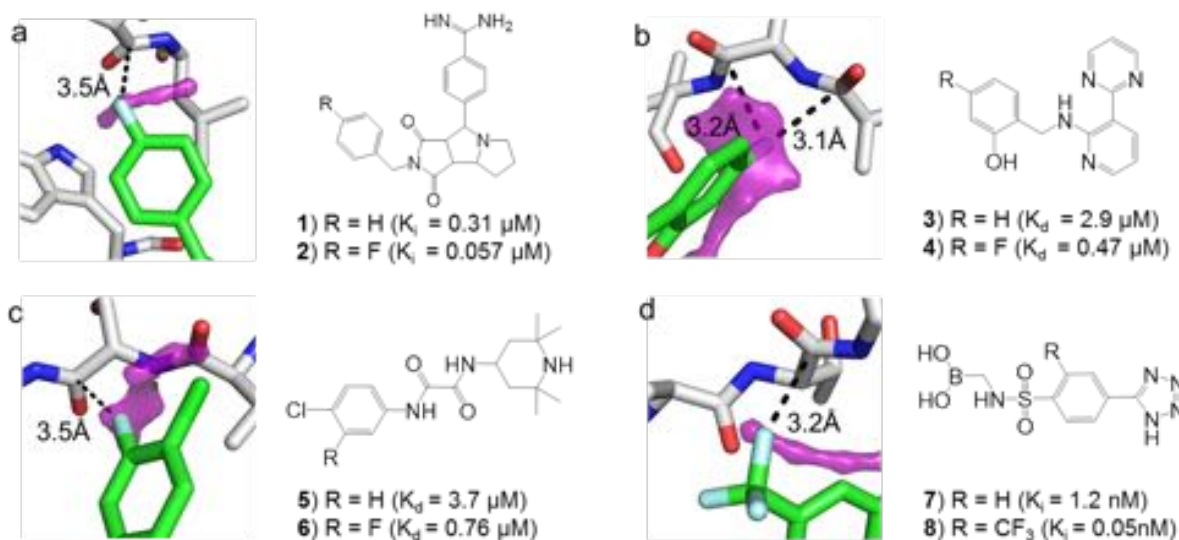
Figure 6.3. *Analysis of FMAP calculations for known inhibitors containing fluorine atoms.* Crystal structure of protein-inhibitor complexes showing close C–F···C=O contacts and FMAP predictions (in purple). The structures of inhibitors and activities are also reported. a) thrombin inhibitor (PDB code 1OYT). b) procaspase-6 inhibitor (PDB code 4NBL). c) gp120 inhibitor (PDB code 4DKO), d) β-lactamase inhibitor (PDB code 4E3N). Figure produced by Jon Pollock.

There were several examples found where substitution with fluorine did not have beneficial effect on inhibitory activity despite reasonably good agreement with the FMAP predictions. In two examples, introduction of fluorine into inhibitors of neuronal nitric oxide synthase[13] and c-Jun N-terminal kinase 1[14] led to the modest decrease in the inhibitory activity. This indicates that prediction of fluorine substitutions based solely on geometrical criteria might have potential limitations and other factors such as effect of fluorine on stereoelectronic or conformational properties of the ligand, or structural changes upon ligand binding might need to be considered in order to further improve the design of C–F···C=O interactions.

6.8 Conclusions

The FMAP program was developed to facilitate the rational design of C–F···C=O interactions in protein-ligand complexes. FMAP uses a protein crystal structure and calculates sites that could be favorable for forming C–F···C=O ligand-protein interactions. We demonstrated that FMAP could be used to rationalize the improvement in activity of several known inhibitors upon introduction of fluorine. FMAP may also represent a valuable tool for the design of new fluorine substitutions in protein ligands. FMAP relies solely on geometrical and structural criteria, and other effects, such as conformational or electronic changes resulting from fluorine substitution are not taken into account, which might represent a limitation of this approach. Nevertheless, we expect the FMAP can be very useful in the drug discovery projects to rationally design new fluorinated ligands. The predictive power of FMAP in the rational design of fluorinated ligands is currently being explored in several projects in the Cierpicki and Grembecka laboratories.

Notes

This appendix is based on a manuscript in preparation "Rational design of orthogonal multipolar interactions with fluorine in protein-ligand complexes" by Jonathan Pollock, Dmitry Borkin, George Lund, Trupta Purohit, Edyta Dyguda-Kazimierowicz, Jolanta Grembecka and Tomasz Cierpicki. Jonathan Pollock performed an extensive literature review regarding the role of fluorines in ligand-protein interactions, determined all menin-inhibitor complex structures and prepared the majority of the manuscript and figures; Dmitry Borkin also contributed to the literature review and was responsible for the menin inhibitor design and synthesis; George Lund performed the analysis of the PDB structures containing C–F···C=O interactions, wrote the FMAP program and wrote the description of the algorithm; Trupta Purohit performed activity fluorescence polarization assays for determination of the potency of menin-MLL inhibitors; Edyta Dyguda-Kazimierowicz performed quantum mechanical calculations of the C–F···C=O interaction (not shown here); , Jolanta Grembecka and Tomasz Cierpicki supervised the project and reviewed the manuscript.

6.9 Appendices

Appendix Table 6.A1. *Polar coordinates of the hypothetical fluorine positions and their reference atom.*

Hypothetical fluorine	Reference atom	R (Å)	Polar angle (rad)	Azimuthal angle (rad)
1	C	3.00	1.47	1.57
2	C	3.00	1.89	1.71
3	C	3.00	1.31	1.14
4	C	3.00	0.97	1.50
5	C	3.00	1.20	1.90
6	C	3.00	1.60	1.97
7	C	3.00	1.53	-1.33
8	C	3.00	1.14	-1.48
9	C	3.00	1.87	-1.70
10	C	3.00	1.20	-0.91
11	C	3.00	1.47	-1.84
12	N	3.00	1.33	1.31
13	N	3.00	1.55	1.67
14	N	3.00	1.89	1.82
15	N	3.00	2.18	2.12
16	N	3.00	2.31	1.22
17	N	3.00	2.36	1.72
18	N	3.00	1.92	1.52
19	N	3.00	2.00	1.14
20	N	3.00	1.58	1.07
21	N	3.00	1.72	-1.51
22	N	3.00	2.02	-1.91
23	N	3.00	1.31	-1.15
24	N	3.00	1.82	-0.91
25	N	3.00	2.21	-0.82
26	N	3.00	2.52	-1.05
27	N	3.00	2.14	-1.26
28	N	3.00	2.40	-1.75
29	N	3.00	2.81	-1.60

6.10 References

1. Shi, A. *et al.* Structural insights into inhibition of the bivalent menin-MLL interaction by small molecules in leukemia. *Blood* **120,** 4461–9 (2012).

2. Olsen, J. A. *et al.* Fluorine interactions at the thrombin active site: protein backbone fragments H-C(alpha)-C=O comprise a favorable C-F environment and interactions of C-F with electrophiles. *Chembiochem* **5,** 666–75 (2004).

3. Paulini, R., Müller, K. & Diederich, F. Orthogonal multipolar interactions in structural chemistry and biology. *Angew. Chem. Int. Ed. Engl.* **44,** 1788–805 (2005).

4. Müller, K., Faeh, C. & Diederich, F. Fluorine in pharmaceuticals: looking beyond intuition. *Science* **317,** 1881–6 (2007).

5. Purser, S., Moore, P. R., Swallow, S. & Gouverneur, V. Fluorine in medicinal chemistry. *Chem. Soc. Rev.* **37,** 320–30 (2008).

6. Hamelryck, T. & Manderick, B. PDB file parser and structure class implemented in Python. *Bioinformatics* **19,** 2308–10 (2003).

7. Cock, P. J. A. *et al.* Biopython: freely available Python tools for computational molecular biology and bioinformatics. *Bioinformatics* **25,** 1422–3 (2009).

8. Schrodinger LLC. The PyMOL Molecular Graphics System, Version 1.3r1. (2010).

9. Olsen, J. A. *et al.* A fluorine scan of thrombin inhibitors to map the fluorophilicity/ fluorophobicity of an enzyme active site: evidence for C-F...C=O interactions. *Angew. Chem. Int. Ed. Engl.* **42,** 2507–11 (2003).

10. Murray, J. *et al.* Tailoring small molecules for an allosteric site on procaspase-6. *ChemMedChem* **9,** 73–7, 2 (2014).

11. LaLonde, J. M. *et al.* Structure-based design, synthesis, and characterization of dual hotspot small-molecule HIV-1 entry inhibitors. *J. Med. Chem.* **55,** 4382–96 (2012).

12. Eidam, O. *et al.* Fragment-guided design of subnanomolar β-lactamase inhibitors active in vivo. *Proc. Natl. Acad. Sci. U. S. A.* **109,** 17448–53 (2012).

13. Huang, H. & Silverman, R. B. Recent advances toward improving the bioavailability of neuronal nitric oxide synthase inhibitors. *Curr. Top. Med. Chem.* **13,** 803–12 (2013).

14. Probst, G. D. *et al.* Highly selective c-Jun N-terminal kinase (JNK) 2 and 3 inhibitors with in vitro CNS-like pharmacokinetic properties prevent neurodegeneration. *Bioorg. Med. Chem. Lett.* **21,** 315–9 (2011).